# Polymer-coated magnetic nanoparticles and modified polymer nanofibers for the efficient capture of *Mycobacterium tuberculosis (Mtb)*

by

Marica Smit

*Thesis presented in partial fulfilment of the requirements for the degree of Master of Science in Chemistry and Polymer Science at Stellenbosch University*


Supervisor: Dr. Marietjie Lutz

March 2018

*The financial assistance of the National Research Foundation (NRF) towards this research is hereby acknowledged. Opinions expressed and conclusions arrived at, are those of the author and are not necessarily to be attributed to the NRF*

## Declaration

By submitting this thesis electronically, I declare that the entirety of the work contained therein is my own, original work, that I am the sole author thereof (save to the extent explicitly otherwise stated), that reproduction and publication thereof by Stellenbosch University will not infringe any third party rights and that I have not previously in its entirety or in part submitted it for obtaining any qualification.

March 2018

## Abstract

The World Health Organization (WHO) determined that 10.4 million people died of tuberculosis (TB) in 2015 which makes TB the number one cause of death from a preventable infectious disease worldwide. *Mycobacterium tuberculosis* (*Mtb*) is the causative pathogen of TB and a frequent lack of clinical symptoms hampers the pathogen's detection. Current diagnostic tests are limited when applied to low populations of bacteria in biological fluids, such as blood. A large volume of biological fluid is needed for a positive diagnosis. Obtaining multiple samples are, however, difficult, especially from children under six years. A smaller amount of biological fluid will be needed if the *Mtb* can be captured and concentrated within the sample. Polymer coated superparamagnetic magnetite nanoparticles (SPMNs) with affinity for the pathogen can be used as capturing substrates for *Mtb* followed by diagnosis via existing microscopy methods such as fluorescence microscopy (FM).

In this thesis, modified chitosan and modified poly(styrene-*alt*-maleic anhydride) (SMA) were synthesized and utilized to coat SPMNs as well as electrospun into nanofibers to form potential *Mtb* capturing substrates. Chitosan and SMA were modified to from quaternary derivatives which can possibly interact with the *Mtb* cell wall. The nano-substrates were also surface functionalized with a carbohydrate binding protein, namely Concanavalin A (Con A), which can bind to the *Mtb* cell wall. Chitosan coated SPMNs were synthesized by in situ co-precipitating $Fe^{2+}$ and $Fe^{3+}$ with chitosan followed by further modification. SMA coated SPMNs were synthesized by activating the iron oxide core with 3-aminopropyl(triethoxysilane) (3-APTES) followed by further modification. Polymer nanofibers were electrospun via single needle electrospinning. The chitosan derivatives were electrospun into nanofibers by blending with non-ionogenic polymers, viz. polyvinyl alcohol (PVA), polylactide (PLA), polycaprolactam (Nylon 6), polyethylene oxide (PEO) and polyvinyl pyrrolidone (PVP) to facilitate electrospinning.

The nano-substrates were evaluated for their affinity and thus capturing capabilities utilizing the mCherry fluorophore tagged bacillus Calmette-Guérin (BCG) strain of *Mycobacterium bovis*, a live attenuated *Mtb*-mimic. A preliminary nanofiber affinity study was conducted to determine which polymer-and-functional-moiety combination had the highest affinity for the bacteria utilizing FM (fluorescence microscopy). Quaternary SMA (SMI-q$C_{12}$) had the highest affinity for BCG-mCherry (through electrostatic and hydrophobic interactions) followed by Con A immobilized chitosan (CS-EDC-Con A). The SPMNs were coated with three different polymer loadings and a dilution study performed to determine the limit of detection. The 0.9 g loaded SMI-q$C_{12}$ SPMNs had the highest affinity for BCG-mCherry determined via FM and TEM (transmission electron microscopy).

## Opsomming

Die wêreldgesondheidsorganisasie (WGO) het bepaal dat 10.4 miljoen mense gesterf het a.g.v tuberkolose (TB) in 2015 wat TB dus die vernaamste oorsaak van dood aan voorkombare aansteeklike siektes maak wêreldwyd. *Mycobacterium tuberculosis* (*Mtb*) is die patogeen wat TB veroorsaak en ‘n gereelde gebrek aan kliniese simptome belemmer die opsporing van die patogeen. Huidige diagnostiese toetse is beperk wanneer toegepas word op lae populasies van bakterieë in biologiese vloestowwe, soos bloed. ‘n Groot volume biologiese vloeistof word benodig vir ‘n positiewe diagnose. Die verkryging van veelvuldige monsters is egter moeilik, veral van kinders onder ses jaar. ‘n Kleiner hoeveelheid biologiese vloeistof word benodig as die *Mtb* vasgevang en gekonsentreer kan word binne die monster. Polimeer bedekte superparamagnetiese magnetiet nanopartikels (SPMNs) met ‘n affiniteit vir die patogeen kan gebruik word as vasvangingsubstrate vir *Mtb* gevolg deur diagnose via bestaande mikroskopie metodes soos fluoresensie mikroskopie (FM).

In hierdie tesis is gemodifiseerde chitosan en gemodifiseerde poli (styreen-*alt*-maleïensanhidried) (SMA) gesintetiseer en gebruik om SPMNs te bedek asook om nanovesels te elektrospin om potensiële *Mtb* vasvangingsubstrate te vorm. Chitosan en SMA is gemodifiseer om kwaternêre afgeleides te vorm wat moontlik ‘n interaksie kan hê met die *Mtb* selwand. Die nano-substrate is ook oppervlak gefunktionaliseer met ‘n koolhidraat bindende proteïen, naamlik Concanavalin A (Con A), wat kan bind aan die *Mtb* selwand. Chitosan bedekte SPMNs was gesintetiseer deur in situ mede-neerslag van $Fe^{2+}$ en $Fe^{3+}$ met chitosan gevolg deur verdere modifikasie. SMA bedekte SPMNs is gesintetiseer deur aktivering van die ysteroksied kern met 3-aminopropiel(trietoksiesilaan) (3-APTES) gevolg deur verdere modifikasie. Polimeer nanovesels was geëlektrospin via die enkelnaald elektrospin tegniek. Die chitosan afgeleides is tot nanovesels geëlektrospin deur vermenging met nie-ionogeniese polimere, nl. poliviniel alkohol (PVA), polilaktied (PLA), polikaprolaktaam (Nylon 6), poliëtileen oksied (PEO) and poliviniel pirrolidoon (PVP) om elektrospin te fasiliteer.

Die nano-substrate is geëvalueer vir hul affinitiet en dus vasvangingsvermoë d.m.v die mCherry fluorofoor gemerkte bacillus Calmette-Guérin (BCG) stam van *Mycobacterium bovis,* ‘n lewendige verswakte *Mtb* mimiek. ‘n Voorlopige nanovesel affiniteitstudie is uitgevoer om te bepaal watter polimeer-en-funksionele-group kombinasie die hoogste affinitiet het vir die bakterieë d.m.v FM (fluoresensie mikroskopie). Kwaternêre SMA (SMI-$qC_{12}$) het die hoogste affiniteit gehad vir BCG-mCherry (deur elektrostatiese en hidrofobiese interaksies) gevolg deur Con A geïmmobiliseerde chitosan (CS-EDC-Con A). Die SPMNs is bedek met drie verskillende polimeer ladings en ‘n verdunningstudie is uitgevoer om die

opsporingsperk te bepaal. Die 0.9 g bedekte SMI-q$C_{12}$ het die hoogste affiniteit gehad vir BCG-mCherry soos bepaal via FM en TEM (transmissie elektron mikroskopie).

## Acknowledgements

First and foremost I would like to thank God for giving me strength and guidance and helping me overcome difficulties.

I would like to thank my supervisor and mentor, Dr. Marietjie Lutz for her guidance and support throughout this project.

I would like to thank the staff of the Central Analytical Facility: Dr. Angelique Laurie, Madeleine Frazenburg and Elrika Harmzen-Pretorius for training and helping me obtain SEM and EDX images; Elsa Malherbe and Dr. Jaco Brand for NMR analyses; Lize Engelbrecht, Rozanne Adams and Dumisile Lumkwana for their expertise and problem solving to obtain FM images.

I would like to thank Mohammed Jaffer for skilfully obtaining TEM images at UCT.

I would like to thank Dr. Du Preez van Staden and Dr. Tiaan Heunis for culturing BCG numerous times and for assistance with the BCG affinity studies.

I would like to thank the staff at the Department of Chemistry and Polymer Science, especially Erinda Cooper, Aneli Fourie, Calvin Maart, Jim Motshweni and Deon Koen for insuring that everything at the Polymer Science building runs smoothly.

I would like to thank Professor van Reenen and the Olefins Research group for guidance and assistance during my postgraduate studies.

I would like to thank the University of Stellenbosch and the National Research Foundation for the financial support during my studies.

Finally I would like to thank my parents, sister and friends for encouragement, support and motivation.

# Table of Contents

## List of Figures

## List of Schemes

# List of Tables

## List of Abbreviations and Acronyms

**∝-$Fe_2O_3$** hematite

**$\gamma$-$Fe_2O_3$** maghemite

**3-APTES** 3-aminopropyl(triethoxysilane)

**ABTS** 2,2'-azino-bis(3-ethylbenzthiazoline-6-sulfonic acid)

**AcOH** acetic acid

**AIBN** 2,2'-azobis(2-methylpropionitrile)

**ATR-FTIR** attenuated total reflectance Fourier transform infrared

**BA** 1,2,3,4-butanetetracarboxylic acid

**BAL** Bronchoalveolar lavage

**BCG** bacillus Calmette-Guérin

**CF** continuous-flow

**CFU** colony-forming units

**Con A** Concanavalin A

**CP-MAS** cross polarization magic-angle-spinning

**CS** chitosan

**CS-EDC** chitosan-glutaraldehyde-glycine-EDC

**CS-$qC_{10}$** *N*,*N*-(2-dimethyl)propyl-3-*N',N'*-dimethyl-*N'*-decylammonium chitosan chloride

**CS-$qC_{12}$** *N*,*N*-(2-dimethyl)propyl-3-*N',N'*-dimethyl-*N'*-dodecylammonium chitosan chloride

**DA** degree of *N*-acetylation

**DAS** 4,4'-diazido-2,2'-stilbenedisulfonic acid disodium salt tetrahydrate

**DCM** dichloromethane

**DDA** degree of *N*-deacetylation

**DMF** *N*,*N*-dimethylformamide

**DMPA** 2,2-dimethoxy-2-phenylacetophenone

**DMSO** dimethyl sulfoxide

**DQ** degree of quaternization

**EC** enzyme commission

**EDC** *N*-(3-dimethylaminopropyl)-*N'*-ethylcarbodiimide hydrochloride

**EDX** energy dispersive X-ray

**ELISA** enzyme-linked immunosorbent assay

**EPTB** extra pulmonary TB

**$Fe(OH)_3$** Iron(III) oxide-hydroxide

**$Fe^{2+}$** ferrous iron ion

**$Fe^{3+}$** ferric iron ion

**$Fe_3O_4$** magnetite

**FM** fluorescence microscopy

**FWHM** full width at half-maximum

**GlcN** 2-amino-2-deoxy-β-d-glucopyranose

**GlcNAc** β(1→4)-linked 2-acetamido-2-deoxy-β-d-glucopyranose

**GLU** glutaraldehyde

**GLY** glycine

**GPLs** glycopeptidolipids

**HRP** horseradish peroxidase

**LM** light microscopy

**MAnh** maleic anhydride

**Man-LAM** mannose-capped lipoarabinomannan

**MEK** methyl ethyl ketone

**MRI** magnetic resonance imaging

***Mtb*** *Mycobacterium tuberculosis*

**Mw** molecular weight

**NALC** N-acetyl-L-cysteine

**NMR** nuclear magnetic resonance

**Nylon 6** polycaprolactam

**PBS** phosphate buffered saline

**PCR** polymerase chain reaction

**PDIMs** phthiocerol dimycocerosates

**PEO** polyethylene oxide

**PGLs** phenolic glycolipids

**PLA** polylactide

**POC** point-of-care

**PPD** purified protein derivate

**PTB** pulmonary TB

**PVA** polyvinyl alcohol

**PVP** polyvinyl pyrrolidone

**P-XRD** powder X-ray diffraction

**SEM** scanning electron microscopy

**SMA** poly(styrene-*alt*-maleic anhydride)

**SMI-qC$_{10}$** poly(styrene-[*N*-3-(*N'*-decyl-*N',N'*-dimethylammonium)propyl maleimide])

**SMI-qC$_{12}$** poly(styrene-[*N*-3-(*N'*-dodecyl-*N',N'*-dimethylammonium)propyl maleimide])

**SMI-tC** poly(styrene-[*N*-3-(*N',N'*-dimethylamino)propyl maleimide])

**SPIONs** superparamagnetic iron oxide nanoparticles

**SP-MAS** single pulse magic-angle-spinning

**SPMNs** superparamagentic magnetite nanoparticles

**SQUID** superconducting quantum interference device

**TB** Tuberculosis

**TDMs** trehalose dimycolates

**TEGDMA** triethylene glycol dimethacrylate

**TEM** transmission electron microscopy

**TFA** trifluoroacetic acid

**TGA** thermogravimetric analysis

**THF** tetrahydrofuran

**TMC** trimethylammonium chitosan chloride

**WCA** water contact angle

**WHO** World Health Organization

**wt%** weight percentage

## List of Symbols

| | |
|---|---|
| Å | Angstrom |
| $D_p$ | average size of the crystalline domains |
| eV | electronvolts |
| k | Scherrer constant |
| K | Kelvin |
| kHz | kilohertz |
| kV | kilovolts |
| MHz | megahertz |
| λ | X-ray wavelength |

# Chapter 1

Introduction

## 1.1 Introduction

Tuberculosis (TB) is one of the three primary poverty-related infectious diseases with a high morbidity and mortality rate. The management and diagnosis of childhood TB in developing countries remains challenging due to low bacilli yield.[1] *Mycobacterium tuberculosis* (*Mtb*) is the causative pathogen of tuberculosis and is an intracellular pathogen that relies on the survival of the microorganism within host cells. This mode of infection and frequent lack of clinical symptoms hampers the pathogen's detection. Current diagnostic tests are limited as it is difficult to detect low populations of bacteria in biological fluids, such as blood, sputum and lymph fluid.[2] A large volume of biological fluid, for example sputum, is needed for a positive diagnosis. Obtaining multiple samples are, however, difficult, especially from children under six years.[3] A smaller amount of biological fluid will be needed if the *Mtb* can be concentrated within the sample. Substrates with affinity for the pathogen can be used to capture and thus concentrate *Mtb*.

Polymers with known affinity to *Mtb* can be used as substrates. Chitosan, a natural polysaccharide, possesses favourable properties, such as non-toxicity, antibacterial activity, bacterial adhesion, biodegradability and biocompatibility.[4] The quaternary derivatives of *N*-alkyl chitosan have been shown to have an even higher bacterial activity when compared to chitosan itself.[5] Poly(styrene-*alt*-maleic anhydride) (SMA) can be used as biological substrate due to its low toxicity, low cost, bacterial adhesion and good biocompatibility and biodegradation. The reactive anhydride functional groups can be used to form quaternary ammonium derivatives of SMA with known *Mtb* affinity.[6,7] Concanavalin A (Con A) immobilized to chitosan and SMA is a well-studied carbohydrate-binding protein and human receptor for the carbohydrate-based structures on the surface of *Mtb*, such as mannose. The interaction between these human receptors and mycobacterial mannose can facilitate the capture and concentration of *Mtb*.[7] These polymers can be incorporated into nanofibers and nanoparticles and used as *Mtb* capturing platforms.

Materials at nanoscale (nanoparticles and nanofibers) have tuneable properties, a high specific surface area and a high aspect ratio.[8] These qualities are favourable for the adhesion of *Mtb*. Electrospinning can be used to produce quaternary ammonium chitosan and SMA nanofibers. Con A was immobilized to the chitosan and SMA fibers post-

electrospinning to avoid degradation. Superparamagnetic iron oxide nanoparticles can be controlled with regard to shape, size and crystallinity followed by polymer coating to incorporate functional groups. Chitosan and SMA derivatives form a coating around magnetic iron oxide nanoparticles via chelation with the Fe-OH groups.[9] The bacilli in a sample can thus be captured and concentrated to the substrates, followed by extraction via an external magnet. This will thus aid in fast and accurate diagnosis of TB utilizing for instance fluorescence microscopy.

## 1.2 Objectives

The overall aim of this research project is to develop polymer coated magnetic iron oxide nanoparticles with *Mtb* affinity and superparamagnetic properties for the efficient capture of *Mycobacterium tuberculosis* (*Mtb*) from a variety of specimen types to enable fast and accurate diagnosis of tuberculosis using conventional diagnostic methods such as fluorescence microscopy (FM). *Mtb* captured magnetic nanoparticles can be extracted via an external magnet followed by further analysis. Functionalized polymer nanofibers were also investigated as *Mtb* affinity substrates, as nanofibers have shown to have a high sensitivity for bacteria. Polysaccharide chitosan and SMA was used as polymers that can be modified with chemical moieties selected based on possible interactions with the *Mtb* cell wall. Chemical moieties include quaternary ammonium compounds and immobilized Concanavalin A (Con A).These polymers were electropun into nanofibers due to the high specific area and ease of use. Non-ionogenic polymers were needed to facilitate electrospinning of the modified chitosan. The suitability of the non-ionogenic polymers were evaluated via a, live attenuated *Mtb* mimic, Bacillus Calmette-Guérin (BCG) affinity study. Superparamagnetic iron oxide magnetic nanoparticles (SPMNs) coated with the polymer-and-functional-moiety combination which captures BCG with the highest efficacy in the nanofiber study can give an indication of the sensitivity of the SPMNs w.r.t. BCG affinity. The following objectives have been identified in order to address this knowledge gap:

1. Synthesize and characterize poly(styrene-*alt*-maleic anhydride) (SMA) and SMA modified with quaternary ammonium groups thus poly(styrene-[*N*-3-(*N'*-decyl-*N',N'*-dimethylammonium)propyl maleimide]) (SMI-q$C_{10}$) and poly(styrene-[*N*-3-(*N'*-dodecyl-*N',N'*-dimethylammonium)propyl maleimide]) (SMI-q$C_{12}$). Characterize chitosan (CS) and synthesize and characterize CS modified with quaternary ammonium groups CS-q$C_{10}$ (*N*,*N*-(2-dimethyl)propyl-3-*N',N'*-dimethyl-*N'*-decylammonium chitosan chloride) and CS-q$C_{12}$ (*N*,*N*-(2-dimethyl)propyl-3-*N',N'*-

dimethyl-*N'*-dodecylammonium chitosan chloride). Modify chitosan with linker molecules, such as glycine and *N*-(3-dimethylaminopropyl)-*N'*-ethylcarbodiimide hydrochloride (EDC), in order to immobilize Con A.

2. The formation, crosslinking and characterization of SMA nanofibers immobilized with Con A as well as its quaternary derivatives. The formation, crosslinking and characterization of bi-component nanofibers consisting of CS-Con A, CS-$qC_{10}$ and Cs-$qC_{12}$ blended with non-ionogenic polymers, which include polyvinyl alcohol (PVA), polylactide (PLA) and Nylon 6, necessary to facilitate the electrospinning of modified chitosan.

3. BCG affinity studies using $OD_{600nm}$ = 6/18.78 $\times 10^7$ CFU/mL on the modified SMA and CS nanofibers to determine which polymer-and-functional-moiety combination captures BCG with the highest efficacy.

4. Synthesize and characterize superparamagnetic iron oxide magnetic nanoparticles (SPMNs), coated with three different loadings of the polymer-and-functional-moiety combination which captures BCG with the highest efficacy in the nanofiber study.

5. Dilution studies with BCG on the polymer coated SPMNs to determine sensitivity.

## 1.3 Thesis layout

**Chapter 1: Introduction**

This chapter serves as an introduction to the research project and background to previous research. The objectives of the project will be given in a brief research description with the aims to be met.

**Chapter 2: Literature review**

This chapter introduces the historical and theoretical aspects that relate to the thesis. Background will be provided regarding tuberculosis, diagnosis of TB and nanotechnology (coated SPMNs and electrospinning nanofibers). Chitosan and SMA as well as its quaternary ammonium derivatives will be discussed. The use of Con A with regard to *Mtb* affinity will be described.

**Chapter 3: Synthesis and characterization of precursor polymers**

This chapter describes the characterization of pristine chitosan and the synthesis and characterization of quaternized *N*-alkyl chitosan derivatives (CS-q$C_{10}$ and CS-q$C_{12}$). The synthesis and characterization of chitosan modified with linker molecules in order to immobilize Con A will be outlined. The synthesis and characterization of SMA and the quaternized derivatives of SMA (SMI-q$C_{10}$ and SMI-q$C_{12}$) are also included.

**Chapter 4: Chitosan based bi-component nanofibers and SMA based nanofibers**

This chapter describes the formation of bi-component polymeric nanofibers of CS-EDC-Con A (chitosan-glutaraldehyde-glycine-EDC-Con A), CS-q$C_{10}$ and CS-q$C_{12}$ blended with suitable non-ionogenic polymer partners to facilitate electrospinning as well as the subsequent crosslinking to produce aqueous/phosphate buffered saline (PBS) solution stability. The formation of SMA-Con A, SMI-q$C_{10}$ and SMI-q$C_{12}$ nanofibers as well as thermal crosslinking will be described.

**Chapter 5: Synthesis and characterization of superparamagnetic magnetite nanoparticles and nanocomposite materials**

This chapter details the synthesis and characterization of coated superparamagnetic magnetite nanoparticles (SPMNs) consisting of a SPMN core and three different polymer loadings of SMI-q$C_{12}$ and CS-EDC-Con A, respectively. The polymer-and-functional-moiety combinations were determined via the BCG affinity study on the nanofibers.

**Chapter 6: Affinity studies between modified chitosan and modified SMA nano-substrates and mycobacteria**

This chapter presents the evaluation of modified chitosan bi-component nanofibers and modified SMA nanofibers as potential capturing platforms for *M. bovis* BCG, the live virulent strain of *M. tuberculosis*. The polymer-and-functional-moiety combination with the highest BCG affinity was used to coat SPMNs followed by a dilution study to determine the limit of detection.

**Chapter 7: Conclusions and Recommendations**

This chapter provides a summary with regard to the conclusions gathered from this study. Conclusions will be made with regard to polymer modification, nanofiber morphology, super paramagnetic nanoparticles and the affinity studies. The chapter also discusses possible future work.

## 1.4 References


1. Aketi, L., Kashongwe, Z., Kinsiona, C., Fueza, S. B., Kokolomami, J., Bolie, G., Lumbala, P. & Diayisu, J. S. Childhood tuberculosis in a sub-saharan tertiary facility: Epidemiology and factors associated with treatment outcome. *PLoS One* **11,** 1–14 (2016).
2. Kaittanis, C., Santra, S. & Perez, J. M. Emerging nanotechnology-based strategies for the identification of microbial pathogenesis. *Adv. Drug Deliv. Rev.* **62,** 408–423 (2010).
3. Nicol, M. P., Workman, L., Isaacs, W., Munro, J., Black, F., Eley, B., Boehme, C. C., Zemanay, W. & Zar, H. J. Accuracy of the Xpert MTB/RIF test for the diagnosis of pulmonary tuberculosis in children admitted to hospital in Cape Town, South Africa: A descriptive study. *Lancet Infect. Dis.* **11,** 819–824 (2011).
4. Liu, Y., Lv, H., Qin, Y., Deng, L. & Wang, Y. Gentamicin modified chitosan film with improved antibacterial property and cell biocompatibility. *Int. J. Biol. Macromol.* **98,** 550–556 (2017).
5. Sahariah, P., Benediktssdóttir, B. E., Hjálmarsdóttir, M. Á., Sigurjonsson, O. E., Sørensen, K. K., Thygesen, M. B., Jensen, K. J. & Másson, M. Impact of chain length on antibacterial activity and hemocompatibility of quaternary *N*-alkyl and *N*, *N*-dialkyl chitosan derivatives. *Biomacromolecules* **16,** 1449–1460 (2015).
6. Li, Y., Nie, W., Chen, P. & Zhou, Y. Preparation and characterization of sulfonated poly(styrene-*alt*-maleic anhydride) and its selective removal of cationic dyes. *Colloids Surfaces A Physicochem. Eng. Asp.* **499,** 46–53 (2016).
7. Cronje, L., Warren, R. & Klumperman, B. pH-dependent adhesion of mycobacteria to surface-modified polymer nanofibers. *J. Mater. Chem. B* **1,** 6608–6618 (2013).
8. Homayoni, H., Ravandi, S. A. H. & Valizadeh, M. Electrospinning of chitosan nanofibers: Processing optimization. *Carbohydr. Polym.* **77,** 656–661 (2009).
9. Borlido, L., Azevedo, A. M., Roque, A. C. A & Aires-Barros, M. R. Magnetic separations in biotechnology. *Biotechnol. Adv.* **31,** 1374–1385 (2013).

# Chapter 2

Literature review

## 2.1 Introduction

According to data collected by the World Health Organization (WHO) 10.4 million people died of tuberculosis (TB) in 2015. This makes the disease the number one cause of death from a preventable infectious disease worldwide.[1] Early diagnosis and initiation of treatment is essential to reduce the TB burden. Delays in diagnosis and treatment contribute to increased TB transmission and severity of illness. Diagnostic and treatment delay are due to a number of socio-demographic, economic, behavioural and clinical factors. These factors include rural residence, being a smear-positive pulmonary TB (PTB) case, illiteracy, being an extra pulmonary TB (EPTB) case, old age and having multi-drug-resistant TB.[2] TB infection control is especially crucial in areas with a high number of HIV infected residents. The risk of mortality and morbidity is significantly higher in patients infected with TB and HIV. The current TB vaccine, *Mycobacterium bovis* Bacillus Calmette–Guérin (BCG) does not prevent infection but may reduce mortality in children. Currently global initiatives have been launched to prevent, care and control TB namely the End TB Strategy.[3,1]

## 2.2 Infection

*Mtb* (the causative pathogen of TB) infection occurs via pulmonary exposure where active bacilli are inhaled from the environment. The factors that influence infection are mainly living and working conditions. Densely populated living and working areas with poor ventilation (prolonging duration of exposure) as well as immunocompetency with the virus could thus lead to *Mtb* infection. *Mtb* infection occurs when an infected carrier coughs, sneezes or talks and small droplets (1 to 5 µm in diameter) are aerosolized and expelled.[4] These droplets contain the pathogenic species and can be inhaled. The lungs will attempt to phagocytize the pathogen and transport it across the alveolar epithelium where it is taken up by the lungs. A pro-inflammatory response will be triggered followed by immune cells forming encapsulated granuloma. This will lead to a cascade effect and to possible active TB.[5]

*Mtb* is aerobic, non-motile, 1–10 µm in length, a rod shaped bacillus and intracellular pathogen that multiplies within macrophages. The bacterium triggers the production of free radicals but avoids being killed by the same radicals. Pathogenic *Mtb* can exist in dormant

form, latent TB, where no symptoms of the disease are shown. These patients cannot transmit the disease but they have a lifelong risk of TB reactivation.[6] *Mtb* is resistant to disinfectants and Gram's stain due to its complex cell wall with high molecular weight lipids. The pathogen is gram positive but the wax-rich cell wall lends the bacilli acid fast properties. The cell wall glycolipids and mycolic acids are responsible for some of the immune responses. *Mtb* can bind to a variety of host cell receptors such as surfactant protein receptors and macrophage receptors.[4] A brief overview of the *Mtb* lifecycle is illustrated in Figure 2.1.

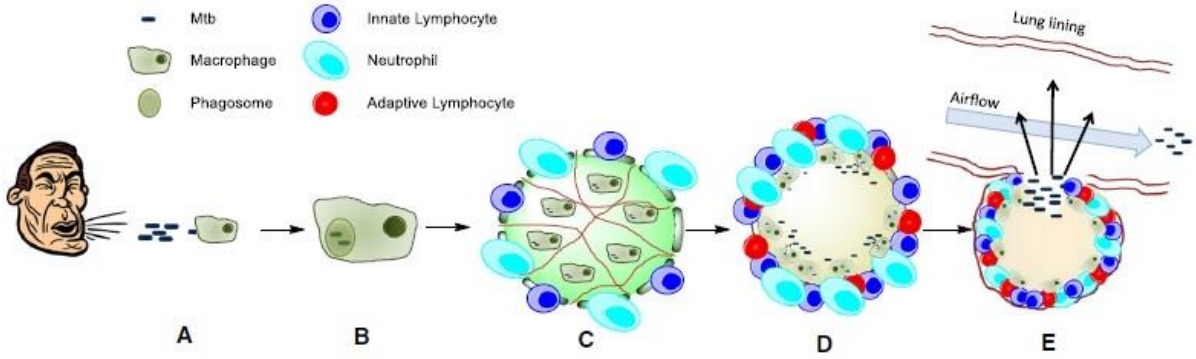


Figure 2.1: An overview of the Mtb life cycle.[5]

## 2.3 Diagnosis of TB

Strong government commitment and financing as well as community engagement are necessary in order to diagnose and manage TB. Currently there is a shortage in diagnostic tools and infrastructure in developing countries. Treatment is available to most TB patients but stock-outs and other delays in especially rural areas can result in ongoing transmission. The majority of multidrug-resistant cases have been treated but the cure rate is only 50%. There is thus a need for safer, shorter, and more efficacious diagnosis and drug administration.[1] TB is diagnosed via clinical symptoms and chest radiography followed by laboratory results for confirmation. New diagnostic techniques have been developed but an accurate and reliable testing method is however not currently available. A "Gold standard" to detect and diagnose TB is thus yet to be found. Microscopic examination of sputum is widely used as it is rapid, inexpensive and allows quantitative estimation of the number of bacilli. It is however unable to distinguish tuberculosis bacilli from non-tuberculosis mycobacteria, and has a low sensitivity. Decontamination using N-acetyl-L-cysteine (NALC) and sodium hydroxide kills contaminating bacteria in sputum samples.[7] Positive sputum smear samples should however undergo molecular testing such as polymerase chain reaction (PCR),

transcription amplification, ligase chain reaction and strand displacement amplification to confirm TB infection.[4] Nucleic acid amplification tests provide faster results than acid-fast bacilli culture (using Ziehl–Neelsen or hematoxylin–eosin (H&E) staining) and has a higher sensitivity compared to sputum smear microscopy. Samples stained with Ziehl–Neelsen use conventional light microscopy. Fluorescent microscopy stains consisting of a mixture of auramine O and rhodamine B dyes binds to the nucleic acids within acid-fast bacilli as seen in Figure 2.2. Fluorescent staining has shown to be more sensitive and the slides can be read more rapidly compared to Ziehl-Neelsen staining. The WHO has thus endorsed a phase out of conventional Ziehl–Neelsen light microscopy in favour of auramine-rhodamine acid-fast bacilli staining. For molecular detection methods the amount of sputum can have a direct impact on the sensitivity of the test.[8,9,7] The tests to detect previous exposure to the *Mtb* is the tuberculin skin test or purified protein derivate (PPD), enzyme-linked immunosorbent assay (ELISA) test and interferon gamma release assay.

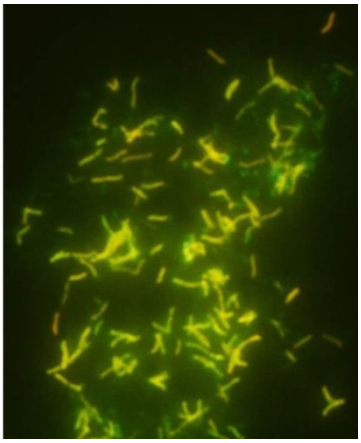

Figure 2.2: Acid-fast bacilli stain: *Mtb* stained with fluorescent auramine-rhodamine stain.[7]

The limitations of diagnostic techniques are due to the low concentration of bacilli in samples as well as difficulty to detect immunology markers associated with *Mtb*. In order to obtain high specificity and low minimum detection limits, complex and expensive equipment are often needed. The equipment and trained personnel also adds to the running costs and feasibility. The WHO recorded 5.2 million cases of pulmonary tuberculosis in 2014. It was found that only 58% of the cases were confirmed by laboratory methods such as smear or culture. The remaining 42% of patients were however only diagnosed by clinical criteria (symptom history or chest X-ray). The findings are thus an indication that the availability of diagnostic tools is limited.[7] Fast, effective, and lower cost diagnostic analysis is thus of importance.

For effective TB diagnosis *Mtb* has to be identified within a sample of bodily fluid obtained from a patient. The samples are most commonly found in respiratory specimens such as sputum, bronchial aspirates and bronchoalveolar lavage fluid. Tissues, normally sterile body fluids, blood, and urine can however also be analyzed. Infants and young children have difficulty coughing expectorated sputum. Sputum can be induced using saline with an ultrasonic nebulizer. Swallowed sputum can be obtained via gastric lavage but acidic gastric washings may decrease the viability of mycobacteria. Bronchoalveolar lavage (BAL) fluid can be obtained during a bronchoscopy but this method is invasive.[7] The diagnosis of TB is especially hampered in children due to the low concentration of bacilli in obtained samples, low rate of positive culture and smear tests due to paucibacillary TB, lack of definitive diagnostic methods and variable clinical symptoms.[10] A large amount of sample is needed for an accurate TB diagnosis. Alternatively the *Mtb* bacilli can be concentrated within the sample and extracted.

Accurate and fast *Mtb* detection can be realized by obtaining good quality samples. The collected sample must have a high concentration of *Mtb* present, irrespective of the analysis technique used. A large sample volume or multiple samples is thus needed to obtain a high concentration.[11] Alternatively a smaller volume can be used if the *Mtb* is concentrated within the sample. Nanotechnology and polymer science in conjunction with known molecular and cellular interactions can be used to improve the diagnostic success of TB.

## 2.4 Nanotechnology

Nanotechnology refers to the design, synthesis and application of matter at a molecular scale. Nanoscale refers to dimensions and tolerances of less than 100 nanometers and the possibility of manipulation of individual atoms and molecules. Nanotechnology has revolutionized science for several decades - improvements have been made in the fields of medicine and biology with regard to drug delivery, medical diagnostics and manufacturing. Recent research has demonstrated its potential application to novel forms of disease detection and treatment. Nanotechnology has been used to change the mechanisms by which drugs are delivered and its application to scaffolds for nerve regeneration has been investigated. Research regarding the mechanisms and characteristics of medical nanoparticles and nanofibers has highlighted the pharmacologic potential in improving drug synthesis and carriers as well as the optimization of materials and reducing toxicity.[12] Nanotechnology enables the improvement of diagnostic techniques resulting in high throughput screening and possible point-of-care (POC) diagnostics.[13]

Previous research has been conducted that focussed on the optimization of existing TB test methods. Nanotechnology was utilized to synthesize affinity substrates to enable the capture and concentration of *M. tuberculosis* for improved diagnosis. In a study by Cronje, poly(styrene-*co*-maleic anhydride) (SMA) functionalized with a $C_{12}$ aliphatic quaternary ammonium moiety was found to have the most effective affinity for BCG as well as *M. tuberculosis.*[14] In a similar study by Du Plessis, poly(styrene-*alt*-maleic anhydride) (SMA) functionalized with Con A captured BCG most effectively due to saccharide binding of the protein. SMA modified with aliphatic quaternary ammonium moieties of chain lengths $C_8$-$C_{12}$ also showed capturing abilities through ionic and hydrophobic interactions.[15] Quaternized chitosan nanofibers and coated iron oxide nanoparticles where investigated with regards to BCG affinity by Fortuin. It was found that chitosan coated nanoparticles functionalized with a $C_{12}$ aliphatic quaternary ammonium moiety (CS-q$C_{12}$), captured the most BCG. *N*-trimethylammonium chitosan chloride (TMC) blended with PVA, to produce nanofibers crosslinked with genipin, were found to have the strongest interaction with BCG of the nanofibers.[16]

Nanofibers and nanoparticles have a high surface area to volume ratio and a porous structure which enables the use as affinity substrates.[17,18] A nanoscale substrate, such as nanofibers and nanoparticles, with *Mtb* affinity can be used to concentrate the bacteria in the sample. The sample volume needed will thus be less and will aid in diagnostic analysis. Magnetic nanoparticles coated with a polymer that has affinity for *Mtb* can be used to concentrate the bacilli in the sample. The bacilli can be captured by the coated polymer and the magnetic iron oxide nanoparticles can adhere to an external magnet. An external magnetic field can thus be used to remove the concentrated bacteria from the sample.

### 2.4.1 Nanoparticles

Nanoparticles have unique properties compared to the bulk due to quantum effects at nanoscale. The properties of nanoparticles are influenced by the size and microstructural details of the core and the surface. Three main approaches are used to create nanomaterials namely the top-down, bottom-up and virtual approach. The top-down approach has been the traditional approach for miniaturization utilizing lithography. The bottom-up approach entails the self-assembly from molecular precursors in chemical solutions. The virtual approach technique is used by the computational theorists where new materials are created in computer simulations. Magnetism differs in some materials when one or more dimensions are reduced. The reduction in dimensions can result in the reduction of coordination number of atoms, reducing the hopping tendency of electrons from site to site. The kinetic energy (bandwidth) of electrons is also reduced and Coulomb

interactions/bandwidth ratio is enhanced, which enhances magnetism. The appearance of surface and interface states due to the reduced symmetry and changed boundary conditions plays an important role in inducing the magnetism in the materials of reduced dimensions.[19]

Nanoparticles can be used in numerous fields, including physics and chemistry. The reduced dimensions of solid materials lead to novel, modifiable physical and chemical properties that differ from the bulk material. The ultra-small nanosize has revolutionized science as application to drug delivery, contrast enhancers in magnetic resonance imaging (MRI) and antimicrobial agents to kill bacteria resistant to antibiotics.[18] The Massart's method can be used to produce nanoparticles with a diameter less than 20 nm. These superparamagnetic iron oxide nanoparticles (SPIONs) have shown high field irreversibility and high saturation field.[20] These qualities enable the particles to no longer show magnetic interaction after the external magnetic field is removed. This broadens the application of the nanoparticles in controlled magnetism as well as giving larger structures magnetic properties.

Biocompatibility and toxicity of SPIONs are important criteria for the use in biomedical applications. Biocompatibility is determined by the magnetic responsive component (such as, magnetite, iron, nickel, cobalt, neodymium–iron–boron or samarium–cobalt), the final size of the particles (including the core), the coatings and the stability at neutral pH. The nanoparticles must have a high magnetization in order to control the movement of the particles in a sample with a magnetic field. Highly magnetic metals such as cobalt and nickel are toxic and susceptible to oxidation and can thus not be used. For biomedical applications iron oxide particles such as magnetite ($Fe_3O_4$) or its oxidised form maghemite ($\gamma$-$Fe_2O_3$) are most commonly used.[20] Iron is polymorphic in nature with multiple oxidation states. Iron oxide nanoparticles will have different crystal structures depending on the oxidation state (Fe(II) or Fe(III)), $Fe_3O_4$ has a cubic inverse spinel structure.

For this study magnetite will be synthesized due to its superparamagnetic properties as well as ease of synthesis via co-precipitation. The surface of the nanoparticles can be coated with a polymer as seen in biomedical applications.[21]

## 2.5 Magnetite

Magnetite ($Fe_3O_4$) and maghemite ($\gamma$-$Fe_2O_3$) are iron oxides which possess similar face centred cubic close-packed structure and are of interest due to their magnetic and biological properties as well as half-metallic behaviour.[22] Magnetite is, however, the polymorph that shows the strongest magnetic properties.[23]

### 2.5.1 Synthesis

Magnetic (magnetite) nanoparticles can be synthesized via co-precipitation with bases, micro emulsions, thermal decomposition and/or reduction, micelle synthesis, sol-gel, and hydrothermal synthesis.[24] Co-precipitation is a simple method and commonly used to synthesize magnetic nanoparticles by titrating aqueous Fe(II)/Fe(III) salt solutions with a base under inert atmosphere. Co-precipitation is favourable due to the large gram-scale product that can be formed. The size, shape, and composition of the magnetic nanoparticles can be controlled by the type of salts used (chlorides, sulfates or nitrates), the Fe(II)/Fe(III) ratio, the reaction temperature, the pH and ionic strength of the solution.[25] $Fe_3O_4$ is thermodynamically stable under ambient laboratory conditions and forms readily under most solvent based nanoparticles synthesis conditions. The bulk material is redox active, while the surface composition is easily varied by slight changes to $O_2$ partial pressure and substrate temperatures. The surface of $Fe_3O_4$ nanoparticles are often covered with a multilayer of α-$Fe_2O_3$ (hematite) due to exposure to the ambient atmosphere and, as with most oxides, monolayer amounts of surface hydroxyl and physically adsorbed water.[26]

### 2.5.2 Structure

Magnetite has a face centred cubic (inverse) spinel structure, based on 32 $O^{2-}$ ions, close-packed along the [111] direction as seen in Figure 2.3. $Fe_3O_4$ contains divalent and trivalent iron, contrary to other iron oxides. The cubic inverse spinel structure consists of a cubic close packed array of oxide ions, where all the $Fe^{2+}$ ions occupy half of the octahedral sites and the $Fe^{3+}$ are split evenly across the remaining octahedral sites and the tetrahedral sites. The stoichiometry of magnetite is Fe(II)/Fe(III) = 1/2, where the divalent ions may be partly or fully replaced by other divalent ions (Co, Mn, Zn, etc). This lends magnetite *n*- and *p*-type semiconductor characteristics. Magnetite however has the lowest resistivity among iron oxides due to its small bandgap (0.1 eV).[27]

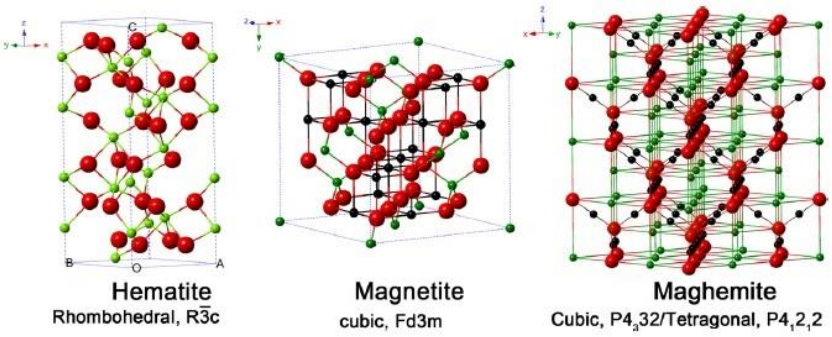


Figure 2.3: Crystal structure of hematite, magnetite and maghemite (black ball = $Fe^{2+}$, green ball = $Fe^{3+}$ and red ball =$O^{2-}$).

### 2.5.3 Crystal growth

The precipitation of nanoparticles from solution is a fundamental method of crystallisation where nucleation and crystal growth are the principle pathways for solid formation. Using this method the nuclei can grow uniformly by diffusion from the solution to the nanoparticle surfaces. Monodispersed nanoparticles can be formed by uniform nucleation followed by crystal growth without further nucleation. Multiple nucleations can however occur and result in uniform nanoparticles by Oswald ripening (large uniform crystals formed by crystal growth through the dissolution of small crystallites). Larger sized particles that are uniform can also be obtained by aggregation of small crystallites through coalescence. Crystal growth in solution is interface-controlled up to a certain critical size and beyond that size, the growth is diffusion controlled.[20] Co-precipitation occurs via the LaMer mechanism defined by a short burst of nucleation from a supersaturated solution followed by slow growth of particles without notable additional nucleation. Magnetic nanoparticles can, based on Brownian relaxation and Néel relaxation theory as seen in Figure 2.4, produce heat accompanied with the relaxation process of nanoparticles. Magnetic nanoparticles are magnetized and the magnetic moment is gradually arranged via this synthesis.[28]

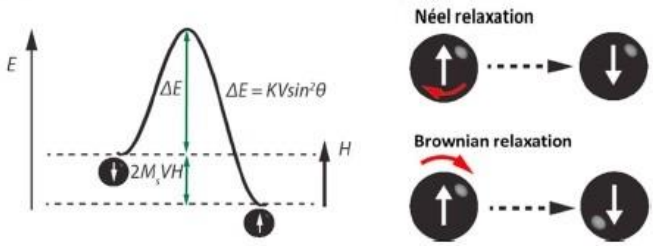


Figure 2.4: The energy barriers governing single domain particles (left) and the relaxation processes that influence the heating properties of magnetic nanoparticles (right). [29]

### 2.5.4 Magnetism

Magnetization describes the strength of the magnetic dipole moment of the magnetic nanoparticles at a certain magnetic field strength quantified as magnetic moment per volume of core material. The magnetic moment (depending on the core material) follows characteristic saturation behaviour. The magnetic behaviour of the nanoparticles is dependent on magnetic dipole interaction. A material with unpaired electrons will be paramagnetic and will be attracted by an external magnetic field. Paramagnetic ions in close proximity to each other will be influenced by the alignment of the magnetic dipoles. These ions can be ferrimagnetic, ferromagnetic or antiferromagnetic. A ferromagnetic material will have temporary magnetism due to the alignment of magnetic moments of the ions.[30]

### 2.5.5 Nanoscale magnetism effects

The magnetic properties of nanoparticles vary significantly from bulk materials in magnetic moment and anisotropy due to the influence of surface region atoms. The surface region atoms determine the magnetic properties of the system as a whole. The magnetic properties of magnetic nanoparticles can be either modified or deteriorated by size reduction. These properties include saturation magnetization and hysteresis loop (field irreversibility). Physicochemical and synthesis parameters, however, also affect magnetism. Ferri- or ferromagnetic nanoparticles will exhibit superparamagnetic behaviour in the regions smaller than their magnetic domains. Superparamagnetism is a transition from a ferri- or ferromagnetic state towards paramagnetic behaviour with high susceptibility and saturation magnetization.[23] The critical size of the superparamagnetic transition depends on the value of the effective magnetic anisotropy constant. In colloidal suspensions of superparamagnetic nanoparticles or magnetic fluids the net magnetic attraction is greatly reduced due to thermally induced randomization of the individual nanoparticles' magnetic moments.[31] These particles thus show better dispersion in solution as they do not tend to magnetically interact with each other to form aggregates. Their magnetic susceptibility, however, still remains high. Superparamagnetic nanoparticles exhibit zero remanence (and coercivity) and will thus have zero average magnetism in the absence of an applied external magnetic field as seen in Figure 2.5. [25]

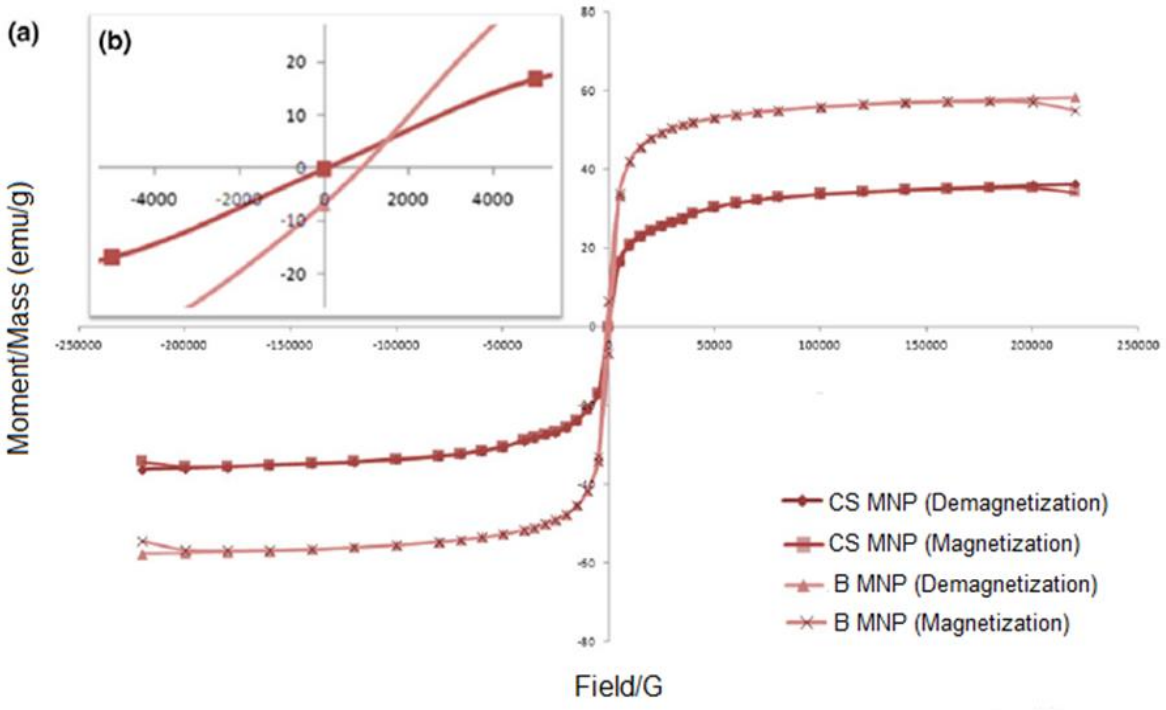


Figure 2:5: a) Magnetic hysteresis loops of pristine iron oxide SPMNs and chitosan coated SPMNs b) enlargement of the centre of the hysteresis loops.[32]

### 2.5.6 Coated SPMNs

Magnetic nanoparticles show attraction towards one another which leads to aggregation. Coating the nanoparticles with various organic and inorganic shells enhances air or thermal stability, dispersion and reduces core loss of composites. It is, however, seen that the saturation magnetism is lowered leading to weaker magnetism.[33] Surfactants and polymers can be used to coat the nanoparticles which improve dispersion in solution and binds functional groups to the surface of the nanoparticles.[34] These functional groups can be used for further functionalization such as binding a protein, ligand or drug. Polymers can physically adsorb onto the surface of nanoparticles via electrostatic interactions, hydrophobic interactions and hydrogen bonding.

Polymers with functional groups such as hydroxyl, amine and carboxyl groups can adsorb onto nanoparticle surfaces. Multifunctional magnetic composites have been synthesized by surface modification of iron oxide nanoparticles. Iron oxide has hydroxyl groups that can be used for further functionalization. Polymers with amino groups such as chitosan can adhere to the surface of iron oxide nanoparticles. Whereas iron oxide nanoparticles modified with aminosilane are able to further functionalize with SMA.

Coating nanoparticles with a functional polymer can improve the stability, surface charge, functionality and targeting capability. The nanoparticles thus form less aggregates whilst broadening the end use. Depending on the polymer of choice amino groups, carboxylic acids, phosphates and sulphates can be bound to the surface of the nanoparticles. The coated nanoparticles will be stable in aqueous solution and can thus be applied to biological applications. Chitosan and SMA have shown to be biological compatible and can thus be modified and used for its BCG capturing capabilities.[35]

## 2.6 Chitosan

Chitosan is the *N*-deacetylated derivative of chitin, although the *N*-deacetylation is rarely complete. The structure of chitosan is composed of 2-amino-2-deoxy-β-d-glucopyranose (GlcN) and β(1→4)-linked 2-acetamido-2-deoxy-β-d-glucopyranose (GlcNAc) residues. A sharp distinction in nomenclature with respect to the degree of *N*-deacetylation between chitin and chitosan has however not been defined. Chitosan are of interest in commercial use due to its high percentage of nitrogen (6.89%) compared to synthetically substituted cellulose (1.25%). Chitosan can thus be used as a chelating agent. There is, however, a limitation with regard to its reactivity and processability. Chitosan is obtained from crab or shrimp shells and fungal *mycelia*. Chitin production is supplied by food industries such as shrimp canning. Whereas chitosan–glucan complexes are produced from fermentation

processes (of *Aspergillus niger*, *Mucor rouxii*, and *Streptomyces*) which involves alkali treatment.[36]

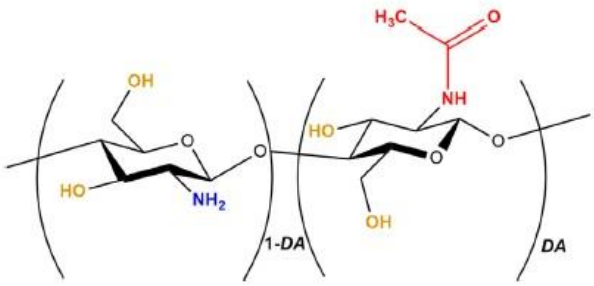


Figure 2.6: Chemical structure of chitosan (1-DA (degree of acetylation)) (left) and chitin (DA =1) (right).[37]

Chitosan consists of hydroxyl and amino groups, and possesses favourable properties, including non-toxicity, biodegradability, biocompatibility and bioactivity. These advantages lead to chitosan based materials being widely used in the biomedical field.[38] With tissue engineering however, its application is limited due to its relative hydrophobicity and common bacterial infection after surgery.[39] Most naturally occurring polysaccharides (cellulose, dextran, pectin, alginic acid, agar, agarose and carragenans) are neutral or acidic, whereas chitin and chitosan are highly basic.[40] This property allows polyoxysalt formation, film formation, the ability to chelate metal ions and optical structural characteristics.

Chitosan is soluble in dilute acids such as acetic acid and formic acid. The nitrogen content of chitosan is due to its primary aliphatic amino groups. Chitosan can thus undergo reactions typical of amines, including *N*-acylation and Schiff reactions. Chitosan derivatives can be obtained under mild conditions and is considered to be substituted glucans. At room temperature, chitosan forms aldimines with aldehydes. *N*-alkyl chitosan can be produced by hydrogenation of chitosan and simple aldehydes. The presence of substituents weakens the hydrogen bonds of chitosan; *N*-alkyl chitosans can thus swell in water despite the hydrophobicity of the alkyl chains.[36]

Introducing quaternary groups on the chitosan backbone renders the polymer soluble over a wider pH range and enables strong cationic activity.[41] From previous studies, it has been reported that quaternized chitosan derivatives exhibit higher antimicrobial and antimycotic activity compared to pristine chitosan.[42] The incorporation of quaternized chitosan in electrospun nanofibers and nanoparticles will thus impart high antibacterial and antimycotic activity. Polycations present due to quaternization are able to bind to the cytoplasmic membrane of bacterial cells. The charge density of the polyelectrolyte increases with an

increase in the molecular weight, which leads to the enhanced adsorption of polycations onto the negatively charged cell surface.[43]

## 2.7 SMA

Poly(styrene-*alt*-maleic anhydride) (SMA) is a linear molecular chain polymer with regular alternating non-polar styrene and polar, reactive maleic anhydride. It has favourable properties such as low toxicity, low cost, and good biocompatibility and biodegradation. Modified SMA copolymers have been used as surface active agents, microbicides, external dopants, drug carriers, and sorbent for removal of heavy metal ions.[44] SMA can be used to synthesize micro- and nanostructured materials through self-organization. Micelles can also be obtained by emulsion polymerization followed by using as latexes. Capsules of SMA can be formed utilizing a combination with gelatin or dodecanol. Templates can be formed utilizing the mesoscopic self-assembling morphology of SMA films.[45]

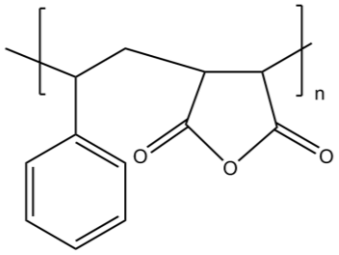


Figure 2.7: Chemical structure of SMA.

SMA can be synthesized via conventional free radical copolymerization. SMA is soluble in a variety of solvents, depending on the ratio of styrene and maleic anhydride, due to the combination of polar and nonpolar monomers. Styrene and maleic anhydride has been copolymerized in *N*,*N*-dimethylformamide (DMF) in previous studies.[46] SMA is a thermoplastic with a high heat resistance and good dimensional stability, qualities which are ideal for modification.[47]

SMA can be functionalized and the degree of hydrophilicity modified through reaction with alcohols for esterification, amines for antibacterial activity and alkali.[45] The reactive maleic anhydride units can undergo nucleophilic addition with amine compounds due to ring-opening. SMA undergoes self-emulsification after addition of a nucleophile. The nucleophile can react with the maleic anhydride units and therefore introduce functional groups into the polymer chain. Tertiary amine and quaternary ammonium compounds have shown antimicrobial activity as well as bacterial adhesion.[48]

Quaternized chitosan and SMA derivatives are thus polymers that indicate applicability in biological applications. Both polymers are biocompatible and have cellular adhesion properties necessary for bacterial affinity substrates. Nanomaterials such as nanoparticles and nanofibers can be utilized as substrates due to their enhanced properties. Quaternized chitosan and SMA can be electrospun into nanofibers with a large surface area to volume ratio. Iron oxide nanoparticles can chelate quaternized chitosan and quaternized SMA, forming coated magnetic nanoparticles.

## 2.8 Electrospinning

Nanofibers are fibers produced in the submicron range due to processing of the polymer solution. Electrospinning has received increasing attention due its favourable properties and is considered to be a vital scientific and commercial venture with global economic benefits. Various techniques are implemented for the production of nanomaterials; including drawing-processing, template-assisted synthesis, self-assembly, solvent casting, phase separation, and electrospinning. Electrospinning is used the most frequently to produce nanofibers due to a high surface area to volume ratio and large number of inter-/intra-fibrous pores. Nanofibers are frequently used in the biomedical field using biocompatible and biodegradable (natural or synthetic) polymers.[49] A high loading of bacterial microbes per unit mass can be obtained due to the large number of inter- and intra-fibrous pores.

The basic single needle electrospinning setup includes a syringe containing polymer solution (attached to a pump for constant flow), metallic needle, power supply, and metallic collector. The pumped polymer solution is charged via the metallic needle, which causes instability in the polymer solution droplet. The reciprocal repulsion of charges produces a force that opposes the surface tension, leading to polymer solution flow in the direction of the electric field. A further increase in electric field causes the spherical droplet to deform into a conical shape. Ultrafine nanofibers emerge from the conical polymer droplet (Taylor cone) and are collected on the metallic collector (kept at optimal distance). A stable charge jet will be able to form when the polymer solution has sufficient cohesive force. The internal and external charge forces cause whipping of the polymer solution jet in the direction of the collector. This whipping motion stretches and slides the polymer chains past each other within the solution, leading to nanofibers.[50]

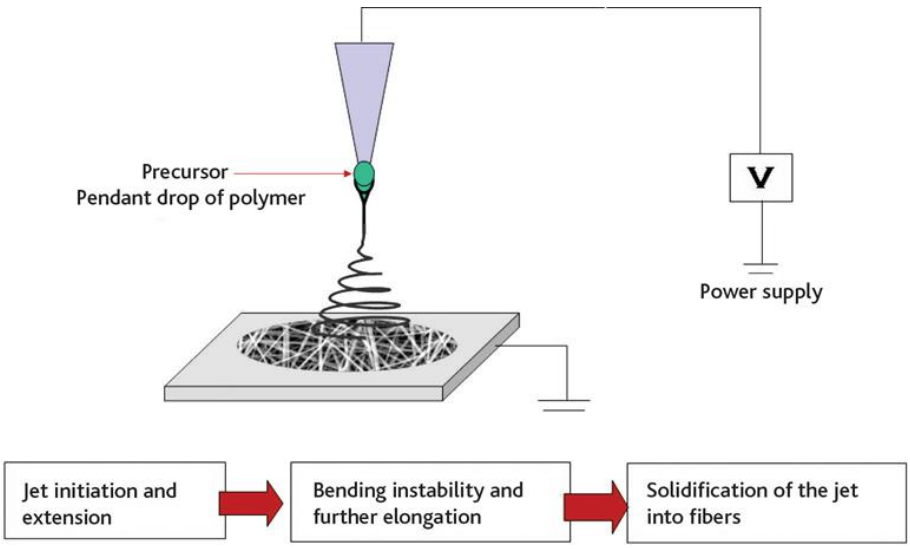


Figure 2.8: Principle of electrospinning.[51]

Factors that influence fiber formation that should be optimised during experiments include the electrospinning setup (applied electric field, distance between the needle and collector and flow rate), solution (solvent, polymer concentration, viscosity and solution conductivity) and environmental (humidity and temperature) parameters.[17]

## 2.9 Conclusion

In conclusion, the characteristics, methods of infection and diagnosis of tuberculosis have been summarized. The difficulties diagnosing TB as well as the requirements for an accurate TB diagnosis was discussed. The main problem in diagnosis is the large specimen volume needed to obtain an acceptable bacterial yield. Nanotechnology in the form of nanofibers and nanoparticles in conjunction with polymer science can be used to address the issue of diagnosing TB.

## 2.10 References

1. Schito, M., Hanna, D. & Zumla, A. Tuberculosis Eradication versus Control. *Int. J. Infect. Dis.* **56,** 10–13 (2017).
2. Gebreegziabher, S. B., Bjune, G. A. & Yimer, S. A. Patients' and health system's delays in the diagnosis and treatment of new pulmonary tuberculosis patients in West Gojjam Zone, Northwest Ethiopia: a cross-sectional study. *BMC Infect. Dis.* **16,** 673 (2016).
3. Baghaei, P., Tabarsi, P., Jabehdari, S., Marjani, M., Moniri, A., Farnia, P. & Velayati, A. A. HIV and tuberculosis trends and survival of coinfection in a referral center in Tehran: A 12-year study. *Int. J. Mycobacteriology* **5,** S16–S17 (2016).
4. Yepes, J. F., Sullivan, J. & Pinto, A. Tuberculosis: Medical management update. *Oral Surgery, Oral Med. Oral Pathol. Oral Radiol. Endodontology* **98,** 267–273 (2004).

5. Hoagland, D. T., Liu, J., Lee, R. B. & Lee, R. E. New agents for the treatment of drug-resistant *Mycobacterium tuberculosis*. *Adv. Drug Deliv. Rev.* **102,** 55–72 (2016).

6. Chinsembu, K. C. Tuberculosis and nature's pharmacy of putative anti-tuberculosis agents. *Acta Trop.* **153,** 46–56 (2016).

7. Caulfield, A. J. & Wengenack, N. L. Diagnosis of active tuberculosis disease: From microscopy to molecular techniques. *J. Clin. Tuberc. Other Mycobact. Dis.* **4,** 33–43 (2016).

8. Fisher, M., Dolby, T., Surtie, S., Omar, G., Hapeela, N., Basu, D., DeWalt, A., Kelso, D., Nicol, M. & McFall, S. Improved method for collection of sputum for tuberculosis testing to ensure adequate sample volumes for molecular diagnostic testing. *J. Microbiol. Methods* **135,** 35–40 (2017).

9. Lee, C. N., Wang, Y. M., Lai, W. F., Chen, T. J., Yu, M. C., Fang, C. L., Yu, F. L., Tsai, Y. H., Chang, W. H. S., Zuo, C. S. & Renshaw, P. F. Super-paramagnetic iron oxide nanoparticles for use in extrapulmonary tuberculosis diagnosis. *Clin. Microbiol. Infect.* **18,** E149–E157 (2012).

10. Ki, H. P. & Shingadia, D. Tuberculosis in children. *Paediatr. Child Health (Oxford).* **27,** 109–115 (2017).

11. Gray, J. W. Childhood tuberculosis and its early diagnosis. *Clin. Biochem.* **37,** 450–455 (2004).

12. Garimella, R. & Eltorai, A. E. M. Nanotechnology in orthopedics. *J. Orthop.* **14,** 30–33 (2017).

13. Boisseau, P. & Loubaton, B. Nanomedicine, nanotechnology in medicine. *Comptes Rendus Phys.* **12,** 620–636 (2011).

14. Cronje, L. Surface modification of styrene maleic anhydride nanofibers for efficient capture of *Mycobacterium tuberculosis*. (Stellenbosch University, South Africa, 2012).

15. du Plessis, A. Functionalized Polymer Nanofibrous Substrates as Capturing Platforms for Mycobacteria. (Stellenbosch University, South Africa, 2016).

16. Fortuin, L. Modified chitosan nano-substrates for mycobacterial capture. (Stellenbosch University, South Africa, 2015).

17. Homayoni, H., Ravandi, S. A. H. & Valizadeh, M. Electrospinning of chitosan nanofibers: Processing optimization. *Carbohydr. Polym.* **77,** 656–661 (2009).

18. El-Zowalaty, M. E., Al-Ali, S. H. H., Husseiny, M. I., Geilich, B. M., Webster, T. J. & Hussein, M. Z. The ability of streptomycin-loaded chitosan-coated magnetic nanocomposites to possess antimicrobial and antituberculosis activities. *Int. J. Nanomedicine* **10,** 3269–3274 (2015).

19. Singh, R. Unexpected magnetism in nanomaterials. *J. Magn. Magn. Mater.* **346,** 58–73 (2013).

20. Mahmoudi, M., Sant, S., Wang, B., Laurent, S. & Sen, T. Superparamagnetic iron oxide nanoparticles (SPIONs): Development, surface modification and applications in chemotherapy. *Adv. Drug Deliv. Rev.* **63,** 24–46 (2011).

21. Cuong, N. D., Hoa, T. T., Khieu, D. Q., Lam, T. D., Hoa, N. D. & Van Hieu, N. Synthesis, characterization, and comparative gas-sensing properties of $Fe_2O_3$ prepared from $Fe_3O_4$ and $Fe_3O_4$-chitosan. *J. Alloys Compd.* **523,** 120–126 (2012).

22. Bezdorozhev, O., Kolodiazhnyi, T. & Vasylkiv, O. Precipitation synthesis and magnetic properties of self-assembled magnetite-chitosan nanostructures. *J. Magn. Magn. Mater.* **428,** 406–411 (2017).

23. Shaterabadi, Z., Nabiyouni, G. & Soleymani, M. High impact of in situ dextran coating on biocompatibility, stability and magnetic properties of iron oxide nanoparticles. *Mater. Sci. Eng. C* **75,** 947–956 (2017).

24. Su, C. Environmental implications and applications of engineered nanoscale magnetite and its hybrid nanocomposites: A review of recent literature. *J. Hazard. Mater.* **322,** 48–84 (2017).

25. Borlido, L., Azevedo, A. M., Roque, A. C. A. & Aires-Barros, M. R. Magnetic separations in biotechnology. *Biotechnol. Adv.* **31,** 1374–1385 (2013).

26. Bagheri, S. & Julkapli, N. M. Modified iron oxide nanomaterials: Functionalization and

application. *J. Magn. Magn. Mater.* **416,** 117–133 (2016).

27. Wu, W., Wu, Z., Yu, T., Jiang, C. & Kim, W. Recent progress on magnetic iron oxide nanoparticles: synthesis, surface functional strategies and biomedical applications. *Sci. Technol. Adv. Mater.* **16,** 23501 (2015).

28. Li, Y., Hu, K., Chen, B., Liang, Y., Fan, F., Sun, J., Zhang, Y. & Gu, N. $Fe_3O_4$@PSC nanoparticle clusters with enhanced magnetic properties prepared by alternating-current magnetic field assisted co-precipitation. *Colloids Surfaces A Physicochem. Eng. Asp.* **520,** 348–354 (2017).

29. Abenojar, E. C., Wickramasinghe, S., Bas-Concepcion, J. & Samia, A. C. S. Structural effects on the magnetic hyperthermia properties of iron oxide nanoparticles. *Prog. Nat. Sci. Mater. Int.* **26,** 440–448 (2016).

30. Heidsieck, A., Schmid, D. & Gleich, B. Measurement of magnetic moment via optical transmission. *J. Magn. Magn. Mater.* **401,** 511–516 (2016).

31. Gyergyek, S., Makovec, D., Jagodič, M., Drofenik, M., Schenk, K., Jordan, O., Kovač, J., Dražič, G. & Hofmann, H. Hydrothermal growth of iron oxide NPs with a uniform size distribution for magnetically induced hyperthermia: Structural, colloidal and magnetic properties. *J. Alloys Compd.* **694,** 261–271 (2017).

32. Unsoy, G., Yalcin, S., Khodadust, R., Gunduz, G. & Gunduz, U. Synthesis optimization and characterization of chitosan coated iron oxide nanoparticles produced for biomedical applications. *J. Nanoparticle Res.* **14,** (2012).

33. Yang, B., Li, X., Yang, X. & Yu, R. Chemical synthesis of Fe/$Fe_3O_4$ core-shell composites with enhanced soft magnetic performances. *J. Magn. Magn. Mater.* **428,** 6–11 (2017).

34. Chandra, A., Turng, L. S., Li, K. & Huang, H. X. Fracture behavior and optical properties of melt compounded semi-transparent polycarbonate (PC)/alumina nanocomposites. *Compos. Part A Appl. Sci. Manuf.* **42,** 1903–1909 (2011).

35. Dias, A. M. G. C., Hussain, A., Marcos, A. S. & Roque, A. C. A. A biotechnological perspective on the application of iron oxide magnetic colloids modified with polysaccharides. *Biotechnol. Adv.* **29,** 142–155 (2011).

36. Kumar, M. A review of chitin and chitosan applications. *React. Funct. Polym.* **46,** 1–27 (2000).

37. Jerushan, J., Paul, M., Leeuwen, V., Cottet, H., Castignolles, P. & Gaborieau, M. Determination of the distributions of degrees of acetylation of chitosan. *Int. J. Biol. Macromol.* **95,** 40–48 (2017).

38. Safee, N. H. A., Abdullah, P. & Othman, M. R. Synthesis and characterization of carboxymethyl chitosan-$Fe_3O_4$ Nanoparticles. in *Prosiding Seminar Kimia Bersama UKM-ITB VIII 9-11 Jun 2009* 474–480 (2009).

39. Liu, Y., Lv, H., Qin, Y., Deng, L. & Wang, Y. Gentamicin modified chitosan film with improved antibacterial property and cell biocompatibility. *Int. J. Biol. Macromol.* **98,** 550–556 (2017).

40. Rafique, A., Zia, K. M., Zuber, M., Tabasum, S. & Rehman, S. Chitosan functionalized poly(vinyl alcohol) for prospects biomedical and industrial applications: A review. *Int. J. Biol. Macromol.* **87,** 141–154 (2016).

41. Wang, T. W., Xu, Q., Wu, Y., Zeng, A. J., Li, M. & Gao, H. Quaternized chitosan (QCS)/poly (aspartic acid) nanoparticles as a protein drug-delivery system. *Carbohydr. Res.* **344,** 908–914 (2009).

42. Ignatova, M., Manolova, N., Toshkova, R., Rashkov, I., Gardeva, E., Yossifova, L. & Alexandrov, M. Quaternized chitosan-coated nanofibrous materials containing gossypol: Preparation by electrospinning, characterization and antiproliferative activity towards HeLa cells. *Int. J. Pharm.* **436,** 10–24 (2012).

43. Kim, C. H., Choi, J. W., Chun, H. J. & Choi, K. S. Synthesis of chitosan derivatives with quaternary ammonium salt and their antibacterial activity. *Polym. Bull.* **38,** 387–393 (1997).

44. Li, Y., Nie, W., Chen, P. & Zhou, Y. Preparation and characterization of sulfonated poly(styrene-*alt*-maleic anhydride) and its selective removal of cationic dyes. *Colloids Surfaces*

*A Physicochem. Eng. Asp.* **499,** 46–53 (2016).

45. Schoukens, G., Martins, J. & Samyn, P. Insights in the molecular structure of low- and high-molecular weight poly(styrene-maleic anhydride) from vibrational and resonance spectroscopy. *Polym. (United Kingdom)* **54,** 349–362 (2013).

46. Xiang, T., Tang, M., Liu, Y., Li, H., Li, L., Cao, W., Sun, S. & Zhao, C. Preparation and characterization of modified polyethersulfone hollow fiber membranes by blending poly (styrene-*alt*-maleic anhydride). *Desalination* **295,** 26–34 (2012).

47. Cronje, L., Warren, R. & Klumperman, B. pH-dependent adhesion of mycobacteria to surface-modified polymer nanofibers. *J. Mater. Chem. B* **1,** 6608–6618 (2013).

48. Cloete, W. J., Verwey, L. & Klumperman, B. Permanently antimicrobial waterborne coatings based on the dual role of modified poly(styrene-*co*-maleic anhydride). *Eur. Polym. J.* **49,** 1080–1088 (2013).

49. Haider, A., Haider, S. & Kang, I. A comprehensive review summarizing the effect of electrospinning parameters and potential applications of nanofibers in biomedical and biotechnology. *Arab. J. Chem.* (2015). doi:10.1016/j.arabjc.2015.11.015

50. Yoo, H. S., Kim, T. G. & Park, T. G. Surface-functionalized electrospun nanofibers for tissue engineering and drug delivery. *Adv. Drug Deliv. Rev.* **61,** 1033–1042 (2009).

51. Ramakrishna, S., Fujihara, K., Teo, W. E., Yong, T., Ma, Z. & Ramaseshan, R. Electrospun nanofibers: Solving global issues. *Mater. Today* **9,** 40–50 (2006).

# Chapter 3

Synthesis and characterization of precursor polymers

## 3.1 Introduction

Chitosan has favourable properties such as low toxicity, good biodegradability and biocompatibility. It has shown cellular adhesion as well as anti-bacterial qualities which is favourable in biomedical applications. Chitosan is insoluble in water, alkali, and most mineral acidic solutions. Chitosan is, however, soluble in organic acids, such as dilute aqueous acetic, formic acid and lactic acids.[1] The primary amino and hydroxyl groups on the polymer backbone can be utilized as nucleophiles for chemical modification. Modified chitosan imparts functional properties which broadens possible applications.[2] Nucleophilic substitution via the amino groups enables acetylation, iminization, alkylation, quaternization and metal chelation.

Modifying chitosan can alter the hydrophilicity thereof due to additional side chains. Quaternized chitosan has shown anti-microbial activity where an increase in the quaternary ammonium moiety content and chain length of the alkyl substituent increases the anti-bacterial properties.[3] The increase in anti-microbial activity can be attributed to an increase in hydrophobicity. The hydrophobicity and cationic charge due to quaternization thus has a substantial effect on the antibacterial activity and thus cellular adhesion/affinity.[4] Concanavalin A (Con A) is a well-studied carbohydrate-binding protein and human receptor for the carbohydrate-based structures on the surface of *Mtb*, such as mannose. The interaction between the human receptors of Con A and mycobacterial mannose can facilitate the capture and concentration of *Mtb*.[5] To facilitate Con A binding to chitosan, linker molecules are utilized viz. glutaraldehyde (GLU), glycine (GLY) and *N*-(3-dimethylaminopropyl)-*N′*-ethylcarbodiimide hydrochloride (EDC).

Poly(styrene-*alt*-maleic anhydride) (SMA) has favourable properties such as low toxicity, low cost, and good biocompatibility and biodegradation. SMA can be functionalized and the degree of hydrophilicity modified through reaction with amines for antibacterial activity.[6] The reactive maleic anhydride units can undergo nucleophilic addition with amine compounds due to ring-opening. SMA undergoes self-emulsification after addition of a nucleophile. The nucleophile can react with the maleic anhydride units and therefore introduce functional groups into the polymer chain.[7]

## 3.2 Results and discussion

In this chapter the characterization of pristine chitosan (Addendum A) and the synthesis and characterization of quaternized *N*-alkyl chitosan derivatives (CS-qC$_{10}$ and CS-qC$_{12}$) and CS-GLU-GLY-EDC/CS-EDC (chitosan-glutaraldehyde-glycine-EDC) will be discussed as well as the synthesis and characterization of SMA and the quaternized derivatives of SMA (SMI-qC$_{10}$ and SMI-qC$_{12}$). ATR-FTIR, $^{1}$H-NMR and $^{13}$C-NMR spectroscopy was used for characterization. These polymers were chosen for their possible adhesion to the cell wall of *Mycobacterium tuberculosis (Mtb).*

### 3.2.1 CS-qC$_{10}$ and CS-qC$_{12}$

*N*,*N*-(2-dimethyl)propyl-3-*N',N'*-dimethyl-*N'*-decylammonium chitosan chloride (CS-qC$_{10}$) and *N*,*N*-(2-dimethyl)propyl-3-*N',N'*-dimethyl-*N'*-dodecylammonium chitosan chloride (CS-qC$_{12}$) were synthesized via a two-step reaction. In the first step *N*-substituted CS were produced by modifying chitosan with a suitable modification agent (3-dimethylamino-2,2-dimethylpropanal). For the second step, the tertiary amine was quaternized with 10-carbon and 12-carbon bromoalkane chains, respectively. The chemical structures of the synthesized quaternized chitosan derivatives can be seen in Figure 3.1. The two polymers differed only by two carbon atoms in the alkyl chain and thus had similar FTIR and NMR spectra, only CS-qC$_{12}$ will thus be illustrated. The syntheses of these polymers were confirmed by characterization via ATR-FTIR, $^{1}$H-NMR and $^{13}$C-NMR spectroscopy.

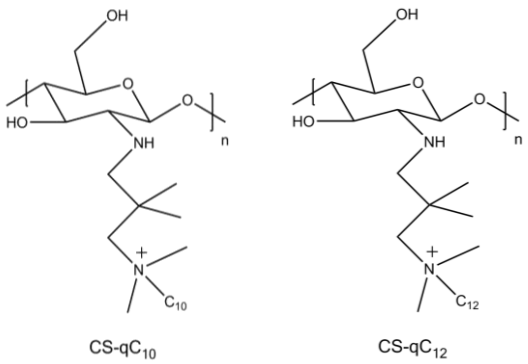


Figure 3.1: Chemical structures of CS-qC$_{10}$ and CS-qC$_{12}$.

#### a) ATR-FTIR

Figure 3.2 represents the FTIR spectra of pristine chitosan, *N*-substituted chitosan and CS-qC$_{12}$.

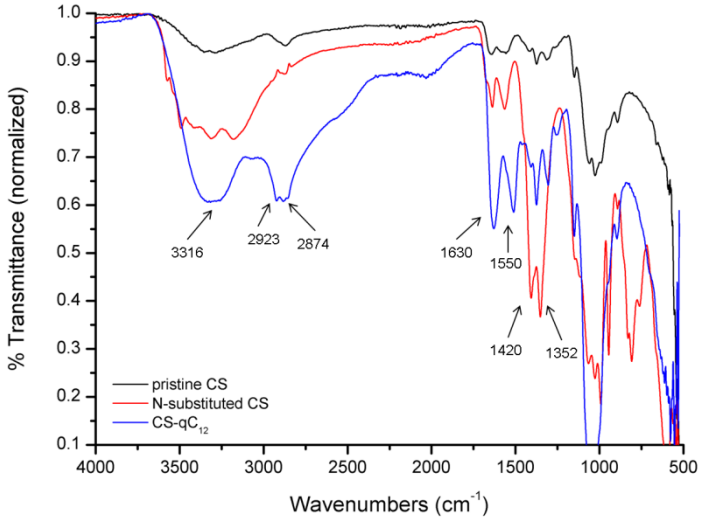


Figure 3.2: FTIR spectra of pristine chitosan, *N*-substituted chitosan and CS-qC$_{12}$.

From the FTIR spectra of pristine chitosan, *N*-substituted chitosan and its quaternized derivatives (Figure 3.2), the peak at 1550 cm$^{-1}$ can be assigned to the primary amine groups (N-H bend). The peak at 1630 cm$^{-1}$ was assigned to the carbonyl stretch of chitosan's acetamido moiety on the *N*-acetylglucosamine (chitin) residue. The C=O bond of the amide I increases dramatically in intensity after *N*-substitution and quaternization due to the formation of a more stable amide bond and a decrease in intramolecular hydrogen bonding of the amide, hydroxyl and amino groups of chitosan.[8] The primary amine peak also increases after modification but less compared to the carbonyl peak.[9]

A broad absorption band between 3050 and 3600 cm$^{-1}$ (O-H, N-H stretch) were observed for chitosan, *N*-substituted chitosan and the quaternized chitosan derivatives. The bands at 2923 and 2874 cm$^{-1}$ (C-H stretch) were present in the quaternized chitosan derivatives due to the alkyl chains. The presence of alkyl chains were corroborated by the bending absorption of the methyl and methylene groups at 1352 and 1420 cm$^{-1}$. These bands increased in intensity in the spectra of CS-qC$_{10}$ and CS-qC$_{12}$ compared to pristine chitosan and also confirmed the inclusion of long aliphatic chains onto the polymer backbone. The C-O stretch at 1050 cm$^{-1}$ increased in intensity after chemical modification.[4]

**b) $^{1}$H-NMR**

The $^{1}$H NMR spectrum of CS-qC$_{12}$ is shown in Figure 3.3. The peak at 5.02 ppm can be assigned to the methine H-1 as seen in pristine chitosan. A broad overlapping peak can be seen for the chitosan polymer backbone H-9, H-10, H-3, H-4, H-6, H-5 and H-6' at 4.08-3.59 ppm. The peaks at 3.47 and 3.29 ppm can be assigned to H-7 and H-11 while the peaks at

2.82 ppm can be assigned to the H-2 proton. The peak at 2.06 ppm can be assigned to the protons attached to the two methyl groups (H-22 and H-23). The peak at 2.21 ppm can be assigned to the protons attached to the two methyl carbons of the quaternary amine, deshielded by the electron withdrawing nitrogen atom. The peaks at 1.78 and 1.29 ppm can be assigned to the inner protons of the alkyl chain added during quaternization. The peak at 1.10 ppm can be assigned to the methyl protons of the acetyl of β(1→4)-linked 2-acetamido-2-deoxy-β-d-glucopyranose (GlcNAc). The peak at 0.88 ppm can be assigned to the terminal methyl protons of the alkyl chain H-21.

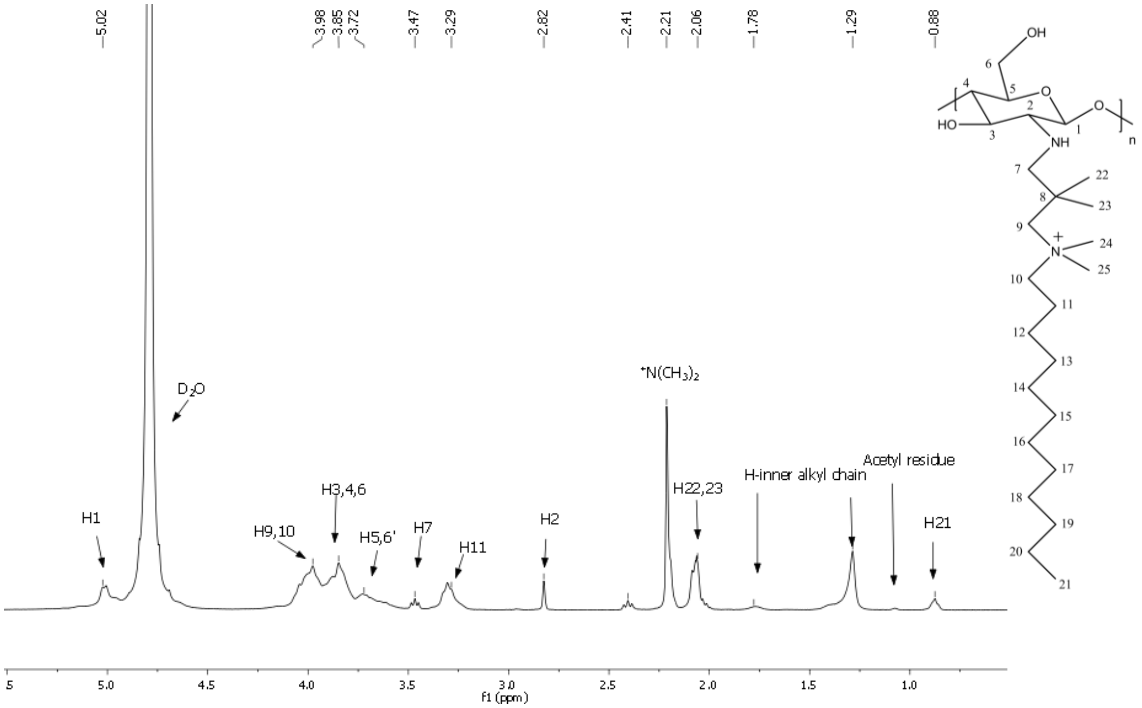


Figure 3.3: $^{1}$H-NMR spectrum of CS-qC$_{12}$ at 80 ˚C in D$_2$0/acetic acid-d4 (70:30, v/v).

The degree of quaternization (DQ %) could be determined from the $^{1}$H-NMR spectra of the quaternized derivatives. The percentage quaternization is determined by the integral of the methine (H-2, 2.82 ppm) proton in relation to the integral area of the residual acetyl (1.1 ppm), as seen by Equation 3.1.[10]

$$\mathrm{DQ}\ \% = 1 - \left( \frac{\frac{\mathrm{CH_3\ (res.\,acetyl)}}{3}}{\mathrm{H-2}} \right) \times 100 \qquad 3.1$$

The DQ % was calculated to be 94 % for CS-qC$_{10}$ and 96 % for CS-qC$_{12}$.

### c) $^{13}$C-NMR

Compared to pristine chitosan, quaternized chitosan (Figure 3.4) had additional upfield signals. The chemical shift at 53.1 ppm can be assigned to the carbons of the quaternary amine group, while the signal at 33.7 can be assigned to the two methyl carbons (C-22 and C-23).[4] The signals at 32.2 ppm can be assigned to the methylene carbons of the inner alkyl chain, 20.0 ppm can be assigned to the terminal methyl carbons of the alkyl chain C-21.

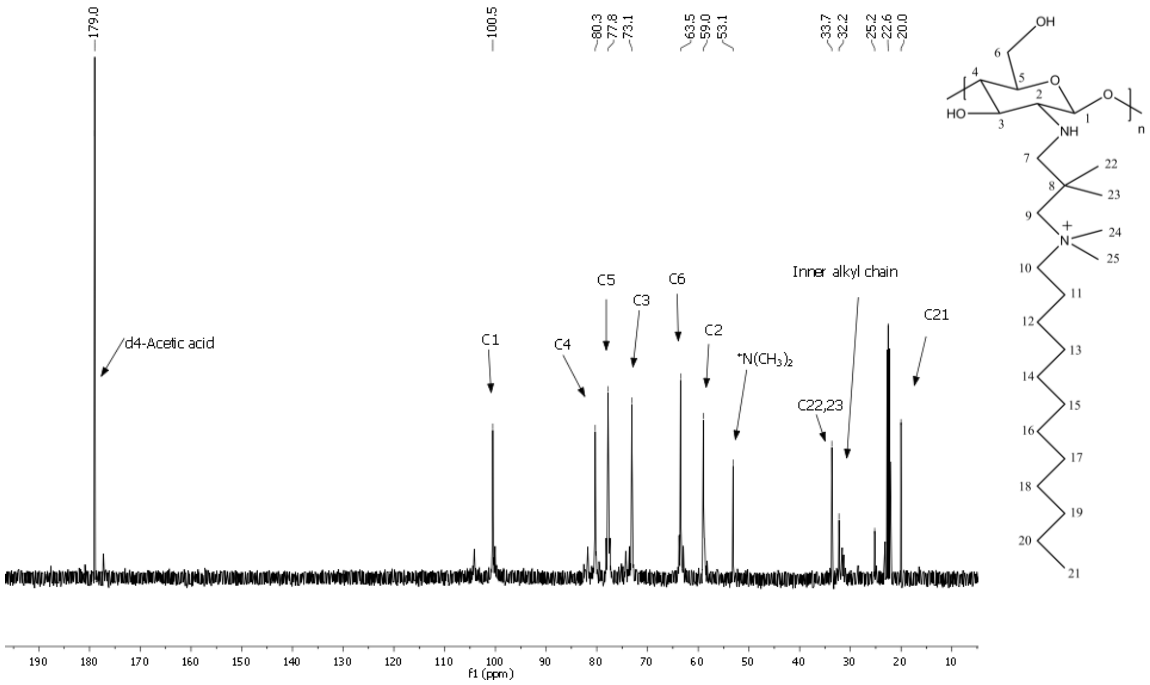


Figure 3.4: $^{13}$C-NMR spectrum of CS-qC$_{12}$ at 80 ˚C in D$_2$0/acetic acid-d4 (70:30, v/v).

### 3.2.2 CS-EDC

Pristine chitosan was modified with linker molecules (CS-EDC) in order to immobilize Con A. Chitosan was crosslinked with glutaraldehyde followed by activating with glycine and 1-ethyl-3-(3-dimethylaminopropyl) carbodiimide (EDC). Epichlorohydrin can be used to covalently bond glycine to the crosslinked chitosan.[11] Carbodiimide forms a urea derivative, *O*-acylisourea, between the carbodiimide and carboxylic group of glycine. The primary amines of Con A can displace *O*-acylisourea via nucleophilic substitution resulting in an amide bond and thus protein immobilization.[12] The synthesis of CS-EDC was confirmed by characterization via ATR-FTIR, $^{13}$C solid-state cross polarization magic-angle-spinning (CP-MAS) and SP (single pulse) MAS NMR spectroscopy. Solid state NMR analysis was utilized due to crosslinking of chitosan during modification making the material insoluble per solution state NMR.

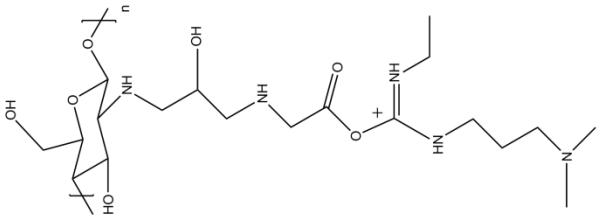

Figure 3.5: Chemical structure of CS-EDC.

**a) ATR-FTIR**

Figure 3.6 represents the FTIR spectra of pristine chitosan, CS-GLU-GLY and CS-GLU-GLY-EDC.

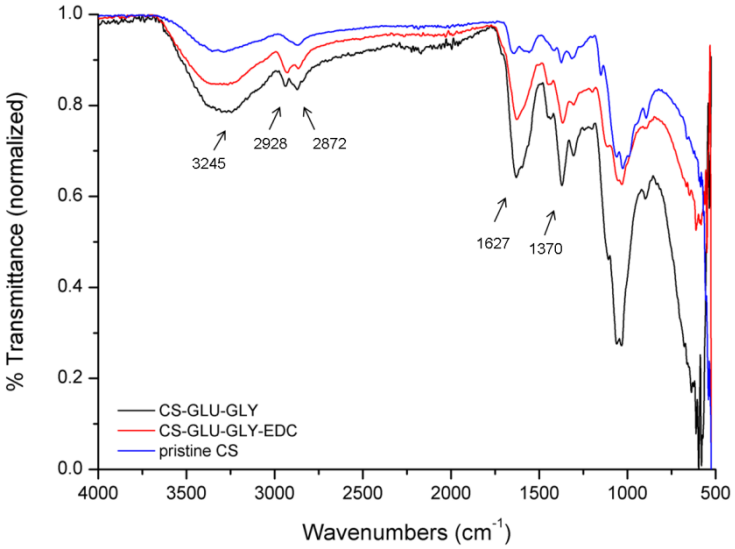


Figure 3.6: FTIR spectra of pristine CS, CS-GLU-GLY and CS-GLU-GLY-EDC.

The peak at 1627 $cm^{-1}$ was assigned to the C=O stretching vibration and the intensity increases after crosslinking chitosan with glutaraldehyde as well as the addition of the linker molecules glycine and EDC. The increase in intensity can be attributed to the addition of C=O bonds in the form of aldehyde, carboxyl and stable carbodiimide groups. The N-H bend absorption band at 1550 $cm^{-1}$, attributed to the free amino groups of pristine chitosan, disappeared after chemical modification due to crosslinking.[13] The broad absorption band between 3000 and 3600 $cm^{-1}$ was assigned to the (O-H, N-H stretch) of pristine chitosan as well as crosslinked chitosan. Bands at 2928 and 2872 $cm^{-1}$ (C-H stretch) were present after crosslinking chitosan due to the alkyl groups of glycine and EDC. Characteristic bending

absorptions of the methyl and methylene groups at 1320 and 1370 $cm^{-1}$ also corroborate the alkyl groups.

### b) Solid state $^{13}$C-NMR

The characteristic peaks of pristine chitosan could be seen in Figure 3.7. From the SP-MAS $^{13}$C-NMR spectrum, the chemical shift at 106.6 ppm can be assigned to C-1 while the characteristic peak for C-4 appears at 83.7 ppm. A small C-F rotor background signal can be seen at 112.3 ppm. Two overlapping peaks can be seen for C-5 and C-3 as well as for C-6 and C-2 at 75.8 and 61.4 ppm respectively. The peak at 22.9 ppm can be assigned to the $CH_3$ (acetyl) of residual chitin.[14] At 43.5 ppm a side band of the larger signals occurred due to the 5 kHz MAS rate spinning. The side band is prevalent for the O-C-O groups. The SP spectrum showed protons with more quantitative relative intensities of the mobile and rigid regions. The peak at 61.4 ppm of C-6 and C-2 thus had the greatest intensity. The CP-MAS $^{13}$C-NMR (Figure 3.8) spectrum had similar signals but discriminated against protons with low proton proximal densities or high mobilities.

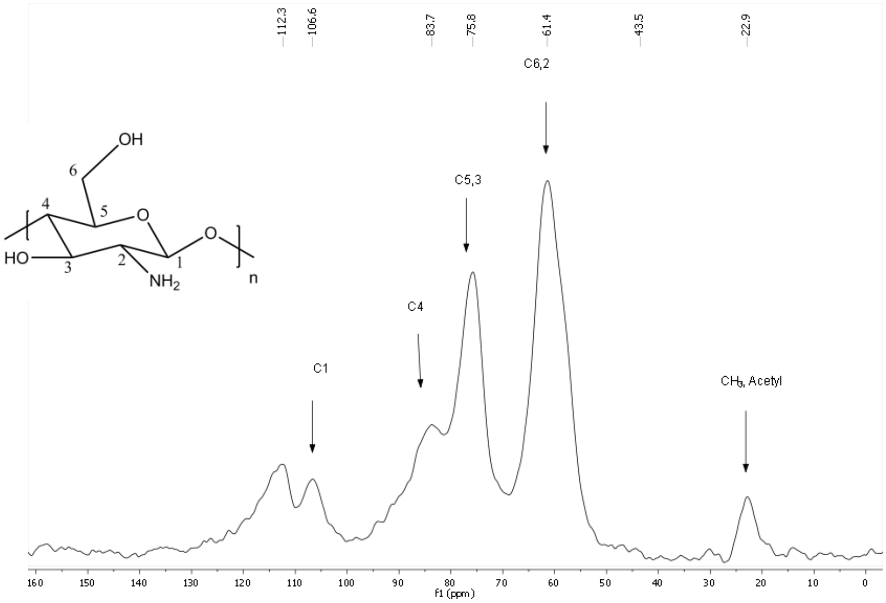


Figure 3.7: SP-MAS $^{13}$C-NMR spectrum of chitosan.

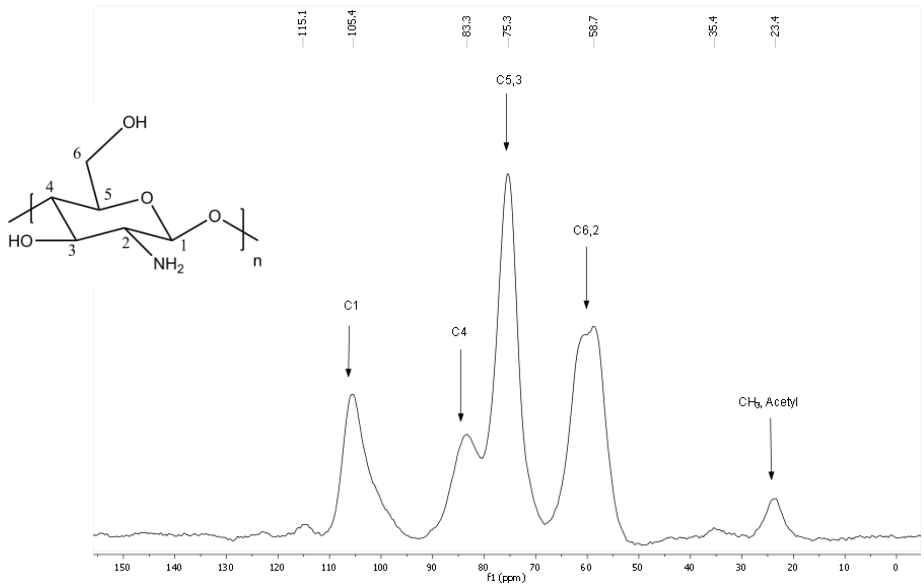


Figure 3.8: CP-MAS $^{13}$C-NMR spectrum of chitosan.

From the SP-MAS $^{13}$C-NMR spectrum of CS-EDC (Figure 3.9) broader signals can be seen due to more rigidity (faster $T_2$ relaxation). The rigidity is attributed to the glutaraldehyde used as crosslinking agent as well as the modification agents. From the CP-MAS $^{13}$C-NMR spectrum of CS-EDC (Figure 3.10) additional broad peaks can be seen at 181.3 and 144.4 ppm. The signal at 181.3 ppm can be assigned to the carbonyl (C-11) as well as the carbonyl of glutaraldehyde.[15] The signal at 144.4 ppm can be assigned to the C=N (C-12) of the carbodiimide where the electronegative nitrogen atom leads to deshielding.[16] A broad band can be seen at 32.9 ppm which can be attributed to the $CH_2$ and $CH_3$ groups of the modification agents.

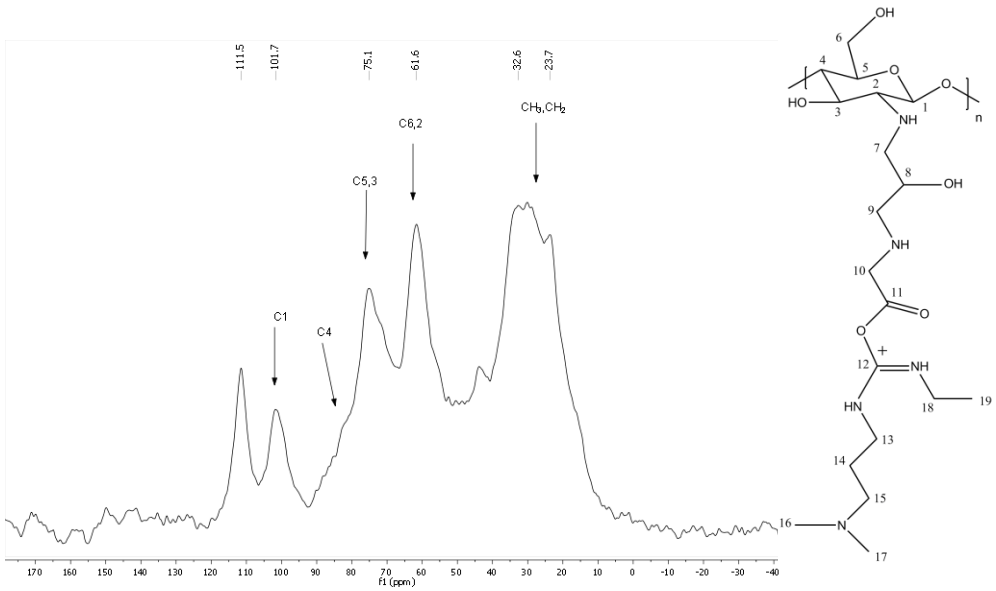


Figure 3.9: SP-MAS $^{13}$C-NMR spectrum of CS-EDC.

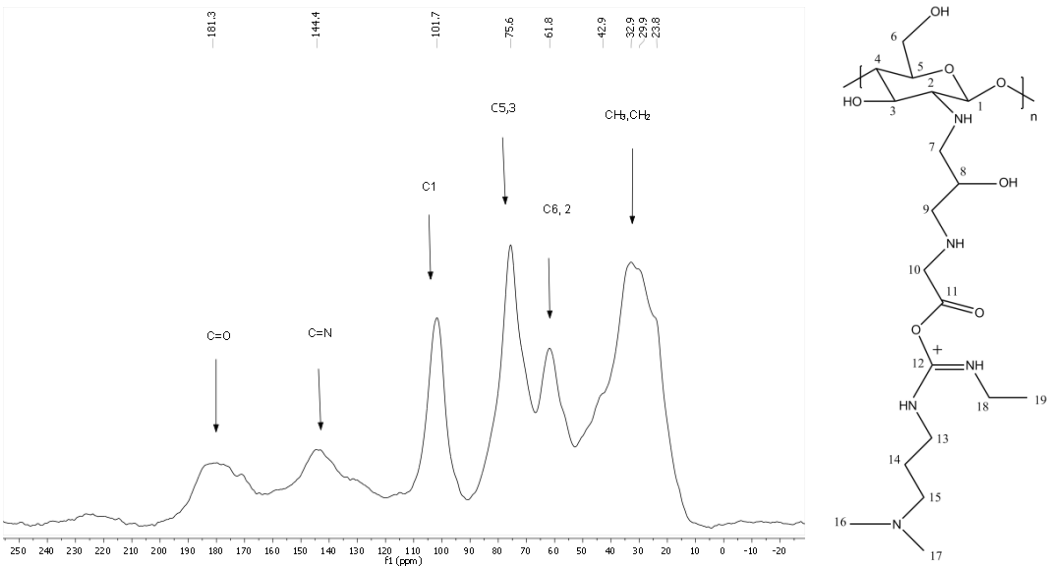


Figure 3.10: CP-MAS $^{13}$C-NMR spectrum of CS-EDC.

### 3.2.3 SMA

SMA was synthesized using conventional radical copolymerization which yielded an alternating copolymer as seen by Figure 3.11. The styrene and maleic anhydride will spontaneously arrange in an alternating sequence, as seen in radical polymerization mechanisms. SMA can be conveniently used as a precursor in the preparation of functional polymers. The reactive maleic anhydride can undergo a ring-opening reaction which enables chemical modification by linking active agents.[6] 3-(*N,N*-dimethylamino)-1-propylamine was used for the modification of SMA, where ring-opening of the maleic anhydride enabled nucleophilic addition of the primary amine. Heating at 170 ˚C enabled ring closure, thus resulting in the formation of styrene maleimide (SMI) (*N*-substituted maleimide). Addition of a bromoalkane resulted in quaternary ammonium SMI.

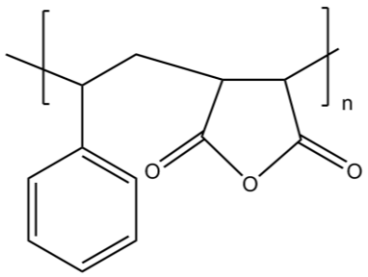


Figure 3.11: Chemical structure of SMA.

**a) ATR-FTIR**

Figure 3.12 represents the FTIR spectra of SMA, poly(styrene-[*N*-3-(*N',N'*-dimethylamino)propyl maleimide]) (SMI-tC) and SMI-qC$_{12}$.

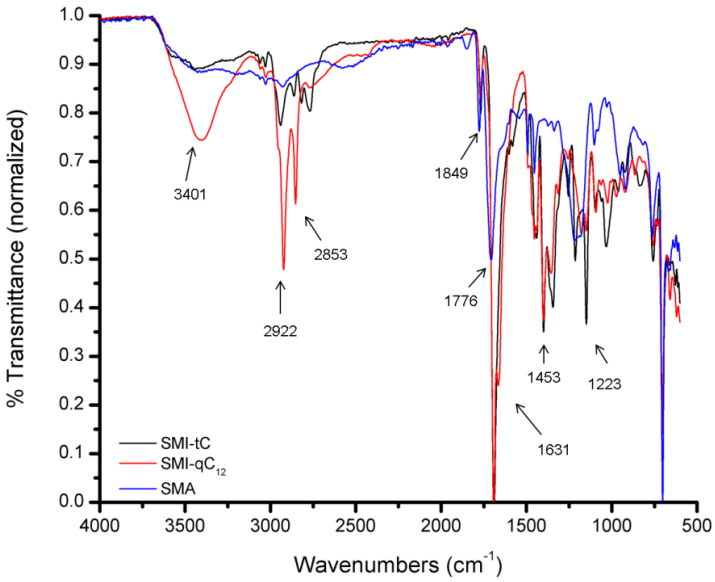


Figure 3.12: FTIR spectra of SMA, SMI-tC and SMI-qC$_{12}$.

From the FTIR spectra of SMA, the characteristic asymmetric and symmetric C=O stretch vibrations (1849 and 1776 cm$^{-1}$) of the cyclic maleic anhydride can be seen. An absorption band at 1223 cm$^{-1}$ can be seen for the cyclic ether (–C–O–C–) of the maleic anhydride residue. The absorption bands at 3027 and 2924 cm$^{-1}$ can be assigned to the aromatic methine and aliphatic methylene stretch vibrations and the bands at 1631 and 1453 cm$^{-1}$ can be assigned to the stretch vibrations (C=C) of the aromatic ring. The out-of-plane C-H bend vibrations of the monosubstituted aromatic ring can be assigned to the bands at 953 and 922 cm$^{-1}$.

From the FTIR spectra of SMI-tC, the (C=O) imide carbonyl asymmetric and symmetric stretch vibrations can be seen at 1768 and 1700 cm$^{-1}$. There is also a disappearance of the maleic anhydride residue bands at 1849 cm$^{-1}$.[17] The C-N vibration of the imide can be assigned to the peak at 1148 cm$^{-1}$. The smaller band cyclic ether (–C–O–C–) band at 1214 cm$^{-1}$ compared to the band of SMA at 1223 cm$^{-1}$ is an indication that some of the maleic anhydride reactive groups did not undergo imidization. Asymmetric and symmetric methyl and methylene stretching vibrations can be seen at 2922 and 2853 cm$^{-1}$ due to the alkyl groups incorporated via 3-(*N*,*N*-dimethylamino)-1-propylamine.

After quaternization (SMI-qC$_{10}$ and SMI-qC$_{12}$), an additional broad band appears between 3100 and 3600 cm$^{-1}$ due to the quaternary ammonium nitrogen. The tertiary amine (SMI-tC) undergoes nucleophilic substitution and resulting quaternization after the addition of a bromoalkane. An increase in the intensity of the bands at 2922 and 2853 cm$^{-1}$, is attributed to the methyl and methylene stretch vibrations of the alkyl chains.

The degree of quaternization (DQ %) of the quaternary derivatives could be determined from the ATR-FTIR spectra due to the reference peak at 702 cm$^{-1}$ (out of plane bending of the benzene ring) that remains constant during quaternization. The methyl groups of the *N*-alkyl amine moiety (SMI-tC), however, had a C-H band at 1344 cm$^{-1}$ that increased in intensity after quaternization (due to introducing alkyl chains). The DQ % could thus be calculated by the ratio of the peak height at 702 and 1344 cm$^{-1}$ for SMI-tC and the quaternized derivatives (SMI-qC$_{10}$ and SMI-qC$_{12}$) as seen by Equation 3.2.[18]

$$\mathrm{DQ\%} = \frac{\left(\text{peak height}\,\frac{704}{1350}\right)_{\mathrm{SMI-tC}}}{\left(\text{peak height}\,\frac{702}{1344}\right)_{\mathrm{SMI-qC_x}}} \times 100 \qquad 3.2$$

The DQ % was calculated to be 89 % for SMI-qC$_{10}$ and 88 % for SMI-qC$_{12}$.

**b) $^{1}$H-NMR**

From the $^{1}$H NMR spectrum of SMA (Figure 3.13) a characteristic single broad peak can be seen at 6.8 – 7.5 ppm due to the aromatic protons of the styrene unit. Protons attached to an aromatic ring are deshielded and will have large chemical shifts due to the large anisotropic field. The broad peak at 2.34 ppm corresponds to the chemical shift of the methylene and methine protons of the styrene polymer backbone. Whereas the broad, unresolved peak at 3.28 ppm can be attributed to the methine protons of the maleic anhydride polymer backbone. The maleic anhydride protons are attached to a carbon next to a carbonyl group (C=O) and will therefore have peaks downfield (compared to H-1,2) due to the electronegativity of the oxygen.[19]

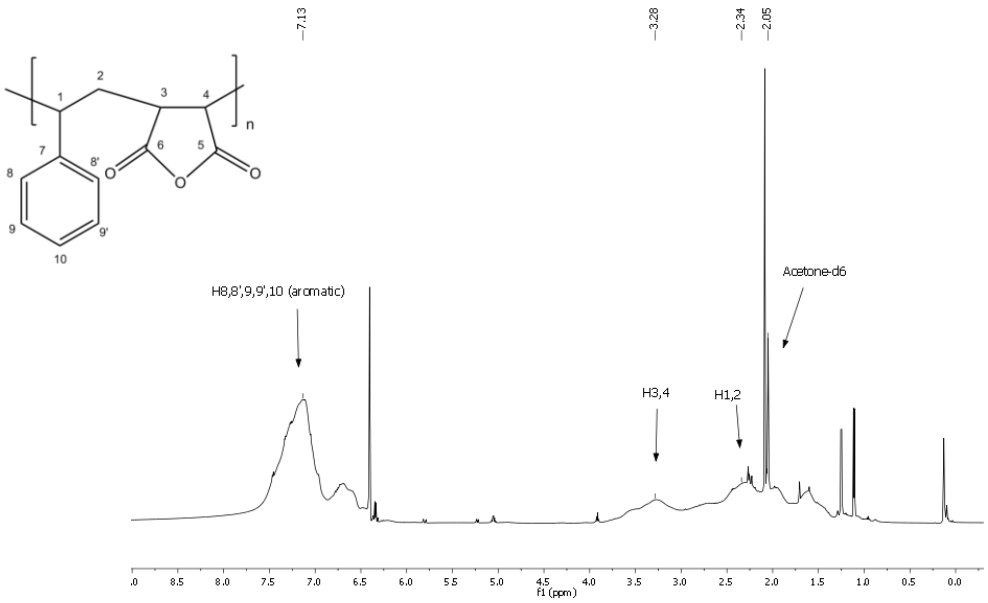


Figure 3.13: $^{1}$H-NMR of SMA in d-acetone.

### c) $^{13}$C-NMR

The $^{13}$C-NMR spectrum of SMA (Figure 3.14) has a characteristic peak at 173.6 ppm due to the carbonyl carbons of the maleic anhydride unit. The peaks at 128.8 ppm and 137.8 ppm are attributed to the aromatic ring carbons of the styrene unit (C-8,8',9,9',10) and the aromatic carbon (C-7) respectively. The peaks at 52.8 ppm, 43.5 ppm and 34.9 ppm are due to the aliphatic methylene and methine carbons of the SMA backbone (C-4, C-1, C-3, C-2). The $^{13}$C-NMR spectrum of SMA thus agrees with literature.[6]

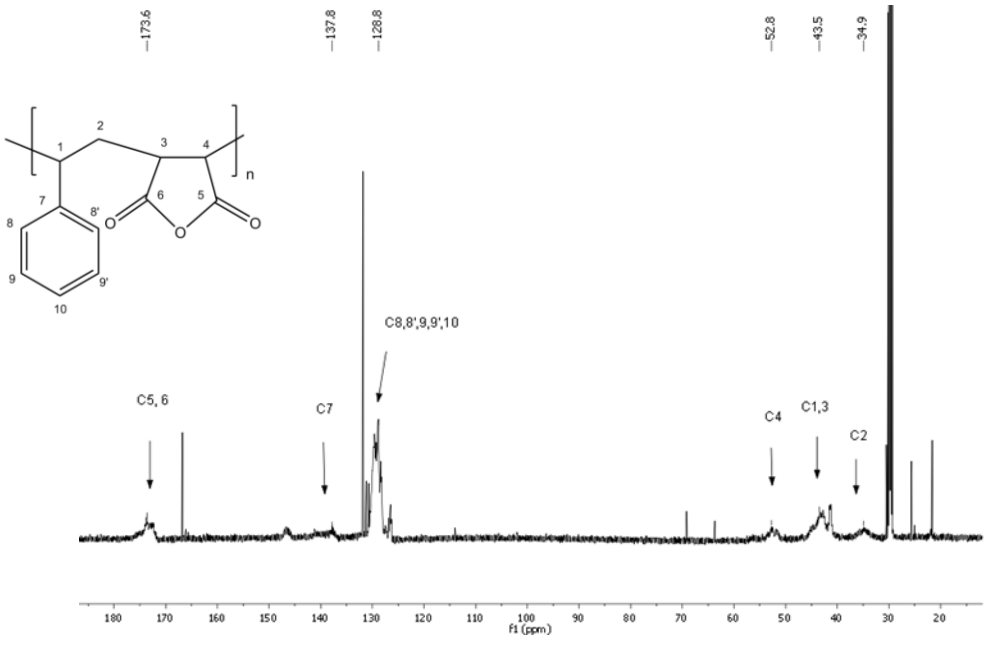


Figure 3.14: $^{13}$C-NMR of SMA in d-acetone.

### 3.2.4 SMI-tC

#### a) $^{1}$H-NMR

From the $^{1}$H-NMR spectrum of SMI-tC (Figure 3.15), a broad peak can be seen at 6.8-7.5 ppm attributed to the deshielded protons attached to the aromatic ring. The peak at 2.39 ppm is due to the methine of the styrene polymer backbone while the peak at 3.37 ppm is due to the deshielded methine protons of the maleic anhydride polymer backbone. Additional peaks in the upfield region can be seen for SMI-tC compared to SMA due to the imidization with 3-(*N*,*N*-dimethylamino)-1-propylamine. The terminal methyl groups are deshielded by the adjacent electron withdrawing nitrogen atom with a chemical shift at 2.15 ppm. The methylene protons (H-13) absorption peak overlaps at 2.15 ppm. The α-hydrogen (H-11) has a chemical shift at 2.94 ppm due to the adjacent nitrogen atom and electronegative carbonyl groups which lead to deshielding. The peak at 1.67 ppm can be attributed to the methylene absorption of the styrene polymer backbone with overlapping methylene absorption (H-12) of the alkyl chain.[20] The imidization of SMA with 3-(*N*,*N*-dimethylamino)-1-propylamine to yield SMI-tC was thus successful.

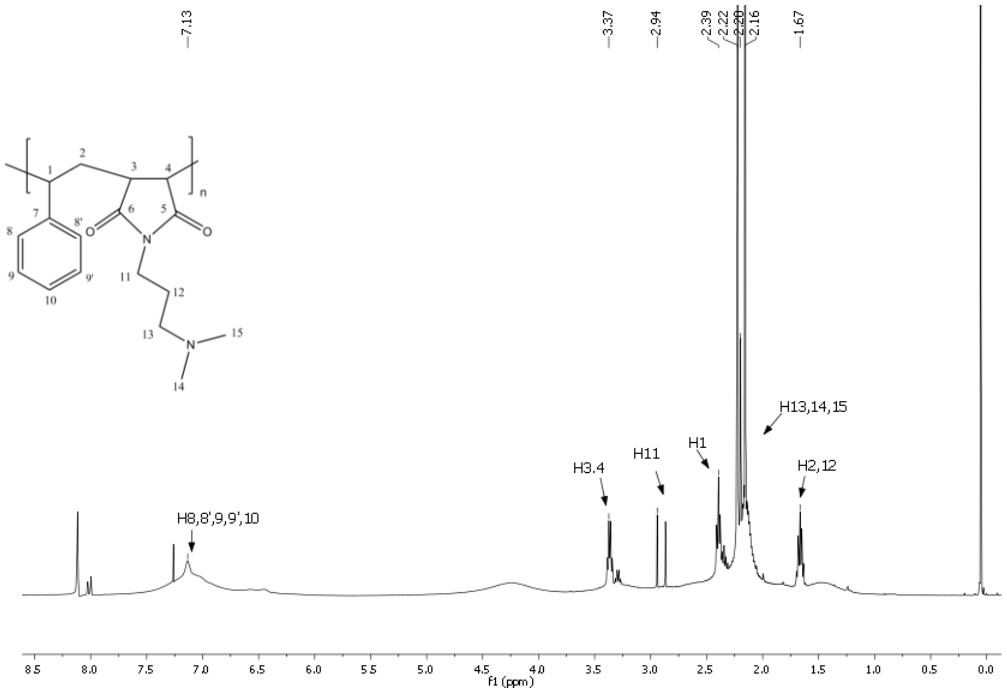


Figure 3.15: $^{1}$H-NMR of SMI-tC in d-chloroform.

### b) $^{13}$C-NMR

The $^{13}$C-NMR spectrum of SMI-tC is characterized by a peak at 178.4 ppm due to the imide carbonyl carbons. This peak is more downfield than the carbonyl peak of SMA due to imide formation. The peak at 128.8 ppm can be attributed to the aromatic ring carbons of the styrene unit. The peak at 38.0 ppm due to the methylene carbon adjacent to the imide nitrogen and the imide carbonyl peak at 178.4 confirm that imidization occurred, replacing the maleic anhydride with a maleimide unit. The primary *N*-alkylamine used for imidization of the maleic anhydride has characteristic peaks at 45.4 and 58.5 ppm due to the methyl carbons (C-14,15) and methylene carbons (C-13) adjacent to the nitrogen of the tertiary amine. The peak at 25.9 ppm is also attributed to the methylene carbon of the aliphatic chain. The $^{13}$C-NMR spectrum of SMI-tC can thus confirm the successful imidization of SMA with 3-(*N,N*-dimethylamino)-1-propylamine.

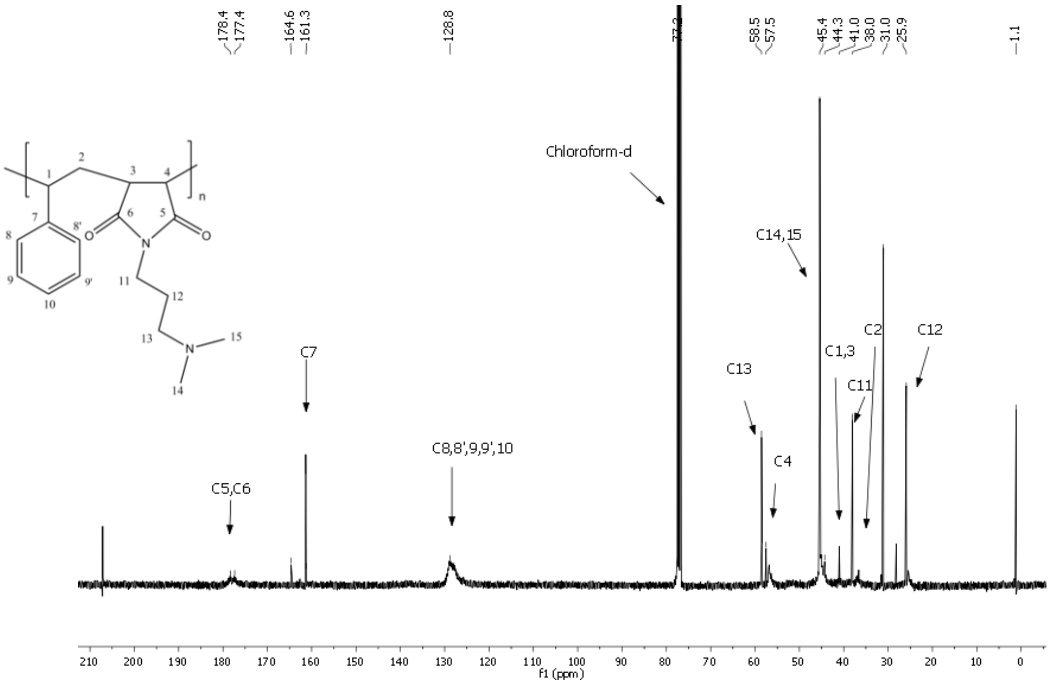


Figure 3.16: $^{13}$C-NMR of SMI-tC in d-chloroform.

### 3.2.5 SMI-qC$_{10}$ and SMI-qC$_{12}$

### a) $^{1}$H-NMR

SMI-tC was quaternized with two aliphatic bromoalkanes, namely 1-bromodecane (Br-C$_{10}$) and 1-bromododecane (Br-C$_{12}$). The $^{1}$H-NMR spectrum of SMI-qC$_{12}$ (Figure 3.17) will be discussed as only the absorption band integration intensity of the peak at 1.22 ppm due to the methylene protons of the aliphatic chain differs slightly for SMI-qC$_{10}$ and SMI-qC$_{12}$. A

characteristic shielded, sharp peak at 0.84 ppm can be seen due to the terminal methyl groups of the $C_{12}$ chain. Additionally a sharp signal at 1.22 ppm is attributed to the methylene protons of the aliphatic carbon chain (H-17 to 25). The broad peak at 1.69 ppm can be assigned to the aliphatic methylene protons of the styrene polymer backbone (H-2) the methylene next to the terminal methyl of the $C_{12}$ chain (H-26) and the methylene on the *N*-alkylamine chain (H-12). The characteristic peak at 3.60 ppm can be assigned to the protons adjacent to the quaternary ammonium moiety (H-14,15) which partially overlaps with the band due to the protons on the maleic anhydride polymer backbone (H-3,4) at 3.37 ppm. The electronegative nitrogen and carbonyl groups will thus lead to deshielding and a higher chemical shift. The broad peak at 6.5-7.5 ppm can be attributed to the deshielded aromatic protons. The successful quaternization of SMI-tC using 1-bromododecane to yield SMI-q$C_{12}$ can thus be confirmed.

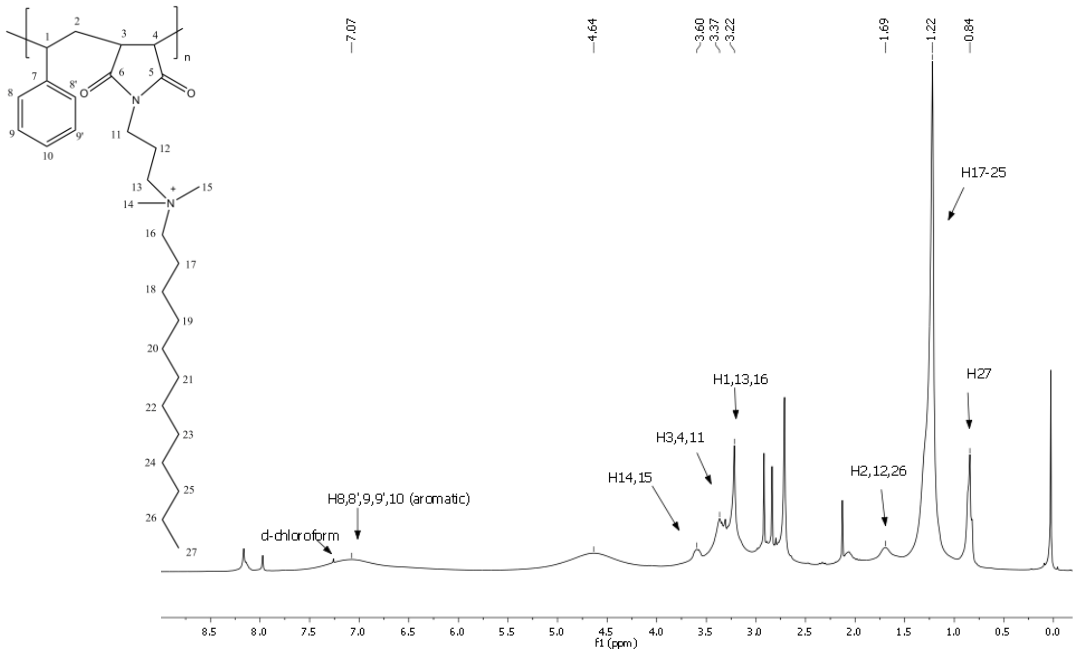


Figure 3.17: $^{1}$H-NMR spectrum of SMI-q$C_{12}$ in d-chloroform.

### b) $^{13}$C-NMR

The $^{13}$C-NMR spectrum of SMI-q$C_{12}$ (Figure 3.18) had similar peaks compared to SMI-tC with additional upfield peaks due to the additional alkyl chain. The methylene carbon signals in the alkyl chain (C18 to 25) are characterized by a peak at 32.0 ppm. Additionally the methyl group (C-27) of the $C_{12}$ chain can be assigned to the upfield peak at 14.2 ppm. The additional upfield peaks thus confirms that nucleophilic substitution took place at the tertiary amine moiety of SMI-tC and that SMI-q$C_{12}$ was obtained.[20]

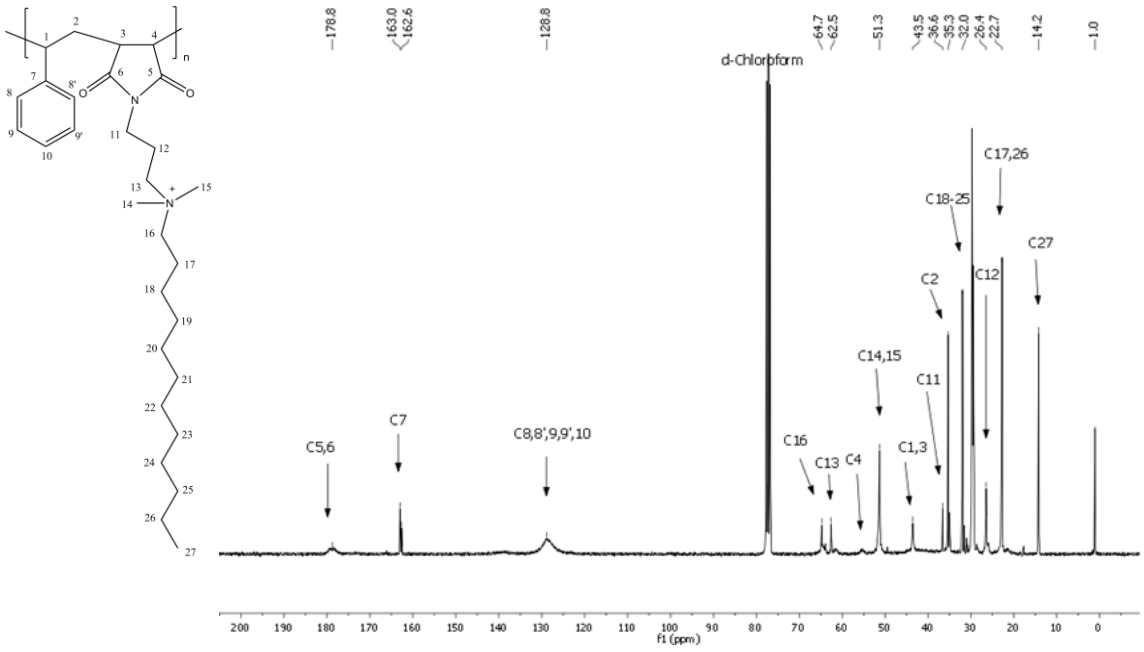


Figure 3.18: $^{13}$C-NMR spectrum of SMI-qC$_{12}$ in d-chloroform.

## 3.3 Conclusion

Pristine chitosan was modified via *N*-substitution and quaternized, forming CS-qC$_{10}$ and CS-qC$_{12}$. Chitosan was modified with linker molecules in order to immobilize Con A, CS-EDC was thus synthesized. SMA was synthesized, modified to form SMI-tC and quaternized to form SMI-qC$_{10}$ and SMI-qC$_{12}$. The synthesis of the polymers were confirmed via ATR-FTIR, $^{1}$H-NMR and $^{13}$C-NMR spectroscopy. The chemical structures of the polymers were chosen based on possible *Mtb* capturing capabilities and will subsequently be used as affinity substrates in the form of nanofibers and nanoparticles.

## 3.4 Experimental

### 3.4.1 Materials

Chitosan (Sigma-Aldrich, Mw = 129 000, DDA 75) was used for the synthesis of *N*,*N*-(2-dimethyl)propyl-3-*N',N'*-dimethyl-*N'*-decylammonium chitosan chloride (CS-qC$_{10}$), *N*,*N*-(2-dimethyl)propyl-3-*N',N'*-dimethyl-*N'* dodecylammonium chitosan chloride (CS-qC$_{12}$) and CS-EDC. While styrene monomer (Merck, ≥ 99%) and maleic anhydride (Merck, 99%) was used for the synthesis of SMA as well as SMI-qC$_{10}$ and SMI-qC$_{12}$. The following chemicals were also utilized: isobutyraldehyde (Aldrich, 98%), formaldehyde solution (Merck, min 37%), dimethylamine solution (Riedel-de Haën, ca. 40%), acetic acid (Merck, ≥ 97.7%), NaBH$_4$ (Aldrich, 99%), acetone (Sigma-Aldrich, 99.5%), *N*-methyl-2-pyrrolidinone (Sigma-Aldrich, ≥

99%), 1-bromodecane (Aldrich, 98%), 1-bromododecane (Aldrich, 97%), glutaraldehyde solution (Sigma-Aldrich, 50 wt% in $H_20$), ethanol (Sigma-Aldrich, 99.5%), epichlorohydrin (Aldrich, 99%), glycine (Saarchem, 99%), 1,4-dioxane (Sigma-Aldrich, ≥ 99%), sodium hydroxide pellets (Merck, ≥ 97%), *N*-(3-dimethylaminopropyl)-*N′*-ethylcarbodiimide hydrochloride (EDC) (Sigma-Aldrich, ≥ 99%), 2,2'-azobis(2-methylpropionitrile) (AIBN) (Sigma-Aldrich, 98%, recrystallized from methanol), ethyl methyl ketone (MEK) (Merck, ≥ 99.5%), heptane (Sigma-Aldrich, 99%), isopropanol (Sigma-Aldrich, 99.5%), pentane (Sigma-Aldrich, 99.5%), *N*,*N*-dimethylformamide (DMF) (Associated chemical enterprises**,** 99%), 3-(*N*,*N*-dimethylamino)-1-propylamine (Aldrich, 99%), diethyl ether (Sigma-Aldrich, 99.5%), deuterium oxide (Merck, 99.96 atom % D), deuterated acetic acid-d4 (Sigma, ≥ 99.5 atom % D), deuterated acetone-d6 (Merck, 99.9 atom % D) and deuterated chloroform-d1 (Merck, 99.8 atom % D).

### 3.4.2 Characterization techniques

#### a) Attenuated total reflectance Fourier transform infrared spectroscopy (ATR-FTIR)

Infrared spectra were obtained using a Nicolet FTIR spectrometer from Thermo-Fischer. An ATR accessory with a diamond/ZnSe internal reflection crystal was attached. The spectra were recorded from 4000 $cm^{-1}$ to 500 $cm^{-1}$ with a spectral resolution of 4 $cm^{-1}$. 64 individual scans were taken to generate the spectra as well as 32 scans for the background spectra before each sample. Omnic software, version 8.1, was used for data acquisition and processing.

#### b) Nuclear magnetic resonance (NMR) spectroscopy

$^{1}H$ NMR and $^{13}C$ NMR spectra were obtained using a Varian VXR 400 or 600 MHz instrument equipped with a Varian magnet (7.0 T). The pristine chitosan and modified chitosan polymers were dissolved in deuterium oxide ($D_2O$) and deuterated acetic acid (d4-acetic acid) in a 70:30 (v/v). The SMA derivatives were dissolved in deuterated chloroform ($CDCl_3$) or deuterated acetone (d6-Acetone) depending on the solubility. CP-MAS $^{13}C$ and SP-MAS $^{13}C$ NMR was performed on chitosan and CS-EDC. The solid state NMR experiments were performed on a Varian VNMRS instrument operating at a frequency of 126 MHz using the combined techniques of magic angle spinning (MAS) and cross-polarization (CP) as well as magic angle spinning (MAS) combined with single pulse (SP). A 4mm Vespel HX T3 MAS probe was used with 5 kHz MAS rate spinning. Analysis was performed at 25 ˚C.

### 3.4.3 Experimental

#### a) 3-dimethylamino-2,2-dimethylpropanal

An aldehyde, as illustrated in Scheme 3.1, was synthesized as modification agent in order to modify pristine chitosan, forming *N*-substituted chitosan. The synthesis is based on the patent by Bernhagen, et al.[21]

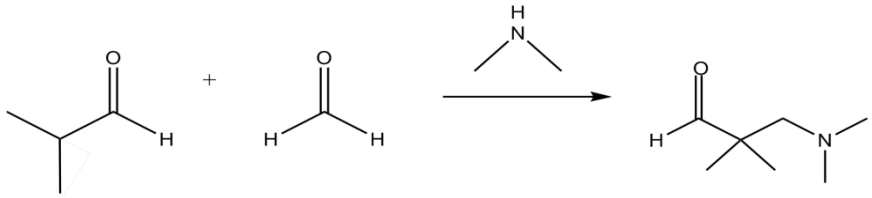


Scheme 3.1: Synthesis of 3-dimethylamino-2,2-dimetylpropanal.

Isobutyraldehyde (50.40 g, 0.7 mole) and aqueous 37% formaldehyde solution (56.7 g, 0.7 mole) was placed in a three neck round bottom flask. 40 % dimethylamine solution (78.75 g, 0.7 mole) was added. The reaction (pH 11) was heated to 100 ˚C and purged with $N_2$ gas for 5 hours. Thereafter the nitrogen gas was removed and the reaction refluxed for a further 24 hours. The reaction was cooled and separated via a separating funnel. The organic phase (bottom layer) was placed in a rotary evaporator to remove the aqueous phase. An orange liquid product was obtained. $^{1}$H NMR (600 MHz, $D_2O$) $\delta$ (ppm) 9.51 (s, 1H, H-1), 2.74 (s, 2H, H-3), 2.24 (s, 6H, H-4,5), 1.22 (s, 6H, H-6,7). $^{13}$C NMR (600 MHz, $D_2O$) $\delta$ (ppm) 211.3 (C-1), 69.5 (C-2), 68.5 (C-3), 45.6 (C-4,5), 24.6 (C-6,7).

#### b) *N*-substituted chitosan

The produced modification agent can selectively form a Schiff base with the amino groups of chitosan. A reducing agent, $NaBH_4$, can then be added resulting in *N*-substituted chitosan. The *N*-substituted chitosan was synthesized based on the experimental procedure of Zhanyong Guo *et al*. as illustrated in Scheme 3.2.[9]

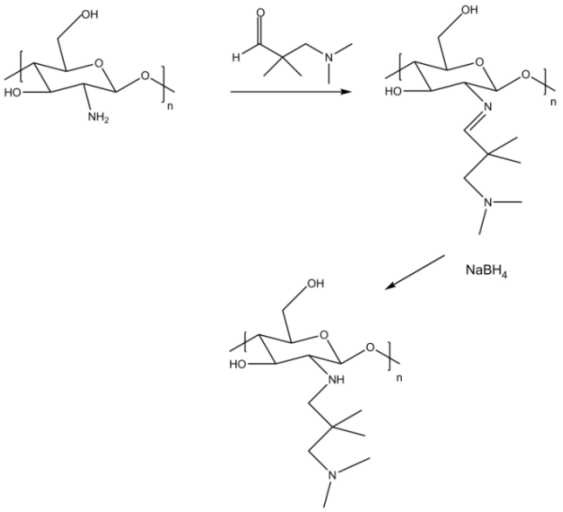


Scheme 3.2: Synthesis of *N*-substituted chitosan.

Chitosan (3 g) was dissolved in 300 mL of 0.5 % acetic acid at room temperature. After which 3-dimethylamino-2,2-dimethylpropanal (6.46 g, 0.05 mol) was added with stirring. After 24 hours 10 % $NaBH_4$ (0.15 mol) was added and the reaction stirred for 24 hours. The white product was precipitated in acetone, filtered and dried at 60 ˚C for 24 hours. Major IR absorptions: 3176, 1638, 1565, 1402, 1352, 992, 945, 809 $cm^{-1}$.$^1$H NMR (400 MHz, $D_2O$/acetic acid-d4 (70:30, v/v)) $\delta$ (ppm) 4.95 (m, H-1), 4.00 (m, H-9), 3.80 (m, H-3, 4, 6), 3.64 (m, H-5,6'), 3.45 (m, H-7), 3.02 (s, H-2), 2.15 (-$^+$N($CH_3$)$_2$), 2.12 (p, H-12,13), 1.22 (s, $H_3$C=O).$^{13}$C NMR (400 MHz, $D_2O$/acetic acid-d4 (70:30, v/v)) $\delta$ (ppm) 99.9 (C-1), 77.8 (C-4), 74.7 (C-5), 73.1 (C-9), 72.8 (C-3), 63.6 (C-6), 59.9 (C-2), 59.3 (-N-**C**$H_3$ x2), 32.9 (C-12,13).

### c) Quaternary chitosan derivatives

The quaternized chitosan derivatives were synthesized via the precursor polymer, *N*-substituted chitosan. *N*-substituted chitosan can react with an alkyl bromine, where the tertiary amine groups of chitosan can attack the electropositive carbon atoms attached to the bromine via nucleophilic substitution. Quaternary chitosan can thus be formed, as illustrated in Scheme 3.3.

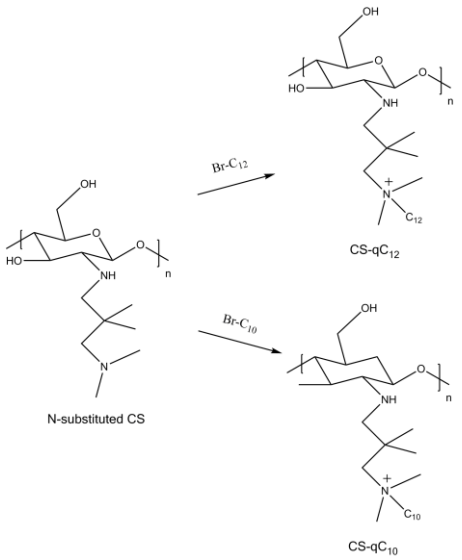


Scheme 3.3: Synthesis of quaternary chitosan via *N*-substituted chitosan.

**i) CS-qC$_{10}$**

*N*-substituted chitosan (3 g) was dispersed in *N*-methyl-2-pyrrolidone (150 mL) and 1.5 mL acetic acid for 24 hours. At this point 1-bromododecane (27 g) was added dropwise, the reaction heated to 100 °C and stirred for 48 hours. The yellow product was precipitated in excess acetone, filtered and dried at 60 ˚C for 24 hours. Major IR absorptions: 3286, 2930, 2875, 1646, 1554, 1408, 1375, 1304, 1150, 1050, 1020 cm$^{-1}$. $^{1}$H NMR (400 MHz, $D_2O$/acetic acid-d4 (70:30, v/v)) $\delta$ (ppm) 5.07 (m, H-1), 4.06 (m, H-9, 10), 3.90 (m, H-3, 4, 6), 3.80 (m, H-5, 6'), 3.57 (t, H-7), 3.36 (m, H-11), 2.92 (s, H-2), 2.16 (-$^{+}$N($CH_3$)$_2$), 1.85 (H-20,21), 1.45 – 1.39 (-$CH_2$-), 1.28 ($H_3$C=O), 0.97 (H-19). $^{13}$C NMR (400 MHz, $D_2O$/acetic acid-d4 (70:30, v/v)) $\delta$ (ppm) 101.0 (C-1), 80.9 (C-4), 78.1 (C-5), 73.5 (C-3), 63.8 (C-6), 59.1 (C-2), 53.3 (-N-**C**$H_3$ x2), 33.8 (C-20,21), 32.5 (-**C**$H_2$-), 25.4 (-**C**$H_3$, Acetyl), 20.3 (C-19).

**ii) CS-qC$_{12}$**

*N*-substituted chitosan (3 g) was dispersed in *N*-methyl-2-pyrrolidone (150 mL) and 1.5 mL acetic acid for 24 hours. At this point 1-bromododecane (27 g) was added dropwise, the reaction heated to 100 °C and stirred for 48 hours. The yellow product was precipitated in excess acetone, filtered and dried at 60 ˚C for 24 hours. Major IR absorptions: 3316, 2923, 2874, 1629, 1510, 1426, 1375, 1305, 1150, 1027, 985 cm$^{-1}$. $^{1}$H NMR (400 MHz, $D_2O$/acetic acid-d4 (70:30, v/v)) $\delta$ (ppm) 5.02 (m, H-1), 3.98 (m, H-9, 10), 3.85 (m, H-3, 4, 6), 3.72 (m, H-5, 6'), 3.47 (t, H-7), 3.29 (m, H-11), 2.82 (s, H-2), 2.21 (-$^{+}$N($CH_3$)$_2$), 2.01 (H-22,23), 1.78 – 1.29 (-$CH_2$-), 1.1 ($H_3$C=O), 0.88 (H-21). $^{13}$C NMR (400 MHz, $D_2O$/acetic acid-d4 (70:30, v/v)) $\delta$ (ppm) 100.5 (C-1), 80.3 (C-4), 77.8 (C-5), 73.1 (C-3), 63.5 (C-6), 59.0 (C-2), 53.1 (-N-**C**$H_3$ x2), 33.7 (C-22,23), 32.2 (-**C**$H_2$-), 25.2 (-**C**$H_3$, Acetyl), 20.0 (C-21).

**d) CS-GLU-GLY-EDC**

The pristine chitosan required modification via linker molecules for Con A immobilization. Chitosan was crosslinked with glutaraldehyde followed by activating with glycine and 1-ethyl-3-(3-dimethylaminopropyl) carbodiimide (EDC) as seen in Scheme 3.4.

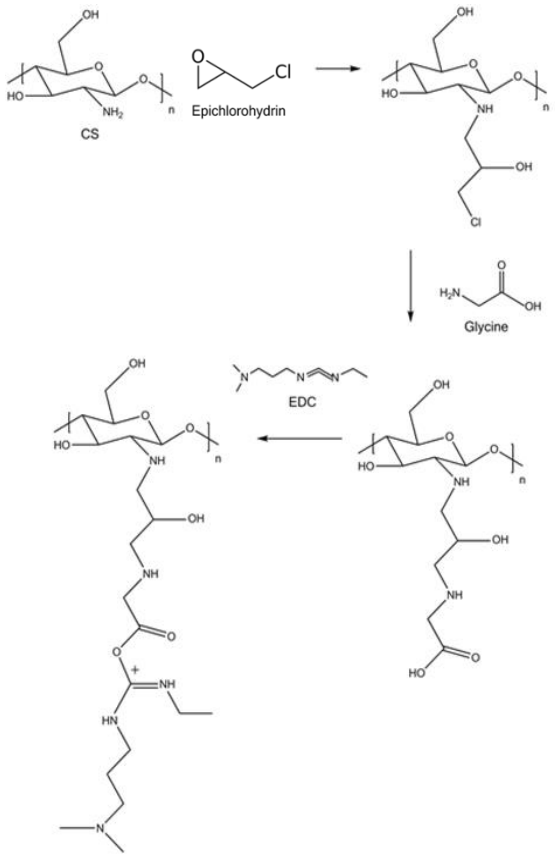


Scheme 3.4: Synthesis of chitosan-EDC via linker molecules.

3 g Chitosan was dissolved in 250 mL of 1% acetic acid. Thereafter 50 mL glutaraldehyde (50 wt%) was added and stirred for 8h. The product was filtered and washed with ethanol and distilled water. The produced crosslinked CS (5 g) was dispersed in 50 mL distilled water, 50 mL ethanol and 10 g epichlorohydrin. The reaction was refluxed for 3h at 100℃, filtered and washed with ethanol and distilled water. The produced CS was added to 5 g glycine dispersed in 100 mL dioxane where after 40 mL of 1M NaOH was added. The reaction was refluxed for 12 hours at 100℃, filtered and washed with water and acetone. The dark brown product was dried in a vacuum oven at r.t. The produced CS-GLU-GLY (1,193 g) was dispersed in 40 mL PBS (pH 7) with stirring. At this point 0,192 g EDC was added and stirred at r.t. for 8 h. The red-brown product was filtered, washed with PBS and dried at r.t. in a vacuum oven. Major IR absorptions: 3266, 2928, 2872, 1628, 1410, 1367, 1320, 1031 $cm^{-1}$. SP-MAS $^{13}C$ NMR (126 MHz) $\delta$ (ppm) 111.5, 101.7 (C1), 75.1 (C-5,3), 61.6

(C-6,2), 32.7-23.7 ($CH_2$,$CH_3$). CP-MAS $^{13}C$ NMR (126 MHz) $\delta$ (ppm) 181.3 (C=O), 144.4 (C=N), 101.7 (C-1), 75.6 (C-5,3), 61.8 (C-6,2), 42.9-23.8 ($CH_2$, $CH_3$).

**e) SMA**

SMA could be synthesized via conventional radical copolymerization using styrene monomer and maleic anhydride monomer with AIBN as initiator, as seen in Scheme 3.5

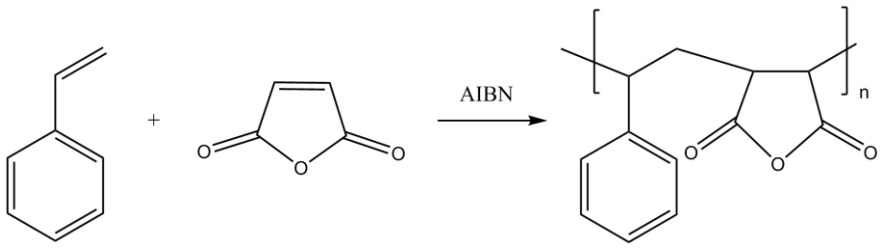


Scheme 3.5: Synthesis of SMA via conventional radical polymerization.

Styrene monomer (15 g, 0.14 mol), maleic anhydride (14 g, 0.14 mol) and 2,2'-azobis(2-methylpropionitrile) (AIBN, 0.1182 g, $7.20\times10^{-4}$ mol) were dissolved in 200 mL methyl ethyl ketone (MEK) at room temperature. The reaction mixture was purged with $N_2$ for 30 min, placed in a heated oil bath at 60 °C for 1 hour and refluxed for 16 hours at 60 °C without $N_2$ gas. The reaction mixture was cooled to room temperature, precipitated in 500 mL isopropanol and washed with heptane. Any unreacted monomer and residual solvent was removed under vacuum at 50 °C overnight. Major IR absorptions: 3027, 1849, 1776, 1710, 1223, 760, 700 $cm^{-1.}$ $^1H$ NMR (600 MHz, acetone): δ (ppm) 7.12 (m, H-8,8',9,9',10 (aromatic)), 3.28 (m, H-3,4), 2.34 (m, H-1,2). $^{13}C$ NMR (600 MHz, acetone): δ (ppm) 173.6 (m, C-5, 6), 137.8 (s, C-7), 128.8 (s, C-8,8',9,9',10 (aromatic)), 52.8 (s, C-4), 43.5 (s, C-1,3) 34.9 (s, C-2).

**f) SMI-tC**

SMA was reacted with a modification agent (3-(*N,N*-dimethylamino)-1-propylamine). The reactive maleic anhydride functional group of SMA could undergo a ring opening reaction with the addition of the modification agent, followed by ring closure at increased temperatures. The resulting product and thus imidization yielded SMI-tC as seen in Scheme 3.6.

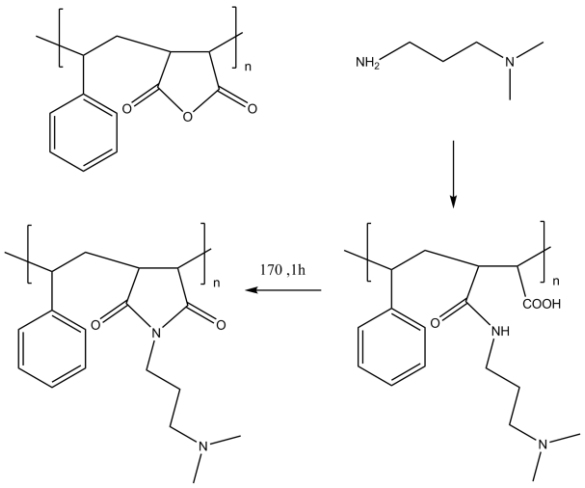


Scheme 3.6: Synthesis of SMI-tC.

SMA (10 g, 49 mmol MAnh) was dissolved in 50 mL DMF at room temperature. 3-(*N,N*-dimethylamino)-1-propylamine (15 g, 147 mmol) was added dropwise to the solution. The reaction was placed in a heated oil bath at 170 °C for two hours, whereafter it was precipitated into diethyl ether, filtered and dried under vacuum at 60 °C overnight. Major IR absorptions: 3444, 2940, 2768, 1768, 1690, 1399, 1344, 1149, 757, 702 $cm^{-1}$. $^{1}H$ NMR (400 MHz, $CDCl_3$): δ (ppm) 7.13 (m, H-8,8',9,9',10 (aromatic)), 3.37 (m, H-3,4), 2.94 (s, H-11), 2.39 (s, H-1), 2.15 (s, H-13,14,15), 1.67 (p, H-2,12).$^{13}C$ NMR (400 MHz, $CDCl_3$): δ (ppm) 178.4 (d, C-5,6), 161.3 (s, C-7), 128.8 (m, C-8,8',9,9',10 (aromatic)), 58.5 (s, C-13), 57.5 (s, C-4), 45.4 (s, C-14,15), 41.0 (s, C-1,3), 38.0 (s, C-11), 36.6 (s, C-2), 25.9 (s, C-12).

### g) Quaternary SMA derivatives

The quaternized SMA derivatives were synthesized via the precursor polymer, SMI-tC. The tertiary amine group of SMI-tC reacted with excess bromoalkane which formed quaternized SMA as seen in Scheme 3.7.

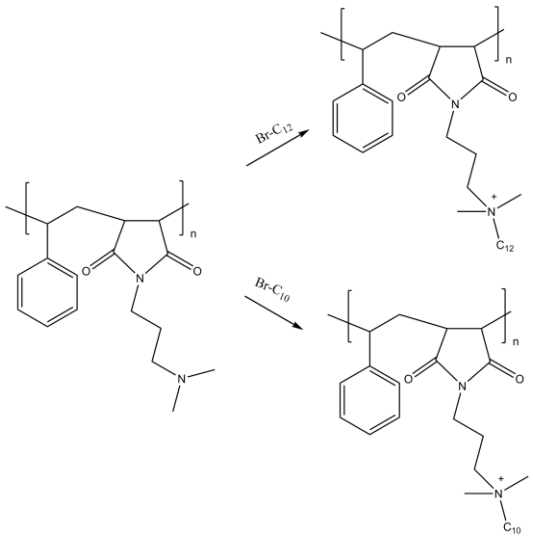


Scheme 3.7: Synthesis of quaternary SMA via SMI-tC.

**i) SMI-qC$_{10}$**

Poly(styrene-[*N*-3-(*N',N'*-dimethylamino)propyl maleimide) (SMI-tC) (3 g, 10,4 mmol MAnh) was dissolved in 50 mL DMF after which 1-bromodecane (2.88 g, 13 mmol) was added dropwise at r.t. The reaction was stirred at 110 °C for 48 hours, cooled, precipitated in diethyl ether, filtered and washed three times with pentane. The SMI-qC$_{10}$ polymer was dried under vacuum at 60 °C overnight to remove residual solvent. Major IR absorptions: 3416, 2922, 2853, 1768, 1662, 1454, 1400, 1350, 1151, 704 cm$^{-1}$. $^{1}$H-NMR (600 MHz, $CDCl_3$): δ (ppm) 7.12 (m, H-8,8',9,9',10 (aromatic) ), 3.46 (m, H-14,15), 3.23 (s, H-3,4,11), 2.92 (s, H-1,13,16), 1.76 (s, H-2,12,24), 1.24 (s, H-17-23), 0.87 (s, H-25). $^{13}$C NMR (600 MHz, $CDCl_3$): δ (ppm) 173.9 (s, C-5,6), 162.8 (s, C-7), 128.0 (s, C-8,8',9,9',10 (aromatic)), 65.3 (s, C-16), 63.2 (s, C-13), 55.6 (s, C-4), 51.3 (s, C-14,15), 43.3 (s, C-1,3), 32.0 (s, C-11), 31.9 (s, C-2), 26.8 (s, C-18-23), 26.4 (s, C-12), 22.8 (s, C-17-23), 14.2 (s, C-25).

**ii) SMI-qC$_{12}$**

Poly(styrene-[*N*-3-(*N',N'*-dimethylamino)propyl maleimide) (SMI-tC) (3 g, 10.4 mmol MAnh) was dissolved in 50 mL DMF after which 1-bromododecane (3.45 g, 13,8 mmol) was added dropwise at r.t. The reaction was stirred at 110 °C for 48 hours, cooled, precipitated in diethyl ether, filtered and washed three times with pentane. The SMI-qC$_{10}$ polymer was dried under vacuum at 60 °C overnight to remove residual solvent. Major IR absorptions: 3401, 2922, 2853, 1768, 1695, 1453, 1401, 1355, 1149, 1024, 757 cm$^{-1}$. $^{1}$H-NMR (300 MHz, $CDCl_3$): δ (ppm) = 7.07 (m, aromatic), 3.60 (s, H-14,15), 3.37 (s, H-3,4,11), 3.22 (s, H-1,13,16), 1.69 (s, H-2,12,26),1.22 (s, H-17-25), 0.84 (s, H-27). $^{13}$C NMR (300 MHz, $CDCl_3$): δ (ppm) 178.8 (s, C-5,6), 163 (s, C-7), 128.8 (s, C-8,8',9,9',10 (aromatic)), 64.7 (s, C-16), 62.5

(s, C-13), 55.3 (s, C-4), 51.3 (s, C-14,15), 43.5 (s, C-1,3), 36.6 (s, C-11), 35.3 (s, C-2), 32.0 (C-18-25), 26.4 (s, C-12), 22.7 (s, C-17,26), 14.2 (s, C-27).

## 3.5 References

1. Homayoni, H., Ravandi, S. A. H. & Valizadeh, M. Electrospinning of chitosan nanofibers: Processing optimization. *Carbohydr. Polym.* **77,** 656–661 (2009).
2. Guo, Z., Liu, H., Chen, X., Ji, X. & Li, P. Hydroxyl radicals scavenging activity of *N*-substituted chitosan and quaternized chitosan. *Bioorganic Med. Chem. Lett.* **16,** 6348–6350 (2006).
3. Sahariah, P., Benediktssdóttir, B. E., Hjálmarsdóttir, M. Á., Sigurjonsson, O. E., Sørensen, K. K., Thygesen, M. B., Jensen, K. J. & Másson, M. Impact of chain length on antibacterial activity and hemocompatibility of quaternary *N*-alkyl and *N*, *N*-dialkyl chitosan derivatives. *Biomacromolecules* **16,** 1449–1460 (2015).
4. Kim, C. H., Choi, J. W., Chun, H. J. & Choi, K. S. Synthesis of chitosan derivatives with quaternary ammonium salt and their antibacterial activity. *Polym. Bull.* **38,** 387–393 (1997).
5. Cronje, L., Warren, R. & Klumperman, B. pH-dependent adhesion of mycobacteria to surface-modified polymer nanofibers. *J. Mater. Chem. B* **1,** 6608–6618 (2013).
6. Schoukens, G., Martins, J. & Samyn, P. Insights in the molecular structure of low- and high-molecular weight poly(styrene-maleic anhydride) from vibrational and resonance spectroscopy. *Polym. (United Kingdom)* **54,** 349–362 (2013).
7. Cloete, W. J., Verwey, L. & Klumperman, B. Permanently antimicrobial waterborne coatings based on the dual role of modified poly(styrene-*co*-maleic anhydride). *Eur. Polym. J.* **49,** 1080–1088 (2013).
8. Kalkan, N. A., Aksoy, S., Aksoy, E. A. & Hasirci, N. Preparation of Chitosan-Coated Magnetite Nanoparticles and Application for Immobilization of Laccase. *J. Appl. Polym. Sci.* **123,** 707–716 (2012).
9. Guo, Z., Xing, R., Liu, S., Zhong, Z., Ji, X., Wang, L. & Li, P. Antifungal properties of Schiff bases of chitosan, *N*-substituted chitosan and quaternized chitosan. *Carbohydr. Res.* **342,** 1329–1332 (2007).
10. Sajomsang, W., Gonil, P. & Tantayanon, S. Antibacterial activity of quaternary ammonium chitosan containing mono or disaccharide moieties: Preparation and characterization. *Int. J. Biol. Macromol.* **44,** 419–427 (2009).
11. Al-Wakeel, K. Z., Abd El Monem, H. & Khalil, M. M. H. Removal of divalent manganese from aqueous solution using glycine modified chitosan resin. *J. Environ. Chem. Eng.* **3,** 179–186 (2015).
12. Kavaz, D., Odabaş, S., Güven, E., Demirbilek, M. & Denkbaş, E. B. Bleomycin Loaded Magnetic Chitosan Nanoparticles as Multifunctional Nanocarriers. *J. Bioact. Compat. Polym.* **25,** 305–318 (2010).
13. Long, J., Li, X., Wu, Z., Xu, E., Xu, X., Jin, Z. & Jiao, A. Immobilization of pullulanase onto activated magnetic chitosan/$Fe_3O_4$ nanoparticles prepared by in situ mineralization and effect of surface functional groups on the stability. *Colloids Surfaces A Physicochem. Eng. Asp.* **472,** 69–77 (2015).
14. Heux, L., Brugnerotto, J., Desbrières, J., Versali, M. F. & Rinaudo, M. Solid state NMR for determination of degree of acetylation of chitin and chitosan. *Biomacromolecules* **1,** 746–751 (2000).
15. Udoetok, I. A., Wilson, L. D. & Headley, J. V. Self-Assembled and Cross-Linked Animal and Plant-Based Polysaccharides: Chitosan-Cellulose Composites and Their Anion Uptake Properties. *ACS Appl. Mater. Interfaces* **8,** 33197–33209 (2016).
16. Derenne, S., Coelho, C., Anquetil, C., Szopa, C., Rahman, A. S., McMillan, P. F., Corà, F., Pickard, C. J., Quirico, E. & Bonhomme, C. New insights into the structure and chemistry of

Titan's tholins via $^{13}C$ and $^{15}N$ solid state nuclear magnetic resonance spectroscopy. *Icarus* **221,** 844–853 (2012).

17. Ali, E.A., Elkholy, S. S., Morsi, R. E. & Elsabee, M. Z. Studies on adsorption behavior of Cu (II) and Cd (II) onto aminothiophene derivatives of Styrene Maleic anhydride copolymer. *J. Taiwan Inst. Chem. Eng.* **64,** 325–335 (2015).

18. Moraes, L. G. P., Rocha, R. S. F., Menegazzo, L. M., Araújo, E. B., Yukimito, K. & Moraes, J. C. S. Infrared spectroscopy: a tool for determination of the degree of conversion in dental composites. *J. Appl. Oral Sci.* **16,** 145–149 (2008).

19. Xiang, T., Tang, M., Liu, Y., Li, H., Li, L., Cao, W., Sun, S. & Zhao, C. Preparation and characterization of modified polyethersulfone hollow fiber membranes by blending poly (styrene-*alt*-maleic anhydride). *Desalination* **295,** 26–34 (2012).

20. Pavia, D. L., Lampman, G. M. & Kriz, G. S. *Introduction to Spectroscopy fourth edition*. *Thomson Learning, Inc.* (2009).

21. Bernhagen, W., Falk, V., Springer, H., Weber, J., Wiebus, E. & Kniep, C. Process for preparing 3-dimethylamino-2,2-dimethylpropanal. (1985).

# Chapter 4

## Chitosan based bi-component nanofibers and SMA based nanofibers

## 4.1 Introduction

Electrospinning is a favourable method for producing continuous polymer fibers with diameters in the nano-scale range. Fibers generated by conventional methods such as spinning from melt or solution are in the 5-500 µm range and thus not favourable for biological applications where a high surface area is needed. During electrospinning, an external electric field is imposed on the polymer solution or melt, the solution and spinning conditions will thus greatly affect fiber formation. The diameters and morphology of the nanofibers will depend on parameters such as the polymer type, polymer chain conformation, viscosity and concentration of solution, conductivity, polarity and surface tension of the solvent. Spinning conditions such as applied field strength, distance between needle tip and collector plate and the feeding rate also need to be optimized for efficient fiber formation.

Electrospinning continuous fibers of polyelectrolyte polymers (such as chitosan) via aqueous solutions have previously been considered impossible due to the repulsive forces between the ionogenic groups as well as their ability to form specific intra- and intermolecular interactions. In recent years, nanofibers could, however, be electrospun from ionogenic polymers by utilizing mixed solutions of ionogenic polymer and non-ionogenic polymer.[1,2] Blending with non-ionogenic polymers improves the electrospinnability as well as the physical and mechanical properties of the chitosan/bi-component nanofiber mats. Suitable non-ionogenic partners for electrospinning of chitosan include polylactide (PLA), poly(vinyl alcohol) (PVA), poly(vinyl pyrrolidone) (PVP), poly(ethylene oxide) (PEO)[3] and polycaprolactam (Nylon 6)[4] as seen in Figure 4.1.

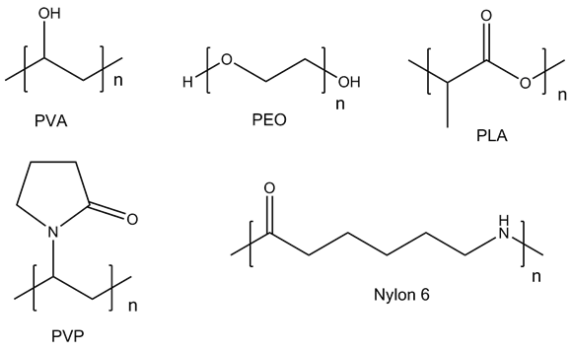


Figure 4.1: Chemical structures of the relevant non-ionogenic polymers.

The different non-ionogenic polymers were blended with the chitosan derivatives (CS-EDC, CS-q$C_{10}$ and CS-q$C_{12}$) followed by electrospinning into bi-component nanofibers in order to determine which modified chitosan and bi-component combination captures *Mtb* most efficiently.

SMA is an ideal *Mtb* capturing platform due to its high heat resistance, dimensional stability, thermoplasticity and low toxicity. The reactive maleic anhydride groups enables polymer modification, SMI-q$C_{10}$ and SMI-q$C_{12}$ were thus synthesized. The maleic anhydride of SMA can also undergo surface functionalization post-electrospinning, such as Con A immobilization.[5] SMA and the quaternized SMA derivatives were electrospun by dissolving the polymers in suitable organic solvents.

Chitosan was modified via linker molecules which activated the polymer for surface functionalization with Con A post-electrospinning. Con A was chosen as surface functionalization agent due to its ability to bind to mannose on the *Mtb* cellular wall.[6] Nanofibers of the SMA derivatives and chitosan derivatives were produced to determine which polymer and functional moiety combination captures *Mtb* most efficiently.

### 4.1.1 Non-ionogenic polymers

#### a) Polyvinyl alcohol

PVA has many important applications, for example, drug delivery, membrane preparation and medical field applications such as artificial pancreas, hemodialysis and implantable medical devices, as it is non-toxic, water soluble and biocompatible. Blending PVA with chitosan can improve the mechanical properties, chemical properties and production cost compared to neat chitosan fibers. Favourable intermolecular interactions can be developed between the different polymers by using different weight ratios of chitosan and PVA.[7] PVA is hydrophilic in nature and the water solubility of PVA based materials must therefore be reduced for use in aqueous media.[8]

#### b) Polylactide

PLA is biodegradable, biocompatible and has a high strength and appropriate degradation rate for musculoskeletal applications. The aliphatic polyester has been applied to biomedical applications such as surgical sutures, substrates for tissue regeneration and carriers for drug and gene delivery.[9] PLA is brittle, has low hydrophilicity, low elongation at break and does not contain reactive side-chain groups. These properties will thus affect the hydrophilicity and brittleness of the chitosan/PLA nanofiber mats.

**c) Polycaprolactam**

Nylon 6 has superior mechanical properties and fiber forming ability compared to other synthetic and natural polymeric materials. Nylon 6 has a high chemical and thermal stability and resembles the collagen protein in its backbone structure and can thus be used in biomedical applications such as bone tissue engineering. Nylon 6 is stable in human bodily fluids, has a hydrophobic surface and tight crystalline structure. The lack of water retention and wettability limits its application in biofilters, biosensors and tissue engineering.[10]

**d) Polyethylene oxide**

PEO is a hydrophilic, biocompatible and water soluble polymer that has frequently been used in biomedical applications.[11,12] The viscosity of neat chitosan in the spinning solution is high due to the strong hydrogen bonding between the $NH_2$ and OH groups of the polymer chains. Blending with PEO in the polymer solution decreases the viscosity of the spinning solution due to the change in intra- and intermolecular interactions of the chitosan chains. The PEO molecules are capable of binding onto the chitosan backbone which increases the solubility of chitosan as well as decreasing the viscosity. Selfassociation of the chitosan chains increased by forming new hydrogen bonds between the OH groups of PEO and water molecules.[13]

**e) Polyvinyl pyrrolidone**

PVP is non-toxic, biocompatible, hydrophilic, has good complexation properties and film forming ability and can thus be used in the biomedical field.[1] The synthetic linear polymer is frequently used in controlled drug release, tissue engineering and wound dressing. It is soluble in water as well as many organic solvents and is thus versatile for electrospinning. Chitosan and PVP are compatible and miscible polymers due to hydrogen bond interactions between the carbonyl groups of PVP and the amino and hydroxyl groups of chitosan. A homogeneous blend can thus be formed for the electrospinning solution.[14]

## 4.2 Results and discussion

The aim of the nanofiber study was to electrospin the quaternized derivatives of chitosan (CS-q$C_{10}$ and CS-q$C_{12}$) and SMA (SMI-q$C_{10}$ and SMI-q$C_{12}$), SMA and CS-EDC into nanofibers via single needle electrospinning. The chitosan derivatives were blended with suitable non-ionogenic polymers. The nanofibers were crosslinked for stability in aqueous media and analysed via SEM (scanning electron microscopy). The SMA and CS-EDC nanofibers were surface functionalized with Con A for *Mtb* affinity. Water contact angle (WCA) measurements were used to determine the hydrophilicity or hydrophobicity of the

nanofibers. The horseradish peroxidase (HRP) enzymatic assay was used to determine the biological activity of the Con A immobilized to the nanofibers.

### 4.2.1 Electrospinning chitosan derivatives/non-ionogenic polymer bi-component nanofibers with crosslinking

The electrospinning and polymer solution parameters greatly affect nanofiber formation. Varying one parameter will affect the other parameters thus optimal spinning conditions must be determined experimentally. The optimal polymer concentration of the chitosan derivatives were 3 wt%. Higher polymer concentrations lead to incomplete dissolution and gelation of the spinning solution. The ideal weight percentages of the non-ionogenic polymers were experimentally determined to be 14 wt% for PVA, 17 wt% for PLA, 25 wt% for Nylon 6, 12 wt% for PEO and 20 wt% for PVP, respectively. A number of parameters determined the optimal spinning solution such as solution viscosity, chain entanglement due to molecular weight and surface tension.

A critical polymer concentration is needed in order to obtain continuous fibers from electrospinning without defects. Sprayed droplets (beading) occurs below this concentration due to insufficient chain entanglements to stabilize the Coulombic repulsion within the ejected polymer solution jet. Uniform and homogenous fibers can be formed when the applied electric field overcomes the surface tension of the polymer solution. The surface tension has an upper and lower boundary if all the other variables are constant. The formation of droplets, beads and fibers can thus be controlled by the surface tension of the polymer solution. Lowering the surface tension of the solution (higher than the critical polymer concentration) aids electrospinning at lower electric fields.[15] Figure 4.2 illustrates the critical polymer concentration.

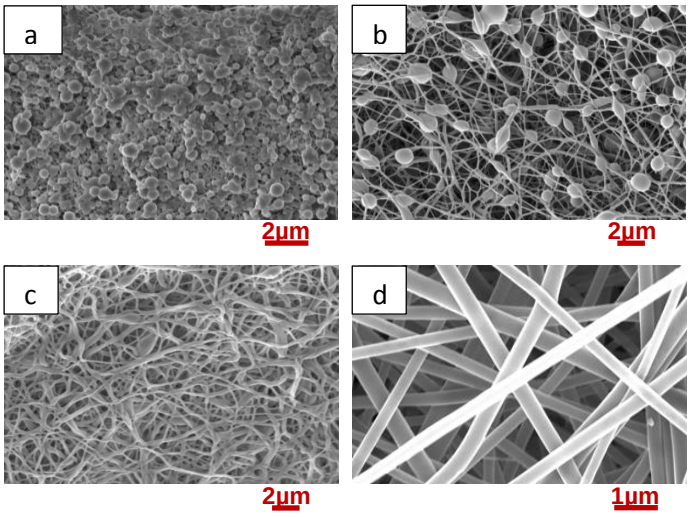


Figure 4.2: SEM images of CS-EDC (3 wt%) blended with PVA a) 10 wt% (Mw=49 kD), b) 10 wt% (Mw=300 kD), c) 12 wt% (Mw=300 kD), d) 14 wt% (Mw=300 kD), in a 40/60 ratio.

PVA as blending polymer was added in a low weight percentage (10 wt%) and molecular weight (Mw=49 kD) (Figure 4.2, a) which resulted in large, irregular electrosprayed droplets due to insufficient chain entanglement and low viscosity. Addition of higher molecular weight bi-component polymer (Mw=300 kD) (b) improved the fiber morphology due to an increase in chain entanglements. Beading is, however, observed at 10 wt% PVA. At 12 wt% PVA (Mw=300 kD) (c) minimal beading was observed due to the increase in viscosity. Finally at 14 wt% PVA (Mw=300 kD) (d) smooth, continuous fibers were electospun and a homogenous fiber mat could be obtained. At a PVA weight percentage higher than 14, the high viscosity spinning solution resulted in polymer jet instability.

The chitosan derivatives and non-ionogenic blending polymers were separately dissolved and blended in a 40/60 ratio (CS/bi-component polymer, w/w). Inclusion of the non-ionogenic polymers facilitated electrospinning and improved mechanical stability. A higher ratio of non-ionogenic polymer is favourable for electrospinning as seen by literature.[15] A 40/60 ratio (CS/bi-component polymer) was thus chosen to facilitate electrospinning while retaining the favourable bacterial adhesion properties of chitosan.

The CS/PVA nanofibers were electrospun by separately dissolving 3 wt% CS in 0.2 M 1,2,3,4-butanetetracarboxylic acid (BA) and 14 wt% PVA in distilled water. Multicarboxylic acids such as BA have been utilized as environment-friendly solvents and *in situ* crosslinking agents for chitosan electrospinning. The acidity of BA can protonate the amine groups of chitosan and dissolve the polymer. Numerous carboxylic acid groups also provide multiple ionic bindings for chitosan thus ionic crosslinked nanofibers can be formed. Multicarboxylic acids are also favourable to maintain chitosan's biocompatibility and non-toxicity.[16] SEM was used to determine the diameter and morphology of the CS/PVA nanofibers as seen in Figure 4.3.

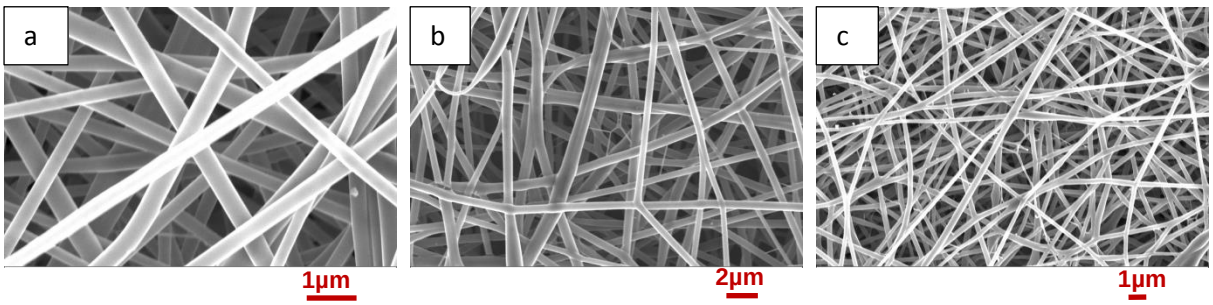


Figure 4.3: SEM images of a) CS-EDC/PVA nanofibers (330 ± 67 nm), b) CS-q$C_{10}$/PVA nanofibers (437 ± 74 nm) and c) CS-q$C_{12}$/PVA nanofibers (264 ± 54 nm).

CS/PLA nanofibers were electrospun by separately dissolving 3 wt% of the chitosan derivatives and 17 wt% of poly(L-lactide) (PLA) in TFA/DCM (trifluoroacetic acid/dichloromethane) (70/30, v/v). PLA has a high strength and was thus a suitable

blending polymer. The produced nanofiber mats were insoluble in phosphate buffered saline (PBS) solution. The nanofibers were, however, brittle and further crosslinking with glutaraldehyde vapour was required for extended exposure to aqueous media. SEM was used to determine the diameter and morphology of the CS/PLA nanofibers as seen in Figure 4.4.

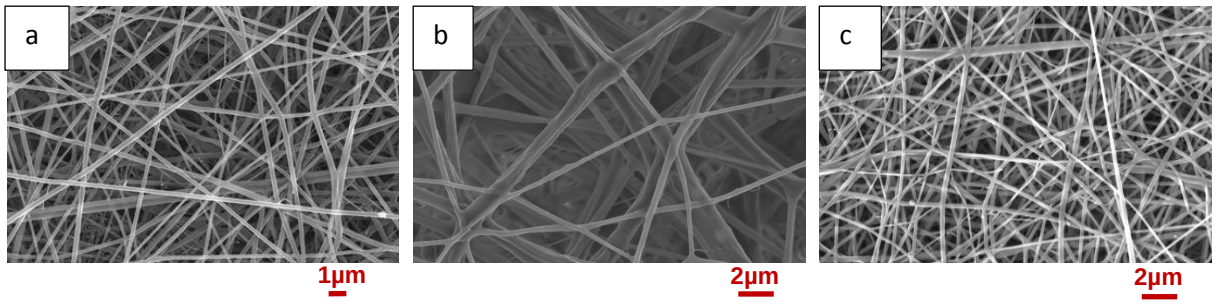


Figure 4.4: SEM images of a) CS-EDC/PLA nanofibers (218 ± 46 nm), b) CS-qC$_{10}$/PLA nanofibers (349 ± 93 nm) and c) CS-qC$_{12}$/PLA nanofibers (202 ± 46 nm).

CS/Nylon 6 nanofibers were electrospun by separately dissolving 3 wt% of the chitosan derivatives and 25 wt% of Nylon 6 in acetic acid/formic acid (2/1, v/v). The CS/Nylon 6 nanofibers were insoluble in aqueous media after stabilizing the nanofiber mats at 100 ˚C for 1h after electrospinning. The nanofiber mats were rinsed with 0.05 M NaOH followed by distilled water to remove acid residues. SEM was used to determine the diameter and morphology of the CS/Nylon 6 nanofibers as seen in Figure 4.5.

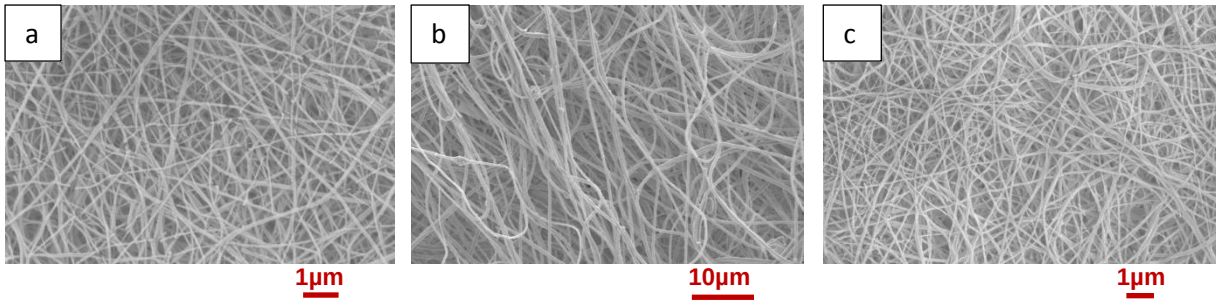


Figure 4.5: SEM images of a) CS-EDC/Nylon 6 nanofibers (111 ± 19 nm), b) CS-qC$_{10}$/Nylon 6 nanofibers (204 ± 41 nm) and c) CS-qC$_{12}$/Nylon 6 nanofibers (141 ± 25 nm).

The CS/PVA, CS/PLA and CS/Nylon 6 nanofibers were stable in PBS and could thus be utilized as affinity substrates as described in Chapter 6. The nanofibers blended with Nylon 6 had the smallest diameters (111-204 nm) and standard deviation of 19-41 nm. The nanofibers blended with PVA and PLA had larger diameters and standard deviations, with 264-437 nm avg. diameter and standard deviation 54-74 nm for PVA and 202-349 nm avg. diameter and standard deviation 46-93 nm for PLA. It was also seen that the CS-qC$_{10}$ fibers had larger diameters than the other CS derivatives when blended with PVA, PLA or Nylon 6.

The CS/PEO nanofibers were electrospun by separately dissolving 3 wt% CS in 10 wt% acetic acid and 12 wt% PEO in distilled water. The CS/PVP nanofibers were electrospun by separately dissolving 3 wt% CS in 10 wt% acetic acid and 20 wt% PVP in distilled water. PVP is hydrophilic and required crosslinking via thermal treatment at 120 ˚C for 3h as soon as possible after electrospinning. The chitosan derivatives are soluble in aqueous media and required crosslinking when blended with hydrophilic bi-component polymers (PVP and PEO). Crosslinking agents were thus used to prevent dissolution and thus impart stability in aqueous media. The crosslinking agents with reactive functional groups are able to covalently bind the polymer chains to each other and retain nanofiber morphology in water. Glutaraldehyde, genipin and photocrosslinking agents were utilized to crosslink the nanofibers and the chemical structures can be seen in Figure 4.6 and 4.7.

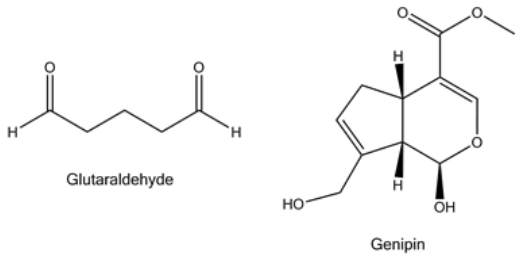


Figure 4.6: Crosslinking agents glutaraldehyde (left) and genipin (right).

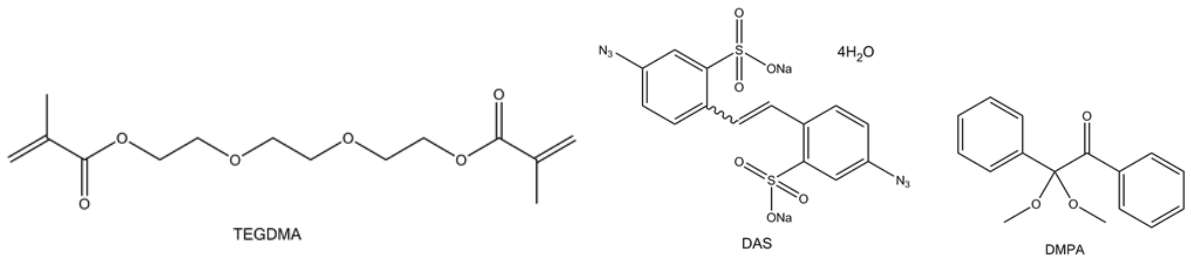


Figure 4.7: Photocrosslinking agents TEGDMA (left), DAS (middle) and DMPA (right).

Glutaraldehyde has been used to covalently crosslink nanofibers for stability in aqueous media. It is, however, known to be cytotoxic.[17] There are discrepancies in literature regarding the crosslinking mechanism of chitosan with glutaraldehyde. The proposed mechanism is where crosslinking proceeds with Schiff base formation between the terminal aldehyde groups of glutaraldehyde and the amino groups of chitosan assuming without formation of Michael-type adducts with the terminal aldehyde group.[9] The CS/PEO and CS/PVP nanofibers were crosslinked by exposing the fiber mats to glutaraldehyde vapour. The nanofibers, however, swelled and dissolved when placed in PBS solution as seen in Figure 4.8 (b) and (d).

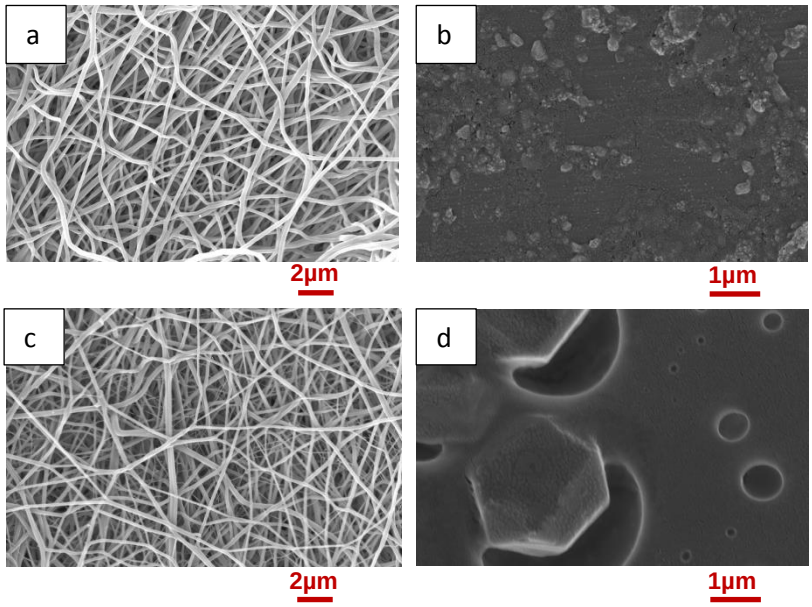


Figure 4.8: SEM images of glutaraldehyde crosslinked nanofibers a) CS-EDC/PEO (161 ± 30 nm), b) EDC/PEO nanofibers after exposed to PBS, c) CS-EDC/PVP nanofibers (167 ± 44 nm) and d) CS-EDC/PVP nanofibers after exposed to PBS.

Genipin was investigated as an alternative natural and lower cytotoxic crosslinking agent. The compound is derived from the fruits of the plant Gardenia jasminoides Ellis and has been used for crosslinking biopolymers of proteins and polysaccharides containing residues with primary amine groups.[18] Similarly to glutaraldehyde crosslinked nanofibers, the CS/PEO and CS/PVP nanofibers *in situ* crosslinked via genipin dissolved in PBS as seen in the case of the CS/PEO nanofibers Figure 4.9 (b).

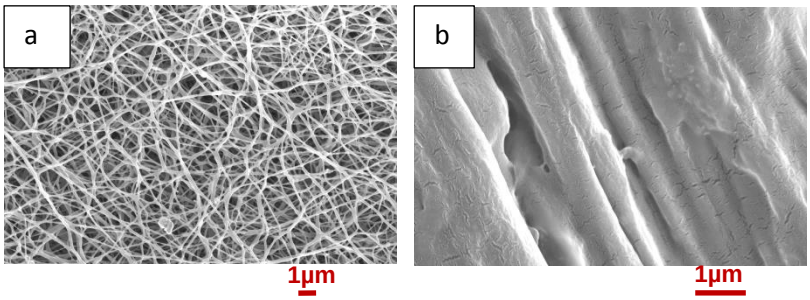


Figure 4.9: SEM images of genipin crosslinked nanofibers a) CS-EDC/PEO (132 ± 35 nm), b) EDC/PEO nanofibers after exposure to PBS.

The CS/PVP nanofibers were crosslinked with photocrosslinking agents by adding 4.5 wt% TEGDMA (triethylene glycol dimethacrylate), 1 wt% DMPA (2,2-dimethoxy-2-phenylacetophenone), 1 wt% DMSO (dimethyl sulfoxide) and 1.5 wt% DAS (4,4'-diazido-2,2'-stilbenedisulfonic acid disodium salt tetrahydrate) (weight % of total polymer content) to the spinning solution. TEGDMA is a crosslinking agent for chitosan with DMPA as photo-initiator whereas DAS is a suitable crosslinking agent for PVP in aqueous solution.[1]

Photocrosslinking, however, formed beaded fibers (a) and a gel network after PBS treatment (b) as seen in Figure 4.10.

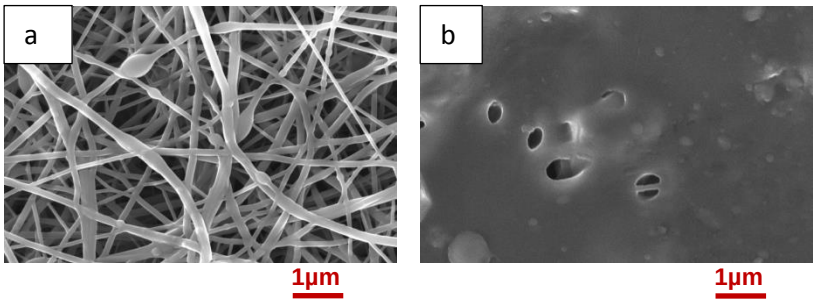


Figure 4.10: SEM images of photocrosslinked PVP nanofibers a) CS-EDC/PVP (145 ± 41 nm), b) EDC/PVP nanofibers after exposure to PBS.

The CS/PEO and CS/PVP nanofibers were inherently hydrophilic due to blending with water soluble PEO and PVP and could not be crosslinked. These fibers were thus removed from the nanofiber study.

### 4.2.2 Electrospinning SMA derivative nanofibers

SMA nanofibers were produced by dissolving 18 wt% polymer in DMF/acetone (1/2, v/v). The SMI-q$C_{10}$ and SMI-q$C_{12}$ nanofibers were dissolved in DMF/methanol (1/1, v/v) with 28 wt% and 25 wt% polymer respectively. The optimal polymer weight percentage was experimentally determined. The nanofiber mats required stabilization at 120˚ C for 2h for optimal dimensional stability. Smooth, continuous and bead free fibers were formed at relatively high polymer weight percentages as seen in Figure 4.11.

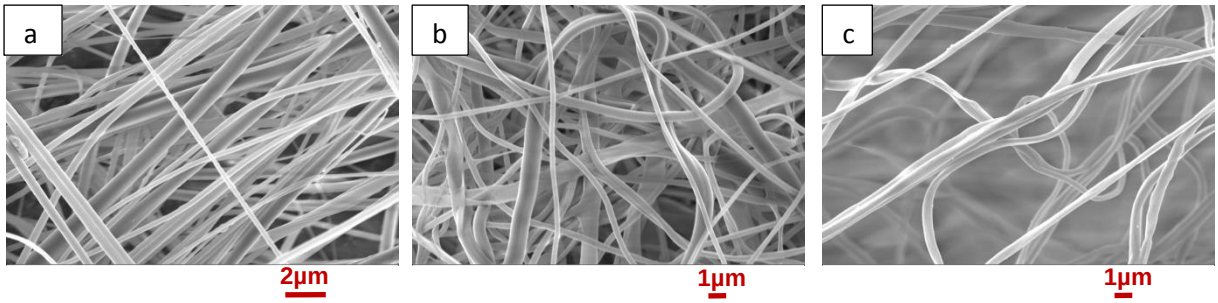


Figure 4.11: SEM images of SMA nanofiber derivatives a) SMA (380 ± 145 nm), b) SMI-q$C_{10}$ (494 ± 143 nm), and c) SMI-q$C_{12}$ (482± 109 nm).

From the SEM images, it was determined that the SMA fibers had the smallest avg. diameter at 380 ± 145 nm. The SMI-q$C_{10}$ and SMI-q$C_{12}$ nanofibers had similar diameters, 494 ± 143 nm and 482 ± 109 nm respectively. These fibers were insoluble in PBS and could thus be utilized as affinity substrates for BCG-mCherry bacteria as described in Chapter 6.

### 4.2.3 Con A immobilization on CS-EDC and SMA nanofibers

Chitosan was crosslinked with glutaraldehyde and modified via linker molecules (glycine and EDC) in order to immobilize Concanavalin A. EDC forms a stable reactive urea derivative (*O*-acylisourea) with the glycine bonded to chitosan. The primary amines of Con A can displace the *O*-acylisourea intermediate via nucleophilic substitution resulting in an amide bond and Con A immobilization as seen in Scheme 4.1.[19]

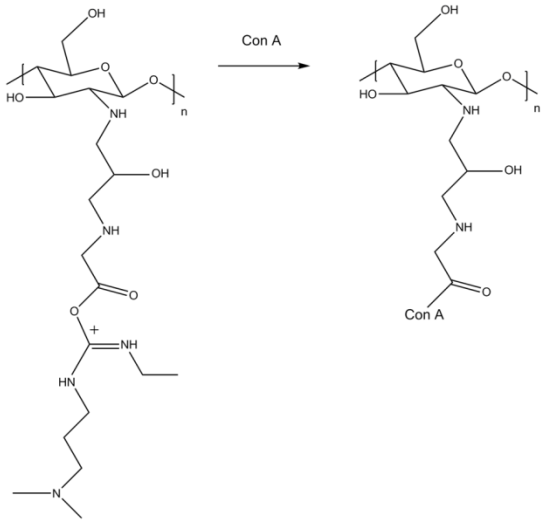


Scheme 4.1: Concanavalin A immobilization to modified chitosan.

Con A was immobilized to the SMA nanofibers via covalent bonding. The nanofibers were surface functionalized with Con A via an imidization reaction. The reactive and easily accessible α-amine groups of Con A can react with the anhydride groups of SMA under neutral conditions resulting in SMI-Con A functionalized nanofiber mats as seen in Scheme 4.2. Manganese and calcium ions were added to the PBS solution to preserve its polypeptide conformation, thus retaining binding activity.[5,20]

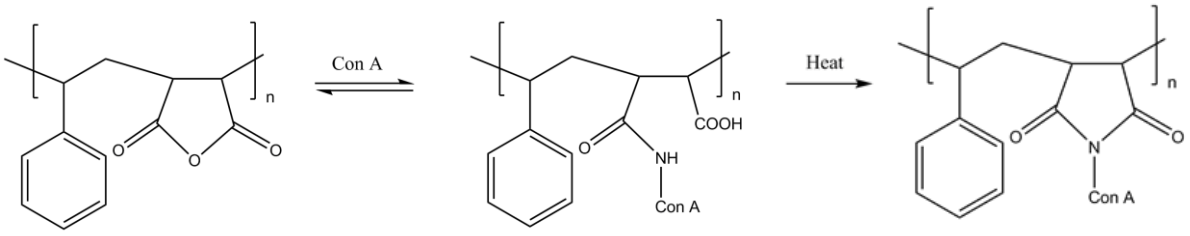


Scheme 4.2: Imidization reaction (immobilization) of SMA with Concanavalin A.

The Con A immobilized nanofibers were analyzed with SEM to determine the change in morphology and fiber diameter. The average fiber diameter of the CS-EDC and SMA fibers did not differ significantly after Con A immobilization. The SMA fibers had a 380 ± 145 nm

avg. diameter compared to 384 ± 182 nm for SMI-Con A while the CS-EDC nanofibers had an avg. diameter of 330 ± 67 nm compared to 281 ± 57 nm for CS-EDC-Con A. Con A formed aggregates attached to the fiber surface as seen in Figure 4.12 (b) and (d).

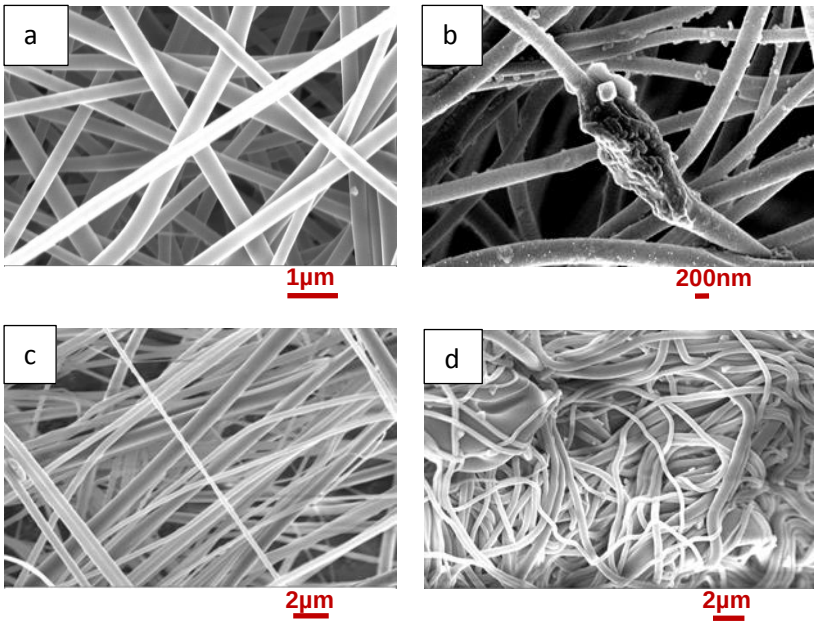


Figure 4.12: SEM images of a) CS-EDC, b) CS-EDC-Con A, c) SMA, d) SMI-Con A nanofibers.

### 4.2.4 Water contact angle measurements

Surface characteristics such as topography, chemistry and surface energy affect the substrate's ability to adsorb or spread water on its surface. The wettability, and thus the ability to spread water over the substrate surface, will consequently affect the interaction and adhesion to cells and bacteria.[21] It has been found that contact angles less than 90˚ correspond to high wettability and a hydrophilic substrate, while contact angles larger than 90˚ correspond to low wettability and thus a hydrophobic surface as illustrated in Figure 4.13.

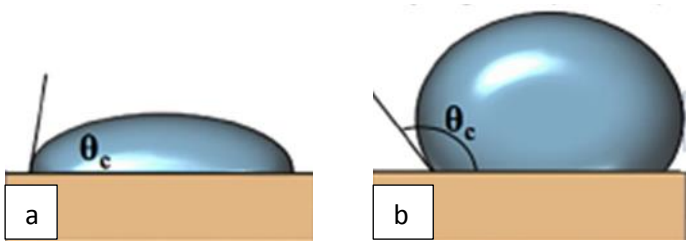


Figure 4.13: Static water contact angle (WCA) measurements with a) θ < 90˚ and b) θ > 90˚.[26]

The chitosan derivatives in the nanofiber study are inherently hydrophilic and water soluble. Blending with hydrophobic PLA and Nylon 6 as well as BA crosslinked PVA improved the

dimensional stability of the nanofiber mats in aqueous solution. Water contact angle (WCA) measurements were thus performed on the CS/PLA, CS/Nylon 6 and CS/PVA nanofibers. All the nanofiber mats were hydrophilic and wetted the surface completely as soon as a 1µL water droplet was placed on the samples. In order to determine the hydrophilicity/hydrophobicity of the various samples, solvent cast films were used for water contact angle measurements. The chitosan derivatives solvent cast films were hydrophilic and the water droplet wetted the surface immediately. Contact angle measurements could, however, be obtained for the PLA, Nylon 6 and PVA films and were 70˚, 73˚ and 74˚ respectively. The hydrophilicity of the non-ionogenic polymer films was thus similar. Blending the chitosan derivatives with the non-ionogenic polymers did not have a significant effect on the WCA measurements, only a slight decrease in hydrophobicity was seen (Figure 4.14 b, d and e). Con A was immobilized on the CS-EDC blended polymer films and a significant increase in hydrophilicity was observed as seen in Figure 4.14 (c) with a water contact angle of 51˚ for CS-EDC/PVA-Con A. The amino acid residues of Con A are able to form hydrogen bonds with the water molecules and will thus improve the wettability of the film.[22]

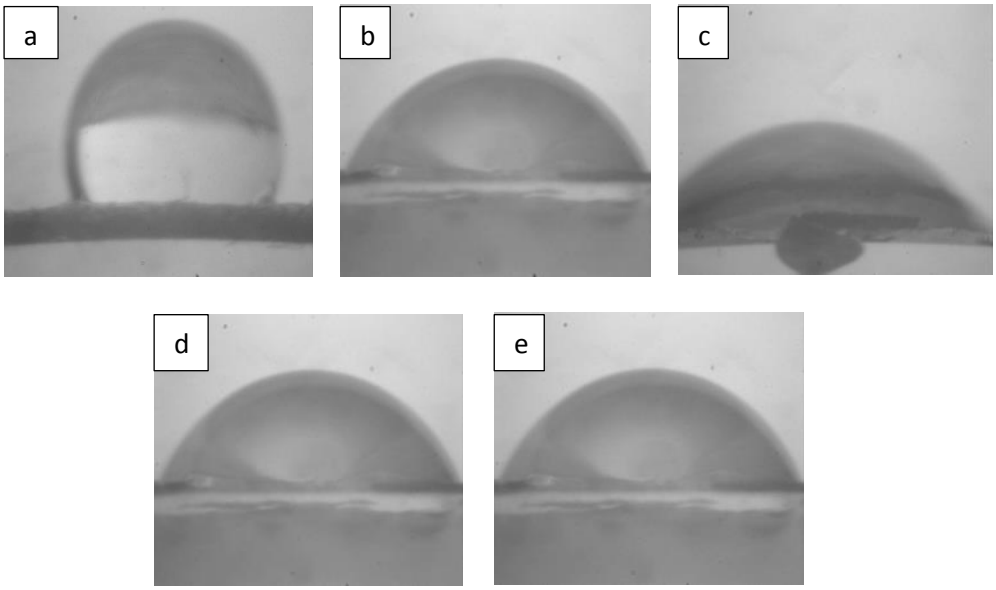


Figure 4.14: Water contact angle measurements of polymer films a) PVA (74˚), b) CS-EDC/PVA (72˚), c) CS-EDC/PVA-Con A (51˚), d) CS-q$C_{10}$/PVA (71˚), e) CS-q$C_{12}$/PVA (72˚).

SMA derivatives are relatively hydrophobic due to the styrene units in the polymer backbone.[23] The SMA derivative nanofibers thus had poor wettability (Figure 4.15 a, c, d). Poor wettability is unfavourable for bacterial adhesion but the fibers had favourable properties such as dimensional stability and minimal swelling in water. The SMI-Con A nanofibers (Fig 4.15 b) had a significant decrease in hydrophobicity due to the ability of Con A to form hydrogen bonds with the water molecules which is favourable for bacterial affinity.

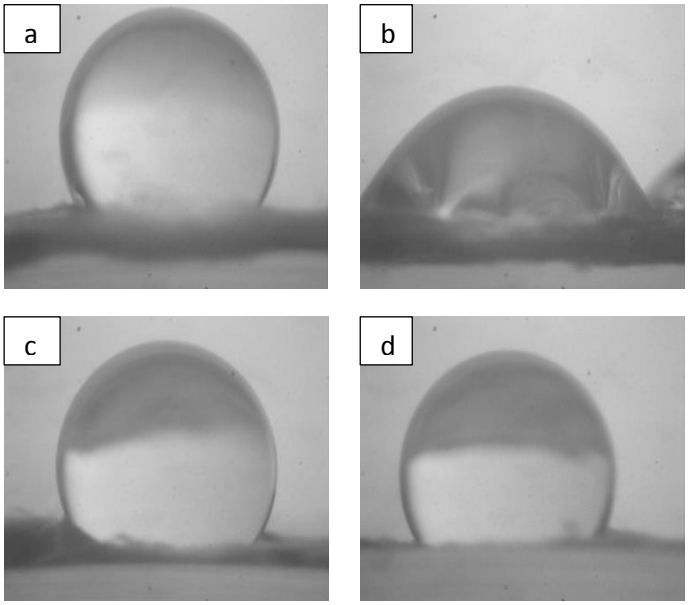


Figure 4.15: Water contact angle measurements of nanofibers a) SMA (136˚), b) SMI-Con A (61˚), c) SMI-q$C_{10}$ (125˚), d) SMI-q$C_{12}$ (134˚).

### 4.2.5 Horseradish peroxidase assay

The horseradish peroxidase (HRP) enzymatic assay was performed on the nanofiber substrates to determine the biological activity of the immobilized Con A. Con A is able to bind to mannose and will therefore bind to the mannose rich glycoprotein (HRP). The HRP bound to the Con A on the fibers can be determined in the presence of a substrate and oxidizing agent.[24] The substrate is oxidized by HRP using an oxidizing agent which can be detected spectrophotometrically. In this HRP assay, the various CS-EDC-Con A and SMI-Con A nanofibers were incubated with HRP in PBS solution for three hours at room temperature, followed by rinsing to remove non-binding HRP. The substrate 2'-azino-bis(3-ethylbenzthiazoline-6-sulfonic acid) (ABTS) and oxidizing agent ($H_2O_2$) was added before measuring the absorbance at 405 nm ($\Delta A_{405nm}$) for 30 minutes. The colour change from green to dark blue was observed for all the fibers, which confirms qualitatively that HRP was bound to biologically active Con A immobilized to the nanofibers (Figure 4.16). The amount of biologically active Con A immobilized to the nanofibers was quantitatively determined as 15.1 % for CS-EDC/PVA-Con A, 11.3 % for CS-EDC/Nylon-Con A and SMI-Con A and 7.5 % for CS-EDC/PLA-Con A. The % biologically active Con A is comparable to literature.[25]

Figure 4.16: SMA-Con A with HRP (left) and without HRP (right).

## 4.3 Conclusion

The chitosan derivative nanofibers were blended with non-ionogenic bi-component polymers in order to improve the stability of the polymer solution jet during electrospinning. The nanofibers will be used as bacterial affinity substrates in aqueous solution and, therefore, required dimensional stability and minimal swelling in water. The CS/PVA crosslinked with BA, CS/PLA crosslinked with glutaraldehyde and CS/Nylon 6 nanofibers retained its stability in aqueous solution and could, therefore, be used as bacterial affinity substrates. The SMA derivatives were electrospun without additional polymers and were stable in PBS after heat treatment. Con A was immobilized via linker molecules to chitosan (CS-EDC) and to SMA. Con A aggregates could be seen on the surface of the nanofibers via SEM. WCA measurements were performed on the chitosan derivative films and SMA derivative nanofibers to determine the hydrophilicity/hydrophobicity. The chitosan derivative films were hydrophilic whereas the SMA nanofibers were relatively hydrophobic which could impede bacterial adhesion. Con A immobilization improved the hydrophilicity of the films and nanofibers due to hydrogen bonding of Con A's amino acid residues with water, which could possibly improve bacterial adhesion. A HRP assay confirmed that the immobilized Con A was biologically active.

## 4.4 Experimental

### 4.4.1 Materials

The following non-ionogenic polymers were used for this part of the project: polyvinyl alcohol (PVA) (Mw = 85-145 kD, 99 % hydrolized), poly(L-lactide) (PLA) (Mw= 259 kD), polycaprolactam (Nylon 6) (density = 1.084 g/mL at 25 °C), polyethylene oxide (PEO) (Mw = 300 kD), polyvinyl pyrrolidone (PVP) (Mw = 360 kD) and were purchased from Sigma Aldrich. The following chemicals were used for this part of the project: 2,2'-azino-bis(3-ethylbenzthiazoline-6-sulfonic acid) (ABTS) (Sigma Aldrich, 10 mg tablets), $KH_2PO_4$ (Aldrich,

99+ %), $H_2O_2$ (Merck, 35 %), bovine serum albumin (Sigma Aldrich, ≥ 96 %), Triton X-100 (Sigma Aldrich, laboratory grade), peroxidase from horseradish Type VI-A (950-2000 unit/mg solid using ABTS), 1,2,3,4-butanetetracarboxylic acid (Aldrich, 99 %), trifluoroacetic acid (Sigma Aldrich, 99 %), DCM (Sigma Aldrich, 99.5%), acetic acid (Merck, ≥ 97.7 %), formic acid (Merck, ≥ 99 %), DMF (Associated chemical enterprises**,** 99%), Acetone (Sigma-Aldrich, 99.5%), Methanol (Sigma Aldrich, 99.5 %), glutaraldehyde (Sigma Aldrich, 50 wt% in $H_2O$), genipin (Sigma-Aldrich, ≥ 98%), TEGDMA (Sigma Aldrich, 95 %), dimethyl sulfoxide (DMSO) (Merck, ≥ 99.9%), 2,2-dimethoxy-2-phenylacetophenone (DMPA)(Aldrich, 99 %), 4,4'-diazido-2,2'-stilbenedisulfonic acid disodium salt tetrahydrate (DAS)(Sigma Aldrich, ≥ 99 %), Concanavalin A from Canavalia ensiformis (Jack bean) Type VI (Sigma Aldrich), $CaCl_2$ (Merck, 98 %), $MnCl_2$ (Sigma Aldrich, beads 99 %), NaCl (Scienceworld, 98.2 %), KCl (Saarchem, 98.5 %), $Na_2HPO_4$ (Nice laboratory chemicals, 99 %).

### 4.4.2 Characterization techniques

#### a) Scanning electron microscopy (SEM)

The micrograph images of the nanofibers were obtained using a MERLIN scanning electron microscope (SEM). The fibers on aluminum foil were cut into approximately 1 ×1 cm squares and placed on the SEM stub via double sided carbon tape. After which the SEM stubs were sputter coated with gold under vacuum prior to imaging. The images were analyzed via *SEM Image Studio*, an imaging analysis program, in order to obtain the fiber diameter and size distributions.

#### b) Water contact angle (WCA)

Static contact angle measurements were used to determine the hydrophobicity or hydrophilicity of the polymer nanofiber surfaces. Magnification could be achieved via a Zeiss microscope unit. For each sample a 1 µL drop of distilled water was placed on the fiber mat followed by capturing the magnified image using a Nikon SMZ-2T (Japan). Static contact angles could be measured using Carl Zeiss AxioVision LE software. In Figure 4.17 the marked parameters needed to calculate the contact angle can be seen on the water droplet, followed by using Equation 4.1 to determine the static contact angle. Ten water droplets of each sample were needed to determine the average water contact angle.

$$\theta = 2 \times \tan^{-1}\left(\frac{h}{r}\right) \qquad 4.1$$

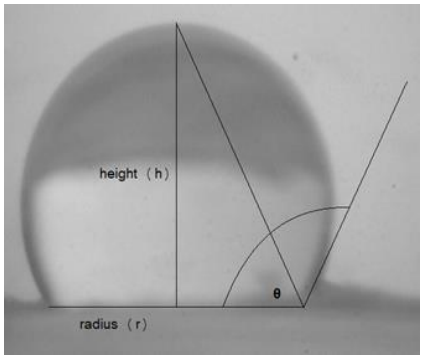


Figure 4.17: Static water contact angle measurements needed to determine the WCA.

### c) Horseradish peroxidase (HRP) enzymatic assay

A HRP assay was used to determine the biological activity of Con A immobilized to the nanofibers. The enzymatic assay of peroxidase (EC (enzyme commission) 1.11.1.7) (Sigma Aldrich) with ABTS as a substrate was used. A 13.6 mg/mL $KH_2PO_4$ solution was prepared with distilled water (pH 5.0 at 25 °C). ABTS (5.0 mg/mL) was added to this solution and referred to as the *substrate*. A 0.3 % (w/w) hydrogen peroxide solution was freshly prepared using a 35 % (w/w) hydrogen peroxide solution and referred to as $H_2O_2$. The *diluent* was prepared in distilled water using 5.4 mg/mL $KH_2PO_4$, 2.5 mg/mL bovine albumin and 5.0 mg/mL Triton X-100 (pH 6.8 at 25 °C). A 1 mg/mL stock solution of peroxidase enzyme from horseradish Type VI-A (HRP) (950-2000 units/mg solid) was prepared using cold diluent and referred to as *enzyme*. The Con A immobilized nanofiber samples (5 mg) were incubated in 1.0 mL of diluted enzyme solution (1 mg/L) for 3 hours on a laboratory shaker at rt. The Con A-HRP fibers were subsequently washed with diluent three times, for 10 min at a time, to remove any non-binding HRP. The reagents were pipetted into cuvettes as summarized in Table 4.1.

Table 4.1: Reagents added to the cuvettes for the blank and sample (test) solution (millilitres).

| | **Blank** | **Sample solution** |
|---|---|---|
| Substrate | 2.9 | 2.9 |
| $H_2O_2$ | 0.1 | 0.1 |
| Diluent | 0.05 | - |
| Enzyme | - | Con A-HRP nanofibers (5 mg) |

The contents of the cuvettes were mixed by inversion followed by determining the increase in absorbance at 405 nm ($A_{405nm}$) for 30 min at 0.02 second intervals with a UV spectrophotometer. The fastest rate was determined by the increase in the slope for each

sample. In Figure 4.18 for the SMI-Con A-HRP nanofibers, the maximum change in absorbance in the 6th minute was used as the maximum linear rate for both the test and the blank sample.

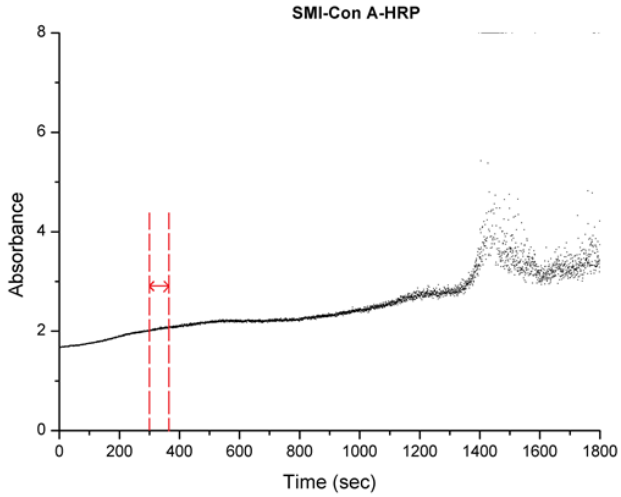


Figure 4.18: Absorbance curve of the HRP incubated SMI-Con A nanofibers.

The biological activity of the Con A immobilized on the nanofiber substrates could be quantified by calculating the units of HRP bound per mass of Con A nanofiber substrate, Equation 4.2.

$$\frac{\text{Units}}{\text{mg solid}} = \frac{\frac{\Delta A_{405nm}}{\text{min}}(\text{sample}) - \frac{\Delta A_{405nm}}{\text{min}}(\text{blank}) \times 3.05 \times \text{DF}}{36.8 \times 0.05} \qquad 4.2$$

3.05 = Final volume in cuvette (millilitres)
DF = Dilution factor of enzyme
36.8 = Millimolar extinction coefficient of oxidised ABTS at $A_{405nm}$
0.05 = Volume enzyme used (millilitres)

From Equation 4.2, it was determined that for the SMI-Con A nanofibers 3 units/mg solid HRP was bound to the fibers. By definition, one unit will oxidise 1.0 µmole ABTS per minute (pH 5.0 at 25°C), therefore, 3 units/mg solid will oxidise 3.0 µmole of ABTS per minute. The final concentration of ABTS in the cuvette was 8.7 mM (26.5 µmole), of which only 3 µmole was oxidised, thus only 11.3 % of the immobilized Con A was biologically active.

### 4.4.3 Experimental procedures

#### a) Electrospinning set-up

The nanofibers were produced via horizontal, single needle electrospinning. The setup includes a high voltage power supply and a syringe pump that is attached to a syringe containing polymer solution. The tip of the needle will be charged and the nanofibers

deposited onto a conductive collection plate. Disposable 5 mL syringes and 0.9 × 40 mm (blunt) steel needle tips were used during electrospinning.

**b) Chitosan bi-component nanofiber preparation**

For the PVA blended nanofibers, a 3 wt% polymer solution of CS-q$C_{10}$, CS-q$C_{12}$ and CS-EDC were prepared by dissolving in 0.2 M 1,2,3,4-butanetetracarboxylic acid. PVA polymer solution (14 wt%) was prepared separately by dissolving in distilled water. For the PLA nanofibers, a 3 wt% polymer solution of CS-q$C_{10}$, CS-q$C_{12}$ and CS-EDC and 17 wt% polymer solution of PLA were separately prepared by dissolving in TFA/DCM (70/30, v/v). In the case of the Nylon 6 nanofibers, a 3 wt% polymer solution of CS-q$C_{10}$, CS-q$C_{12}$ and CS-EDC and 25 wt% polymer solution of Nylon 6 were separately prepared by dissolving in acetic acid/formic acid (2/1, v/v). The Nylon 6 solution was dissolved by heating at 80 ˚C for 8h. For the PEO nanofibers, a 3 wt% polymer solution of CS-q$C_{10}$, CS-q$C_{12}$ and CS-EDC were prepared by dissolving in 10 % acetic acid solution. PEO polymer solution (12 wt%) was prepared separately by dissolving in distilled water. In the case of PVP nanofibers, a 3 wt% polymer solution of CS-q$C_{10}$, CS-q$C_{12}$ and CS-EDC were prepared by dissolving in 10 % acetic acid solution. PVP polymer solution (20 wt%) was prepared separately by dissolving in distilled water.

In all cases, the solutions were stirred at room temperature for 24 h followed by combining the non-ionogenic polymer/CS solutions in a 60/40 ratio (10 g, w/w). The nanofibers were fabricated by electrospinning the respective polymer solutions at a flow rate of 0.013 mL/min, needle tip to collector distance of 20 cm and a voltage of ±15 kV. The nanofibers were collected on a large petri dish covered with aluminium foil. The nanofibers were placed in an oven at 100 ˚C for 1h to thermally crosslink and insure stability. The nanofibers were rinsed with distilled water and dried before use.

**c) SMA and quaternized SMA nanofiber preparation**

A 18 wt% polymer solution of SMA was dissolved in DMF/acetone (1/2, v/v) and stirred for 24h. For the SMI-q$C_{10}$, a 28 wt% polymer solution of SMI-q$C_{10}$ was dissolved in DMF/methanol (1/1, v/v) and stirred for 24h. In the case of SMI-q$C_{12}$, a 25 wt% polymer solution of SMI-q$C_{12}$ was dissolved in DMF/methanol (1/1, v/v) and stirred for 24h. In all cases, the nanofibers were fabricated by electrospinning, the SMA polymer solution at a flow rate of 0.027 mL/min, needle tip to collector distance of 20 cm and a voltage of ±15 kV. The nanofibers were collected on a large petri dish covered with aluminium foil. The nanofibers were placed in an oven at 120 ˚C for 2h to insure stability.

**d) Crosslinking chitosan/ bi-component nanofibers**

**i) Glutaraldehyde vapour crosslinking**

Glutaraldehyde crosslinked nanofibers were obtained by exposing the nanofibers (PEO/CS, PVP/CS and PLA/CS) to 10 mL glutaraldehyde vapour (50 wt%) in a petri dish placed in a desiccator for 24 h. The nanofibers were then dried in a vacuum oven at 30 ˚C for 24 h.

**ii) Genipin crosslinking**

0.5% (w/v) genipin was added to the polymer spinning solutions of PEO/CS and PVP/CS at room temperature with constant stirring, 3 min prior to electrospinning each polymer blend solution. The nanofiber mats were removed from the collector plate and immediately exposed to water vapour in a desiccator at r.t. for 24 h. A petri dish filled with 5 mL distilled water was placed in the desiccator to produce water vapour. The nanofiber mats were washed with ethanol and dried under vacuum at 30 ˚C for 24 h.

**iii) Photocrosslinking**

Photocrosslinked nanofibers were obtained by adding 4.5 wt% TEGDMA, 1 wt% DMPA, 1 wt% DMSO and 1.5 wt% DAS (weight % of total polymer content) to the spinning solution of PEO/CS and PVP/CS. The nanofibers were produced as soon as a homogeneous spinning solution was obtained. To perform crosslinking the nanofiber mats were irradiated with a UV lamp (1500 W, 20 cm away from the nanofiber mats) for 8 h.

**e) Con A immobilization**

A 10 mM phosphate buffered saline (PBS) solution was prepared in distilled water (8 g NaCl, 0.2 g KCl, 1.44 g $Na_2HPO_4$, 0.24 g $KH_2PO_4$, pH 7.4, in 1 L distilled water). 10 mg nanofibers were placed in 1 mL PBS containing Con A (4 mg/mL), $MgCl_2$ (0.01 mg/mL) and $CaCl_2$ (0.01 mg/mL). The samples were incubated on a laboratory shaker at 37 ˚C for 1h, followed by rinsing with PBS (3 times for 10 min at a time) and dried at r.t. in a vacuum oven.

## 4.5 References

1. Ignatova, M., Manolova, N. & Rashkov, I. Novel antibacterial fibers of quaternized chitosan and poly(vinyl pyrrolidone) prepared by electrospinning. *Eur. Polym. J.* **43,** 1112–1122 (2007).
2. Kohsari, I., Shariatinia, Z. & Pourmortazavi, S. M. Antibacterial electrospun chitosan-polyethylene oxide nanocomposite mats containing bioactive silver nanoparticles. *Carbohydr. Polym.* **140,** 287–298 (2016).
3. Maeda, N., Miao, J., Simmons, T. J., Dordick, J. S. & Linhardt, R. J. Composite polysaccharide fibers prepared by electrospinning and coating. *Carbohydr. Polym.* **102,** 950–955 (2014).
4. Maryšková, M., Ardao, I., García-González, C. A., Martinová, L., Rotková, J. & Ševců, A. Polyamide 6/chitosan nanofibers as support for the immobilization of Trametes versicolor

laccase for the elimination of endocrine disrupting chemicals. *Enzyme Microb. Technol.* **89,** 31–38 (2016).

5. Cronje, L., Warren, R. & Klumperman, B. pH-dependent adhesion of mycobacteria to surface-modified polymer nanofibers. *J. Mater. Chem. B* **1,** 6608–6618 (2013).

6. Esparza, M., Palomares, B., García, T., Espinosa, P., Zenteno, E. & Mancilla, R. PstS-1, the 38-kDa *Mycobacterium tuberculosis* glycoprotein, is an adhesin, which binds the macrophage mannose receptor and promotes phagocytosis. *Scand. J. Immunol.* **81,** 46–55 (2015).

7. Rafique, A., Mahmood Zia, K., Zuber, M., Tabasum, S. & Rehman, S. Chitosan functionalized poly(vinyl alcohol) for prospects biomedical and industrial applications: A review. *Int. J. Biol. Macromol.* **87,** 141–154 (2016).

8. Islam, A., Yasin, T., Rafiq, M. A., Shah, T. H., Sabir, A., Khan, S. M. & Jamil, T. In-situ crosslinked nanofiber mats of chitosan/poly(vinyl alcohol) blend: Fabrication, characterization and MTT assay with cancerous bone cells. *Fibers Polym.* **16,** 1853–1860 (2015).

9. Ignatova, M., Manolova, N., Markova, N. & Rashkov, I. Electrospun non-woven nanofibrous hybrid mats based on chitosan and PLA for wound-dressing applications. *Macromol. Biosci.* **9,** 102–111 (2009).

10. Joshi, M. K., Tiwari, A. P., Maharjan, B., Won, K. S., Kim, H. J., Park, C. H. & Kim, C. S. Cellulose reinforced nylon-6 nanofibrous membrane: Fabrication strategies, physicochemical characterizations, wicking properties and biomimetic mineralization. *Carbohydr. Polym.* **147,** 104–113 (2016).

11. Kim, M. W. Surface activity and property of polyethyleneoxide (PEO) in water. *Colloids Surfaces A Physicochem. Eng. Asp.* **128,** 145–154 (1997).

12. Shojaee, S., Cumming, I., Kaialy, W. & Nokhodchi, A. The influence of vitamin E succinate on the stability of polyethylene oxide PEO controlled release matrix tablets. *Colloids Surfaces B Biointerfaces* **111,** 486–492 (2013).

13. Pebdeni, A. B., Sadri, M. & Pebdeni, S. B. Synthesis of chitosan/PEO/silica nanofiber coating for controlled release of cefepime from implants. *RSC Adv.* **6,** 24418–24429 (2016).

14. Poonguzhali, R., Basha, S. K. & Kumari, V. S. Synthesis and characterization of chitosan-PVP-nanocellulose composites for in-vitro wound dressing application. *Int. J. Biol. Macromol.* **105,** 111–120 (2017).

15. Elsabee, M. Z., Naguib, H. F. & Morsi, R. E. Chitosan based nanofibers, review. *Mater. Sci. Eng. C* **32,** 1711–1726 (2012).

16. Pangon, A., Saesoo, S., Saengkrit, N., Ruktanonchai, U. & Intasanta, V. Multicarboxylic acids as environment-friendly solvents and in situ crosslinkers for chitosan/PVA nanofibers with tunable physicochemical properties and biocompatibility. *Carbohydr. Polym.* **138,** 156–165 (2016).

17. Gao, S., Yuan, Z., Guo, W., Chen, M., Liu, S., Xi, T. & Guo, Q. Comparison of glutaraldehyde and carbodiimides to crosslink tissue engineering scaffolds fabricated by decellularized porcine menisci. *Mater. Sci. Eng. C* **71,** 891–900 (2017).

18. Li, Q., Wang, X., Lou, X., Yuan, H., Tu, H., Li, B. & Zhang, Y. Genipin-crosslinked electrospun chitosan nanofibers: Determination of crosslinking conditions and evaluation of cytocompatibility. *Carbohydr. Polym.* **130,** 166–174 (2015).

19. Kavaz, D., Odabaş, S., Güven, E., Demirbilek, M. & Denkbaş, E. B. Bleomycin Loaded Magnetic Chitosan Nanoparticles as Multifunctional Nanocarriers. *J. Bioact. Compat. Polym.* **25,** 305–318 (2010).

20. Hardman, K. D., Agarwal, R. C. & Freiser, M. J. Manganese and calcium binding sites of concanavalin A. *J. Mol. Biol.* **157,** 69–86 (1982).

21. Spriano, S., Chandra, V. S., Cochis, A., Uberti, F., Rimondini, L., Bertone, E., Vitale, A., Scolaro, C., Ferrari, M., Cirisano, F., Gautier, G. & Ferraris, S. How do wettability , zeta potential and hydroxylation degree affect the biological response of biomaterials ? *Mater. Sci. Eng. C* **74,** 542–555 (2017).

22. Li, Z. & Lazaridis, T. The effect of water displacement on binding thermodynamics: Concanavalin A. *J. Phys. Chem. B* **109,** 662–670 (2005).

23. Yao, Q., Lu, S., Lin, F., Zhao, T., Zhao, L. & Chen, X. A co-precipitation strategy for making a ratiometric pH nanosensor for intracellular imaging. *Sensors Actuators B Chem.* **250,** 484–490 (2017).

24. Guo, M., Yang, Y., Wang, Z., Shen, G. & Yu, R. A Mediator-free Horseradish Peroxidase Biosensor Based on Concanavalin A. *Chinese J. Anal. Chem.* **34,** 399–403 (2006).

25. Franco Fraguas, L., Batista-Viera, F. & Carlsson, J. Preparation of high-density Concanavalin A adsorbent and its use for rapid , high-yield purification of peroxidase from horseradish roots. *J. Chromatogr. B* **803,** 237–241 (2004).

26. Zhao, T. & Jiang, L. Contact angle measurement of natural materials. *Colloids Surfaces B Biointerfaces* **161,** 324–330 (2018).

# Chapter 5

Synthesis and characterization of superparamagnetic magnetite nanoparticles and polymer coated nanocomposite materials

## 5.1 Synthesis of pristine and polymer coated magnetic nanoparticles

### 5.1.1 Magnetite nanoparticle formation

Three different approaches can be used to create nanoparticles namely the top-down, bottom-up and virtual approach. The top-down approach has been the traditional approach for miniaturization utilizing lithography. The bottom-up approach entails the self-assembly from molecular precursors in chemical solutions. The virtual approach technique is used by computational theorists where new materials are created in computer simulations.[1] In this study, the bottom-up approach will be followed where dissolved $Fe^{2+}$ and $Fe^{3+}$ ions are co-precipitated from solution to form magnetite ($Fe_3O_4$). Monodisperse iron oxide nanoparticles can be synthesized by controlling the nucleation and crystal growth of the nanoparticles.

With the co-precipitation method, the nuclei can grow uniformly by diffusion from the solution to the nanoparticle surfaces. Monodispersed nanoparticles can be formed by uniform nucleation followed by crystal growth without further nucleation. Crystal growth in solution is interface-controlled up to a certain critical size and beyond that size, the growth is diffusion controlled.[2] Co-precipitation occurs via the LaMer mechanism defined by a short burst of nucleation from a supersaturated solution followed by slow growth of particles without notable additional nucleation as seen in Figure 5.1.[3, 4]

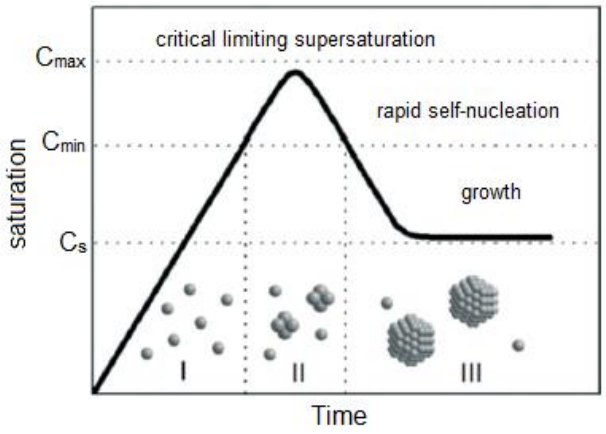


Figure 5.1: The principle of nanoparticle formation due to the LaMer mechanism.

### 5.1.2 Synthesis of pristine $Fe_3O_4$ SPMNs via co-precipitation

Co-precipitation is a simple method and commonly used to synthesize magnetic nanoparticles by titrating aqueous Fe(II)/Fe(III) salt solutions with a base under inert atmosphere. Co-precipitation is favourable due to the large gram-scale product that can be formed. The size, shape, and composition of the magnetic nanoparticles can be controlled by the type of salts used (chlorides, sulfates or nitrates), the Fe(II)/Fe(III) ratio, the reaction temperature, the pH and ionic strength of the solution.[5] $Fe_3O_4$ is thermodynamically stable under ambient laboratory conditions and forms readily under most solvent based nanoparticles synthesis conditions.

The co-precipitation method was first developed by Massart. Fe(III) and Fe(II) was dissolved in an acidified aqueous solution in a 2:1 stoichiometric ratio. After this, a strong base was added which produced a black nanoparticle precipitate. It was noted that the nanoparticles were uniform in diameter and spherical and that oxygen had to be removed from the reaction vessel.[6] The synthesis of iron oxide under ideal conditions as described above, is seen in Reaction 5.1 below.

$$2Fe^{3+} + Fe^{2+} + 8OH^- \rightarrow Fe_3O_4 + 4H_2O \qquad 5.1$$

The nanoparticles are, however, unstable when synthesized at room temperature or in the presence of oxygen. Oxygen may oxidize the nanoparticles to form $Fe(OH)_3$ as seen in Reaction 5.2 or to form maghemite ($\gamma$-$Fe_2O_3$) as seen in Reaction 5.3.[7,8]

$$Fe_3O_4 + \frac{1}{4}O_2 + 4\frac{1}{2}H_2O \rightarrow 3Fe(OH)_3 \qquad 5.2$$

$$2Fe_3O_4 + \frac{1}{2}O_2 \rightarrow 3Fe_2O_3 \qquad 5.3$$

Ideal synthesis conditions have been determined by literature. Bubbling the aqueous solution with $N_2$ gas prevents oxidation and reduces the particle diameter. A pH ≥ 9 is required to precipitate the nanoparticles out of solution, excess base is thus used for precipitation. A stoichiometric ratio ≥ 2:1 for Fe(III):Fe(II) will result in larger, irregular nanoparticles while a ratio ≤ 2:1 results in maghemite, both ratios were thus avoided.[9,10] Fast addition of the base is required during precipitation to reduce agglomeration and to reduce the diameter of the nanoparticles.[11] A higher synthesis temperature was used to impart higher crystallinity and consequently higher saturation magnetization.[12]

### 5.1.3 Synthesis of polymer coated SPMNs

Iron oxide has surface hydroxyl groups that can be used for complex formation with polymer coatings.[13] Polymers such as chitosan have amino, hydroxyl and ether groups that can adhere to the surface of iron oxide nanoparticles via hydrogen bonding. Chitosan coated nanoparticles can be (*in situ*) synthesized via co-precipitation of $Fe^{2+}$, $Fe^{3+}$ and dissolved chitosan. The polymer coating will improve dispersion in solution and thus aggregation.[14] The pristine chitosan forms a shell around the iron oxide core due to polymer chelation. The outer chitosan coating can be functionalized to form CS-EDC as outlined in Chapter 3 as well as Con A immobilized as outlined in Chapter 4.

The iron oxide core can also be surface activated with 3-aminopropyl(triethoxysilane) (3-APTES).[15] The amino groups created on the surface of iron oxide via 3-APTES can be used to coat with SMA. The reactive maleic anhydride of SMA can easily react with amine groups, creating imide bonds, as illustrated by Scheme 5.1.[16] Further functionalization of SMA with 3-(*N*,*N*-dimethylamino)-1-propylamine and 1-bromododecane will result in SMI-q$C_{12}$ coated superparamagnetic magnetite nanoparticles (SPMNs) as outlined in Chapter 3.

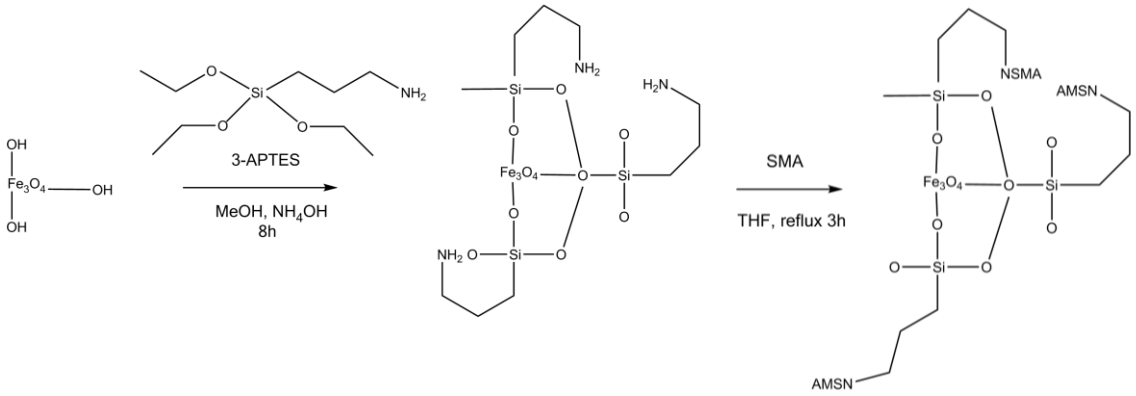


Scheme 5.1: 3-APTES activation of $Fe_3O_4$ nanoparticles and SMA coating.

CS-EDC-Con A and SMI-q$C_{12}$ coated SPMNs were synthesized due to the BCG-mCherry (bacterial affinity) results of the nanofiber study in Chapter 6. Three different polymer loadings were used (0.1 g, 0.5 g and 0.9 g polymer per 1 g iron oxide nanoparticles) to determine the effect of polymer loading.

## 5.2 Results and discussion

The aim of this section of the study was to synthesize and characterize pristine SPMNs as well as the modified chitosan (CS-EDC-Con A) coated SPMNs and SMI-q$C_{12}$ coated

SPMNs. The nanoparticles were characterized via XRD (crystal structure and average crystallite size), TEM (particle diameter and aggregation), TGA (wt% polymer coating), FTIR (functional group analysis), EDX (elemental composition of the nanoparticle surface), HRP (biological activity of Con A) and SQUID (saturation magnetization and superparamagnetism).

### 5.2.1 Powder X-ray diffraction

Pristine $Fe_3O_4$ nanoparticles were synthesized and powder X-ray diffraction (P-XRD) was used to determine the crystallinity and the phase purity of the nanoparticles. Figure 5.2 shows the XRD diffractogram of pristine (uncoated) SPMNs.

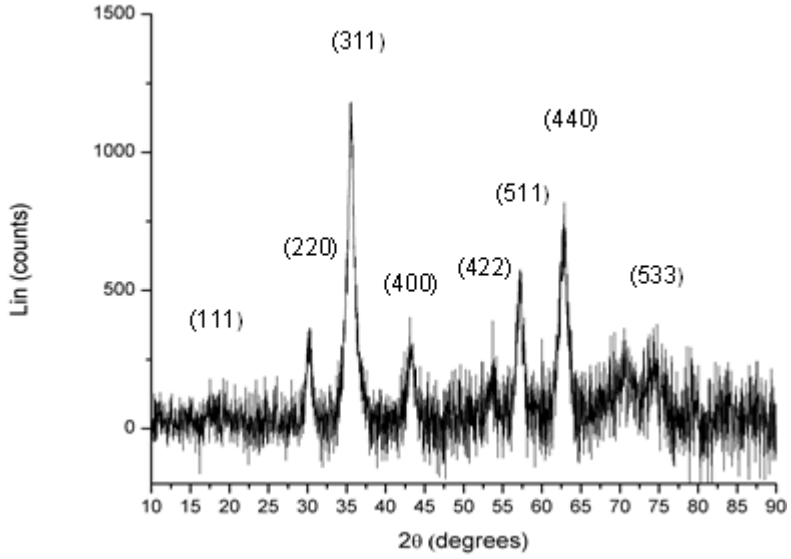


Figure 5.2: X-ray diffractogram pattern of pristine $Fe_3O_4$ nanoparticles.

The XRD diffractogram obtained from pristine $Fe_3O_4$ nanoparticles was compared to literature as well as the database standard for magnetite. It was found that the XRD pattern and relative intensities correlated to literature with characteristic peaks at $2\theta$ = 18.4°, 30.2°, 35.6°, 43.2°, 53.6°, 57.2°, 62.8° and 74.2° corresponding to the (111), (220), (311), (400), (422), (511), (440) and (533) planes respectively.[17] The magnetite nanoparticles thus have a face centred cubic lattice structure as assigned to magnetite by the database standard (Joint Committee on Powder Diffraction Standards, JCPDS file No.00-019-0629).[18]

Peaks of the other phases such as maghemite ($\gamma$-$Fe_2O_3$) are not detected, which is an indication of phase purity. The peaks of maghemite for the (110), (210) and (211) planes are not found in the diffractogram of the iron oxide nanoparticles, as the intensities would be stronger than that of the (111) plane.[19] A peak at 41.2˚ (113) for the oxidized hematite (∝-

$Fe_2O_3$) phase is not seen in the diffractogram. $Fe_3O_4$ (magnetite) is thus the dominant phase for the synthesized nanoparticles. The synthesized magnetite nanoparticles were also black compared to maghemite and hematite nanoparticles which would be brown.[20]

The average crystallite/core size of the pristine $Fe_3O_4$ nanoparticles can be calculated from line broadening analysis using the Scherrer equation (Equation 5.4). The full width at half-maximum (FWHM) of the strongest diffraction peak (311) was used to determine the average core size.[17]

$$D_P = \frac{k\lambda}{\beta\cos\theta} \qquad 5.4$$

Where $D_p$ the average size of the crystalline domains
k is the Scherrer constant (0.89)
λ is the X-ray wavelength (1.5406 nm)
β is the peak full width at half maximum (FWHM),
and θ is the Bragg diffraction angle

The average crystallite size of the pristine $Fe_3O_4$ nanoparticles, using the Scherrer equation, was calculated to be 6.6 nm. The Scherrer formula, however, provides a lower boundary of the average particle size. The average crystallite diameter estimated from XRD is related to the volume weighted average particle size, whereas, the number weighted value is calculated from TEM results. The XRD average particle size measurements also do not include aggregates of nanoparticles or larger nanoparticle clusters.[21]

### 5.2.2 Transmission electron microscopy

Transmission electron microscopy (TEM) (distilled water as solvent) was utilized to determine the effect of polymer loading on the iron oxide nanoparticles with respect to morphology, diameter and size distribution. Uncoated SPMNs were compared to 0.1 g, 0.5 g and 0.9 g polymer loading per 1 g uncoated SPMNs. In Figure 5.3 uncoated SPMNs (a) as well as the three different polymer loadings of CS-EDC-Con A (b-d) and SMI-q$C_{12}$ (e-g) are represented. The polymer coating around the iron oxide core can also be identified in 0.5 g CS-EDC SPMNs (h) and 0.5 g SMI-q$C_{12}$ SPMNs (i).

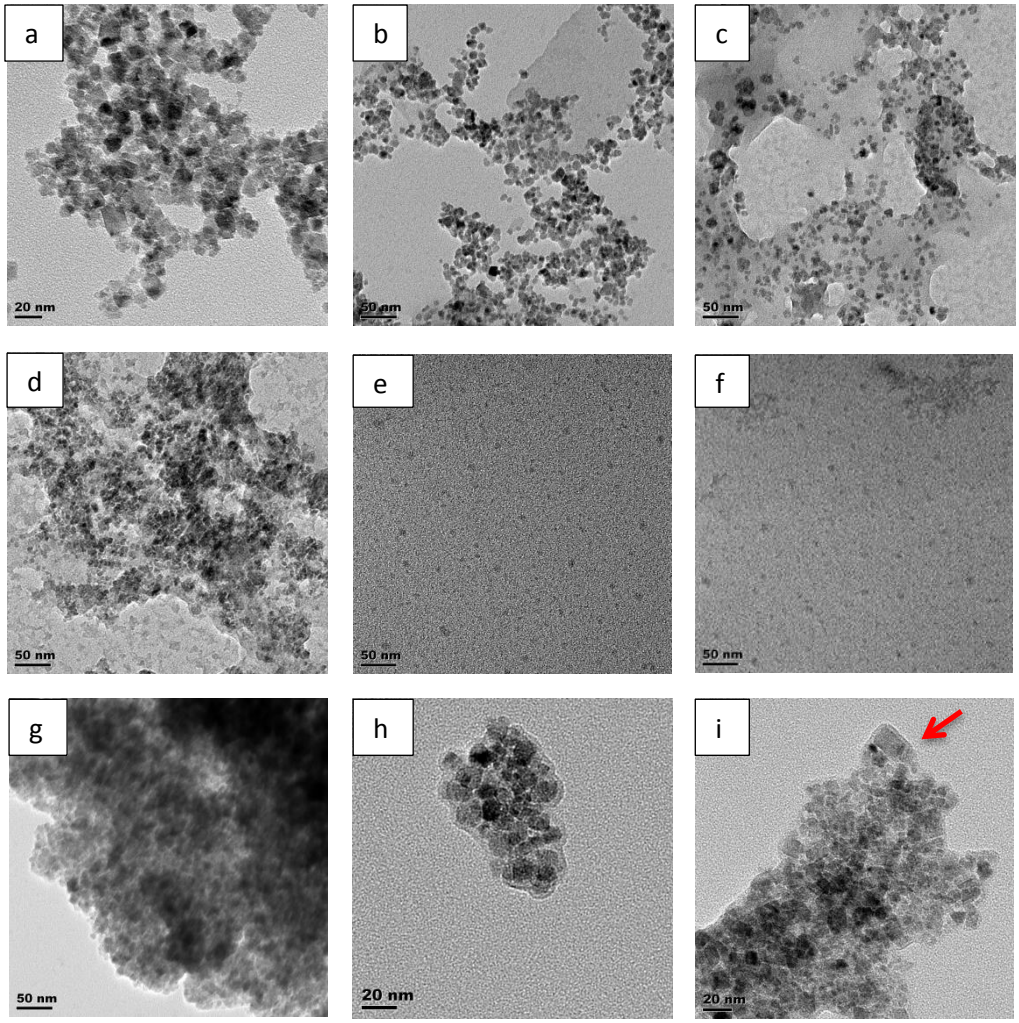


Figure 5.3: TEM images of a) pristine SPMNs, b) 0.1 g CS-EDC-Con A SPMNs, c) 0.5 g CS-EDC-Con A SPMNs, d) 0.9 g CS-EDC-Con A SPMNs, e) 0.1 g SMI-qC$_{12}$ SPMNs, f) 0.5 g SMI-qC$_{12}$ SPMNs, g) 0.9 g SMI-qC$_{12}$ SPMNs, h) 0.5 g CS-EDC SPMNs, i) 0.5 g SMI-qC$_{12}$ SPMNs.

The pristine uncoated nanoparticles were aggregated in Figure 5.3 (a) compared to the polymer coated nanoparticles with 0.1 g and 0.5 g polymer coating (b,c,e,f). Aggregation is observed for uncoated nanoparticles due to the nanoparticles that have attraction towards each other. Coating with a polymer shell enhanced the dispersion in aqueous solution.[14] The nanoparticles with 0.9 g polymer loading, however, showed aggregation, possibly due to the polymer coating of adjacent nanoparticles binding to each other.

Table 5.1: Summary of average diameter and standard deviation for uncoated and polymer coated $Fe_3O_4$ nanoparticles.

| | Uncoated SPMNs | 0.1 g CS-EDC-Con A SPMNs | 0.5 g CS-EDC-Con A SPMNs | 0.9 g CS-EDC-Con A SPMNs | 0.1 g SMI-qC$_{12}$ SPMNs | 0.5 g SMI-qC$_{12}$ SPMNs | 0.9 g SMI-qC$_{12}$ SPMNs |
|---|---|---|---|---|---|---|---|
| Average diameter (nm) | 8.2 ± 2.06 | 8.7 ± 2.03 | 10.2 ± 2.88 | 12.5 ± 6.16 | 9.3 ± 2.63 | 10.1 ± 1.80 | 10.2 ± 2.13 |

The uncoated and coated nanoparticles were largely spherical and had a slight increase in diameter with the increase in polymer loading (Table 5.1). A thin layer of modified chitosan and SMI-q$C_{12}$ coated the nanoparticles and thus lead to an increase in diameter. The size distribution was relatively constant with a 2 nm standard deviation for most nanoparticles except 0.9 g CS-EDC-Con A SPMNs.

### 5.2.3 Thermogravimetric analysis

The percentage content of the polymeric coating around the SPMN core was determined via thermogravimetric analysis (TGA). The TGA curves of the modified chitosan (CS-EDC) and modified SMA (SMI-q$C_{12}$) with 0.1 g, 0.5 g and 0.9 g polymer loading are depicted in Figure 5.4. The weight loss steps were compared to literature which enabled characterization.

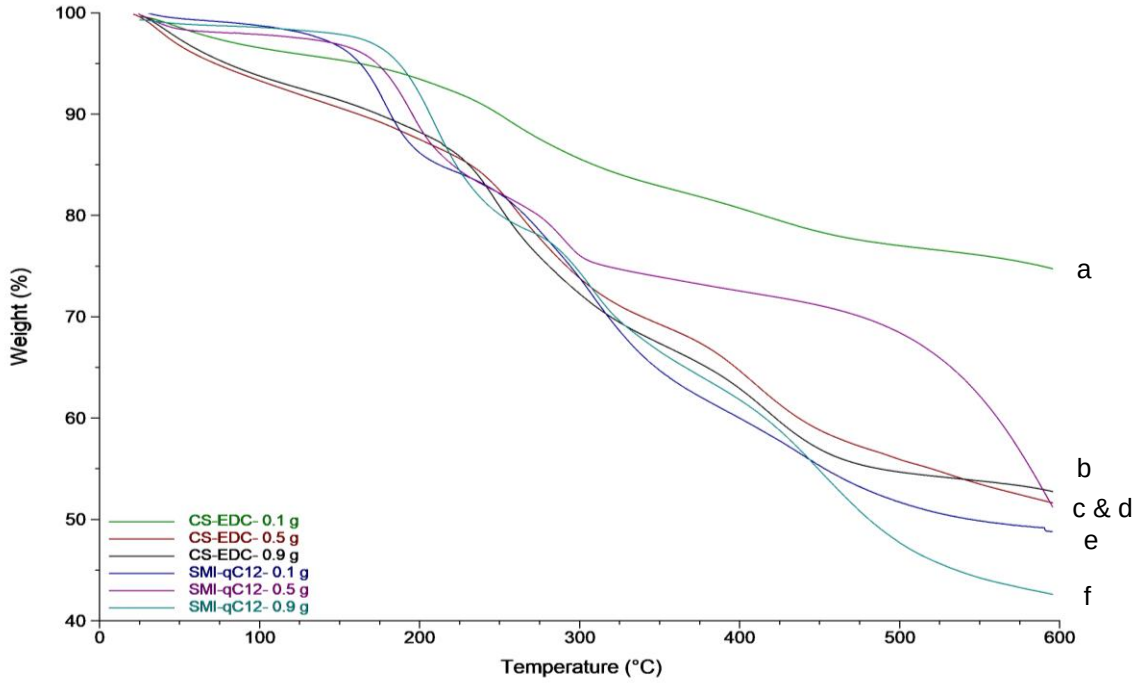


Figure 5.4: TGA curves of a) 0.1 g CS-EDC SPMNs, b) 0.9 g CS-EDC SPMNs, c) 0.5 g CS-EDC SPMNs, d) 0.5g SMI-q$C_{12}$ SPMNs, e) 0.1 g SMI-q$C_{12}$ SPMNs, f) 0.9g SMI-q$C_{12}$ SPMNs.

In Figure 5.5 and Figure 5.6, the first derivative weight loss curves of the modified chitosan and SMA SPMNs are depicted. The first derivative curves were used to identify the magnitude of loss during specific degradation steps as well as the temperature range.

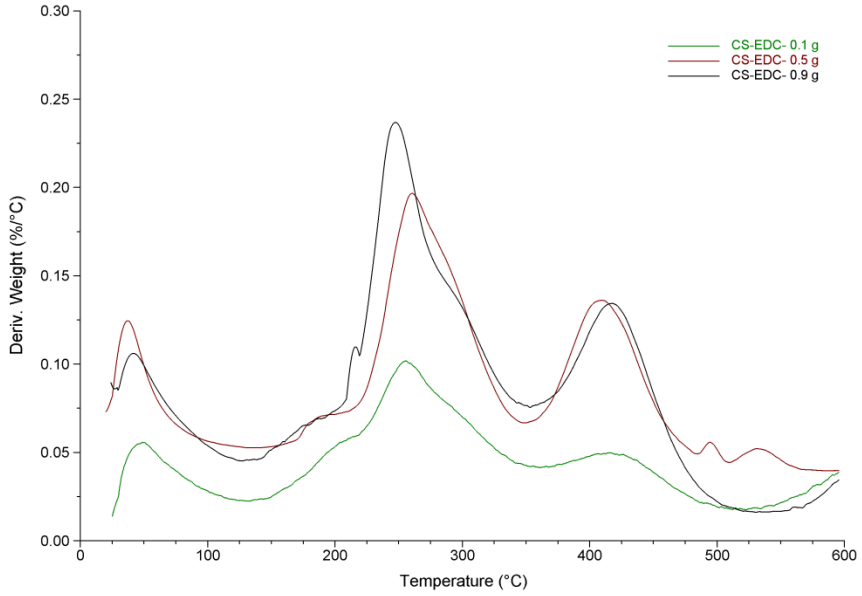


Figure 5.5: TGA first derivative curves of CS-EDC SPMNs with 0.1 g, 0.5 g and 0.9 g polymer loading.

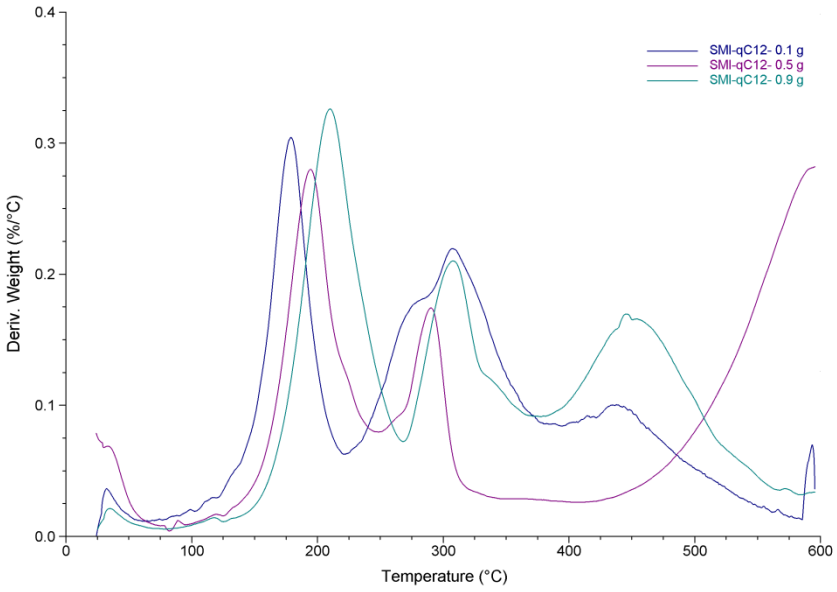


Figure 5.6: TGA first derivative curves of SMI-qC$_{12}$ SPMNs with 0.1 g, 0.5 g and 0.9 g polymer loading.

From Figure 5.4, 5.5 and 5.6, three distinct weight loss steps are observed for the polymer coated SPMNs. The first weight loss step is due to the loss of adsorbed water on the polymer surface as well as surface hydroxyls. This weight loss step occurred from 25 ˚C to 100 ˚C for the SMI-qC$_{12}$ SPMNs (2–3 % weight loss) and from 25 ˚C to 150 ˚C for the CS-EDC SPMNs (4-8 % weight loss). CS-EDC is more hydrophilic compared to SMI-qC$_{12}$ and will thus adsorb more water to the polymer surface. The second and third weight loss steps occurred from 100˚C to 600 ˚C for the SMI-qC$_{12}$ SPMNs and from 150 ˚C to 600 ˚C for the

CS-EDC SPMNs. These weight loss steps can be attributed to the released volatiles and disintegration of the polymer coating.[15,22]

Pristine SPMNs had a minor weight loss of 2 % from 100 ˚C to 600 ˚C. The coated polymers had a weight loss due to degradation of the polymer coating in this temperature range and Equation 5.5 can thus be used to determine the percentage polymer coating.

$$\text{Coating } \% = W_c(\%) - W_u(\%) \qquad 5.5$$

$W_c$ (%) is the percentage of polymer weight lost by the modified chitosan and SMA coated iron oxide nanoparticles and $W_u$ (%) is the percentage weight lost by the uncoated iron oxide nanoparticles.

Table 5.2: Summary of the wt% polymer coating of the CS-EDC and SMI-q$C_{12}$ coated $Fe_3O_4$ nanoparticles.

| | 0.1 g CS-EDC SPMNs | 0.5 g CS-EDC SPMNs | 0.9 g CS-EDC SPMNs | 0.1 g SMI-q$C_{12}$ SPMNs | 0.5 g SMI-q$C_{12}$ SPMNs | 0.9 g SMI-q$C_{12}$ SPMNs |
|---|---|---|---|---|---|---|
| Coating % | 17.75 | 34.25 | 34 | 44 | 45 | 52.5 |

In Table 5.2, it is indicated that the SMI-q$C_{12}$ SPMNs had a higher weight percentage polymer coating compared to the CS-EDC SPMNs. This could be due to the nanoparticle synthesis, *in situ* chitosan coating followed by modification vs. SMA coating of pristine iron oxide nanoparticles and modification. Other factors such as the hydrophobicity and crystallinity of SMA, size of the polymer and packing density also affect the coating %. A direct correlation (linear trend) between polymer loading and coating % was not observed. A higher coating % was, however, achieved with 0.9 g polymer loading compared to 0.1 g polymer loading.

### 5.2.4 Attenuated total reflectance Fourier transform infrared spectroscopy

Fourier transform infrared (FTIR) spectra were utilized to confirm the polymer coating of CS-EDC and SMI-q$C_{12}$ around the superparamagnetic magnetite nanoparticles. The FTIR spectra is illustrated in Figure 5.7 CS-EDC SPMNs (in black), SMI-q$C_{12}$ SPMNs (in red) and pristine (uncoated) SPMNs (in blue). The FTIR spectra illustrate that CS-EDC and SMI-q$C_{12}$ was functionalized onto the iron oxide core. The FTIR spectra of CS-EDC and SMI-q$C_{12}$ was assigned in Chapter 3 and used to identify the polymer coating.

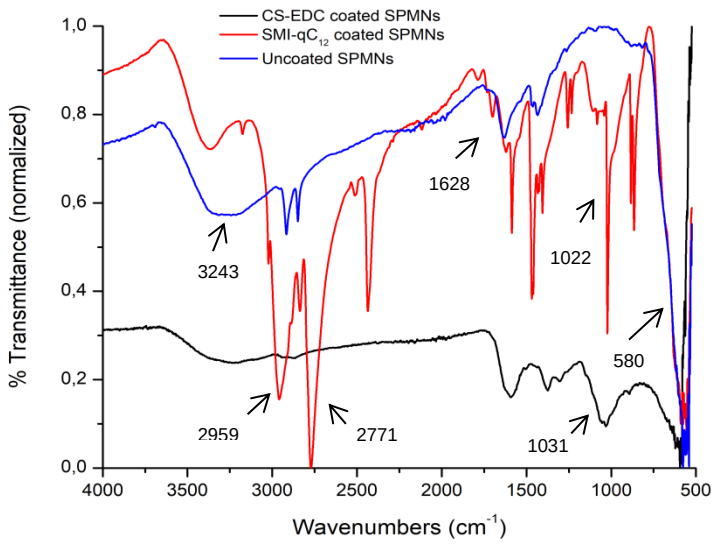


Figure 5.7: FTIR of CS-EDC SPMNs, SMI-qC$_{12}$ SPMNs and uncoated SPMNs.

The characteristic Fe-O vibration of magnetite is observed at 580 cm$^{-1}$ for pristine iron oxide nanoparticles as well as the polymer coated nanoparticles. An O-H stretch (3243 cm$^{-1}$) and bend vibration (1628 cm$^{-1}$) can also be assigned for the uncoated nanoparticles due to surface hydroxyl groups. The CS-EDC SPMNs had a C-O vibration at 1031 cm$^{-1}$ which is characteristic of the chitosan polymer backbone.[23] For the SMI-qC$_{12}$ SPMNs, a significant increase in the intensity of the bands at 2959 and 2771 cm$^{-1}$ can be attributed to the methyl and methylene stretch vibrations of the SMI-qC$_{12}$ alkyl chains. An additional vibration at 1022 cm$^{-1}$ can be assigned to the Si-O symmetric stretch of 3-APTES used for nanoparticle surface activation.[24]

### 5.2.5 Energy dispersive X-ray spectroscopy

Elemental composition analyses were used to confirm the presence of major elements in the synthesized uncoated iron oxide nanoparticles as well as the CS-EDC and SMI-qC$_{12}$ polymer coated SPMNs. Energy dispersive X-ray (EDX) spectroscopy was utilized to quantitatively determine the elemental composition. The pristine SPMNs were largely composed of iron and oxygen elements (Table 5.3) as expected. The presence of additional carbon and nitrogen in the samples confirmed the CS-EDC and SMI-qC$_{12}$ polymer coating around the SPMNs.

Table 5.3: Summary of the elemental composition of CS-EDC and SMI-q$C_{12}$ coated $Fe_3O_4$ nanoparticles.

| | Fe% | O% | N% | C% | Na% | Si% | P% | Cu% | Cl% |
|---|---|---|---|---|---|---|---|---|---|
| Uncoated SPMNs | 59.65 | 33.4 | - | 5.1 | - | 1.55 | - | 0.31 | - |
| 0.1 g CS-EDC SPMNs | 31.69 | 41.31 | 2.35 | 16.76 | 3.57 | 2.17 | 0.37 | 1.36 | 0.41 |
| 0.5 g CS-EDC SPMNs | 24.81 | 26.13 | 3.83 | 39.11 | 2.9 | 1.42 | 0.67 | 0.76 | 0.38 |
| 0.9 g CS-EDC SPMNs | 36.79 | 14.09 | 2.32 | 40.01 | 2.96 | 0.53 | 1.09 | 1.08 | 1.12 |
| 0.1 g SMI-q$C_{12}$ SPMNs | 52.46 | 34.78 | 0.46 | 9.62 | - | 2.27 | - | 0.4 | - |
| 0.5 g SMI-q$C_{12}$ SPMNs | 60.48 | 30.05 | 0.36 | 6.63 | - | 2.12 | - | 0.33 | 0.02 |
| 0.9 g SMI-q$C_{12}$ SPMNs | 55.51 | 31.06 | 0.35 | 10.1 | - | 2.08 | - | 0.9 | - |

### 5.2.6 Horseradish peroxidase enzymatic assay

The horseradish peroxidase (HRP) enzymatic assay (as described in Chapter 4) was performed on the CS-EDC-Con A nanoparticles to determine the biological activity of the immobilized Con A. A colour change from green to dark blue was observed for the CS-EDC-Con A-HRP nanoparticles which confirm qualitatively, that HRP was bound to biologically active Con A immobilized to the nanoparticles (Figure 5.8). The amount of biologically active Con A immobilized to the nanoparticles was quantitatively determined to be 7.5 %.


Figure 5.8: CS-EDC-Con A SPMNs without HRP (left) and with HRP (right).

### 5.2.7 Superconducting quantum interference device

A superconducting quantum interference device (SQUID) was used to determine the magnetic properties of the synthesized pristine (uncoated) magnetite nanoparticles. SQUID was used to determine the saturation magnetization of the nanoparticles as well as their superparamagnetic behaviour. For superparamagnetic nanoparticles, the size of the nanoparticles are smaller than the critical limit (14 nm) in which single domain nanoparticles are observed. When an external magnetic field is applied, the single domain magnets will

align all their magnetic moments in the same direction. The resulting magnetization is thus the largest possible for that specific material and size. Superparamagnetic particles are characterized by zero magnetic remanence and coercivity in the absence of an external magnetic field and will thus not have magnetic memory.[25] The magnetization curves of pristine SPMNs and chitosan coated SPMNs are shown in Figure 5.9. The curve represents the long moment or magnetization as a function of the applied magnetic field (at 300 K).

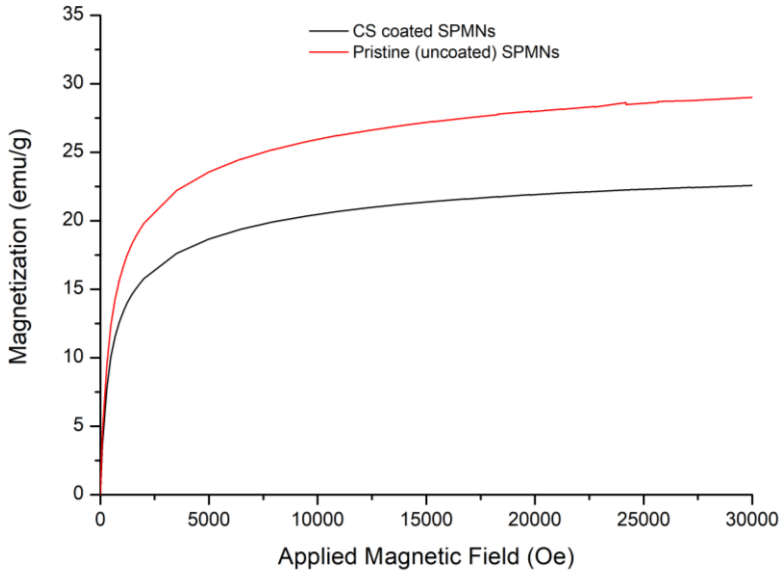


Figure 5.9: SQUID magnetization curves of pristine (uncoated) SPMNs (red) and chitosan coated SPMNs (black).

The SQUID results indicated that the uncoated and chitosan coated nanoparticles were superparamagnetic due to zero coercivity and zero remanence. The saturation magnetization was 29.0 emu/g for the uncoated nanoparticles compared to 22.6 emu/g for the chitosan coated nanoparticles. The polymeric coating thus decreased the effective magnetic moment but superparamagnetic properties were retained.[24] The nanoparticles also experimentally indicated that magnetism was not retained after the removal of an external magnetic field. The synthesized nanoparticles were dispersed in distilled water to form a ferrofluid and could be manipulated with an external magnet. The nanoparticles lost magnetization immediately after removal of the external magnet.

## 5.3 Conclusion

Superparamagnetic magnetite nanoparticles (SPMNs), CS-EDC and SMI-q$C_{12}$ coated SPMN nanocomposites were synthesized via co-precipitation. The chitosan coated and SMA coated nanoparticles could be surface functionalized followed by characterization.

The presence of polymer coating as well as the purity, size and morphology of the nanoparticles were determined. XRD indicated that magnetite was formed due to phase purity and the average crystallite/core size was calculated to be 6.6 nm. TEM was utilized to determine the particle diameters of the uncoated and coated nanoparticles. The uncoated nanoparticles had an average diameter of 8.2 nm, which is larger compared to XRD due to possible magnetically dead layers around the nanoparticles.[26] The polymer coating around the nanoparticles reduced aggregation and a thin layer of polymer coating could be seen. Polymer loading (0.1 g, 0.5 g and 0.9 g) did not increase the average diameter of the nanoparticles significantly. From TGA, a direct correlation (linear trend) between polymer loading and coating % was not observed. A higher coating % was however achieved for 0.9 g polymer loading compared to 0.1 g polymer loading. FTIR and EDX were used to confirm that the iron oxide nanoparticles were coated with a polymer layer. An HRP assay estimated the biological activity of Con A immobilized to the CS-EDC nanoparticles. The uncoated and coated nanoparticles were analysed w.r.t magnetization utilizing SQUID. The nanoparticles retained superparamagnetism, with a slight decrease in saturation magnetization after polymer coating.

## 5.4 Experimental

### 5.4.1 Materials

SMA (poly(styrene-*alt*-maleic anhydride)) was synthesized as outlined in Chapter 3. The following chemicals were used in this part of the project: iron (III) chloride hexahydrate (98 %, Sigma-Aldrich), iron (II) chloride (97%, Sigma-Aldrich), acetic acid (Merck, ≥ 97.7%), ammonium hydroxide (25% in $H_2O$, Merck), ethanol (Sigma-Aldrich, 99.5%), acetone (Sigma-Aldrich, 99.5%), methanol (Sigma-Aldrich, 99.5%), chitosan (Sigma-Aldrich, Mw = 129 000, DDA 75), glutaraldehyde solution (Sigma-Aldrich, 50 wt% in $H_20$), epichlorohydrin (Aldrich, 99%), glycine (Saarchem, 99%), 1,4-dioxane (Sigma-Aldrich, ≥ 99%), sodium hydroxide pellets (Merck, ≥ 97%), *N*-(3-dimethylaminopropyl)-*N*′-ethylcarbodiimide hydrochloride (EDC) (Sigma-Aldrich, ≥ 99%), (3-aminopropyl)triethoxysilane (3-APTES) (Aldrich, 99%), THF (Sigma-Aldrich, 99.5%), DMF (Associated chemical enterprises**,** 99%), isopropanol (Sigma-Aldrich, ≥ 99%), 3-(*N*,*N*-dimethylamino)-1-propylamine (Aldrich, 99%), diethyl ether (Sigma-Aldrich, 99.5%), 1-bromododecane (Aldrich, 97%), pentane (Sigma-Aldrich, 99.5%), hexane (Sigma-Aldrich, 99.5%) Concanavalin A from Canavalia ensiformis (Jack bean) Type VI (Sigma Aldrich), $CaCl_2$ (Merck, 98 %), $MnCl_2$ (Sigma Aldrich, beads 99 %), NaCl (Scienceworld, 98.2 %), KCl (Saarchem, 98.5 %), $Na_2HPO_4$ (Nice laboratory chemicals, 99 %).

### 5.4.2 Characterization Techniques

#### a) Powder X-ray diffraction (P-XRD)

A Siemens D8 Advance diffractometer using Cu Kα radiation (λ = 1.5406 Å) operated at 40 kN and 30 mA was utilized to determine the structural properties of the pristine SPMNs. XRD patterns were recorded in the range 10 - 80° (2θ) with a scan step of 0.034°. The average crystallite size (<D>, Å) could be calculated from line broadening of the XRD spectrum using the Scherrer formula. The samples were dried for 24 h in a vacuum oven at room temperature before analysis, followed by milling the nanoparticles into a fine powder and uniformly packing the nanoparticles into a sample holder to insure a quality diffractogram. The obtained spectrum was corrected for instrumental line broadening and baseline corrected.

#### b) Transmission electron microscopy (TEM)

TEM was utilized to determine the particle size and morphology of the nanoparticles. A JEM 1200EXII model (JEOL, Japan) microscope was used with an accelerated voltage of 120 kV for all the samples. The samples were dried in a vacuum oven at 60°C for 24 h followed by milling into a powder. 1 mg of the SPMN samples was dispersed in distilled water and sonicated for 10 min, after which a drop was pipetted on a carbon-coated 200 mesh copper grid. The samples were dried under ambient conditions, attached to the sample holder and placed in the microscope. An average diameter and size-distribution could be determined by measuring more than 100 particles.

#### c) Thermogravimetric analysis (TGA)

TGA was performed with a Q500 TA instrument in the temperature range of 25 - 600 °C. Pt crucibles were used with about 6 mg dried nanoparticles, under dynamic $N_2$ atmosphere (50 mL/min) and a heating rate of 10 °C/min. The sample holder was calibrated and the samples weighed in a sample component that was flushed with $N_2$ gas and dried.

#### d) Attenuated total reflectance Fourier transform infrared spectroscopy (ATR-FTIR)

Infrared spectra were obtained using a Nicolet FTIR spectrometer from Thermo-Fischer. An ATR accessory with a diamond/ZnSe internal reflection crystal was attached. The spectra were recorded from 4000 $cm^{-1}$ to 500 $cm^{-1}$ with a spectral resolution of 4 $cm^{-1}$. 64 individual scans were taken to generate the spectra as well as 32 scans for the background spectra before each sample. Omnic software, version 8.1, was used for data acquisition and processing.

**e) Energy dispersive X-ray spectroscopy**

The phase compositions of the nanoparticles were quantified using a FE-SEM MERLIN Scanning Electron Microscope (SEM) equipped with an Oxford Instruments® 133 KeV detector and Oxford INCA software. An energy dispersive X-ray spectrometer (EDS) was attached to the microscope and enabled the determination of the chemical or elemental composition of the nanoparticles. (1 mg) of the SPMN samples was dispersed in distilled water and sonicated for 10 min followed by pipetting on aluminium foil. The samples were dried in a vacuum oven and the aluminium foil with nanoparticles mounted on a stub with double sided tape. The sample was then coated with a thin layer of gold, mounted on the SEM stage and analyzed. The beam conditions during the quantitative analyses were 20 kV and approx. 1.4 nA, with the working distance at 15 mm and the specimen beam current -3.92 nA.

**f) Horseradish peroxidase (HRP) enzymatic assay**

A HRP assay was used to determine the biological activity of Con A immobilized to the nanoparticles as described in Chapter 4. The enzymatic assay of peroxidase (EC 1.11.1.7) (Sigma Aldrich) with ABTS as a substrate was used. 50 mg CS-EDC-Con A nanoparticles were incubated in 1.0 mL dilute enzyme solution (1 mg/L) for 3 hours on a laboratory shaker at rt, followed by washing with diluent.

**g) Superconducting quantum interference device (SQUID)**

A SQUID magnetometer was utilized to determine the magnetic nature of pristine SPMNs and polymer coated nanoparticles. A reciprocal sample option was chosen for the samples and performed on a SQUID magnetometer (7 Tesla Magnet). A $10^{-7}$ electromagnetic units (emu) resolution was reached. A liquid SPMN sample (50 mg of 50 mmol $L^{-1}$) was embedded in specific drop-shaped cuvettes (5 mm diameter and 15 mm length). Hysteresis curves were determined at 300 K fixed temperature with a field strength of 0 to 30 kOe. The background of the diamagnetic part of the cuvette was minimized by performing all measurements in a parallel magnetic field in the longitudinal direction to the cuvette. The specific magnetization was calculated in emu/g iron using the signal intensity of the magnetization (emu) and the exact net weight.

### 5.4.3 Experimental procedures

#### a) Synthesis of pristine SPMNs

Pristine SPMNs were synthesized via a co-precipitation reaction developed by Massart where iron(III) chloride and iron(II)chloride were dissolved in acidic media and precipitated in a base to form magnetite nanoparticles.[6]

The experiment was performed under $N_2$ atmosphere. 100 mL of 0.5 % (v/v) aqueous acetic acid was bubbled in a three-necked roundbottom flask for 30 min. 1 g $FeCl_3.6H_2O$ and 0.235 g $FeCl_2$ was added and dissolved for 30 min at 80℃. A pale brown solution was obtained. 17.4 mL of 25 % degassed ammonium hydroxide was rapidly added with vigorous stirring which precipitated the nanoparticles. The solution turned black and was stirred for 1h. The roundbottom was placed in the sonicator at 70℃ for 45 min. The black precipitate was isolated with a magnet and washed 4 times with ethanol and degassed water. The sample was placed in a vacuum oven at 60℃ for 24h.

#### b) CS-EDC-Con A modified coated SPMNs

Chitosan coated iron oxide nanoparticles were synthesized followed by modification via crosslinking (glutaraldehyde) and linker molecules. Con A was immobilized onto the dried CS-EDC nanoparticles.

The experiment was performed under $N_2$ atmosphere. 100 mL of 0.5 % (v/v) aqueous acetic acid was bubbled in a roundbottom flask for 30 min. 0.08 g/ 0.4 g/ 0.73 g solid chitosan (0.1 g/ 0.5 g/ 0.9 g chitosan per 1g $Fe_3O_4$) was dissolved in acetic acid solution for 2h at 80℃. 1 g $FeCl_3.6H_2O$ and 0.235 g $FeCl_2$ was added and dissolved for 30 min. A pale brown solution was obtained. 17.4 mL of 25 % degassed ammonium hydroxide was rapidly added with vigorous stirring to precipitate the chitosan coated nanoparticles. The solution turned black and was stirred for 1 h. The roundbottom was placed in the sonicator at 70℃ for 45 min. The black precipitate was isolated with a magnet and washed 4 times with ethanol and degassed water. The sample was placed in a vacuum oven at 60 ℃ for 24h. The nanoparticle aggregates were milled to a fine powder.

1 g chitosan coated nanoparticles were dispersed in 125 mL distilled water and 25 mL glutaraldehyde. (50 %, 5.6 M) The solution was stirred at 400 rpm for 8h. The obtained nanoparticles were washed with ethanol and water 3 times. The nanoparticles where placed in a vacuum oven at 60℃ for 24h.

1 g crosslinked chitosan coated nanoparticles were suspended in 100 mL distilled water, 100 mL ethanol and 10 g epichlorohydrin. The mixture was refluxed at 100˚C for 3 h. The product was magnetically separated and washed with ethanol and distilled water. 10 g glycine was

suspended in 200 mL 1,4-dioxane in a roundbottom. The solution was mixed with the produced nanoparticles. 80 mL 1.0 M NaOH was added. The mixture was refluxed for 12 h at 100˚C followed by magnetically separating. The product was washed with water and acetone and placed in a vacuum oven to dry.

1 g CS-GLU-GLY nanoparticles were dispersed in 40 mL phosphate buffered saline (PBS) solution. 0.1 g EDC was added and the mixture stirred at 400 rpm for 8h. The nanoparticles were collected with a magnet and washed with PBS 5 times. The nanoparticles were placed in a vacuum oven to dry.

50 mg nanoparticles were placed in 1 mL PBS solution containing Con A (4 mg/mL), $MgCl_2$ (0.01 mg/mL) and $CaCl_2$ (0.01 mg/mL). The samples were incubated on a laboratory shaker at 37 ˚C for 1h, followed my rinsing with PBS (3 times for 10 min at a time) and dried under ambient conditions in a vacuum oven.

**c) SMI-q$C_{12}$ coated SPMNs**

The pristine iron oxide nanoparticles were activated with 3-APTES followed by coating with SMA and further functionalizing to form SMI-q$C_{12}$ coated SPMNs.

1 g milled $Fe_3O_4$ nanoparticles were soaked in 60 mL methanol in a three-necked roundbottom flask and sonicated for 30 min. Ammonium hydroxide (6 mL, 25 % in water) was added and further sonicated for 10 min. 3-APTES (4 mL) was dropwise added under $N_2$ atmosphere and vigorous stirring and heated to 50 ˚C for 8h. The 3-APTES activated nanoparticles were magnetically separated, washed with ethanol and water and then dried in a vacuum oven.

0.1 g/ 0.5 g/ 0.9 g SMA was dissolved in 100 mL THF in a roundbottom flask. 1 g 3-APTES SPMNs were added while stirring followed by sonication for 15 min. The reaction was then refluxed for 3 h at 60 ˚C. The reaction was cooled, isopropanol added to precipitate the SMA and the SMA coated SPMNs magnetically separated. The coated nanoparticles were washed with hexane and dried in a vacuum oven at 60 ˚C.

1 g SMA coated SPMNs were dispersed in 25 mL DMF followed by adding 3-(*N*,*N*-dimethylamino)-1-propylamine (3.3 g) dropwise to the solution. The reaction was heated and refluxed at 170 ˚C for 2h. The reaction was cooled, precipitated in diethyl ether and magnetically separated. The SMI-tC coated SPMNs were dried in a vacuum oven at 60 ˚C.

1 g SMI-tC coated SPMNs were dispersed in 20 mL DMF at rt. 1-bromododecane (1.15 g) was added dropwise with stirring and the reaction heated to 110 ˚C for 48 h. The reaction was cooled, precipitated in diethyl ether, magnetically separated and washed 3 times with pentane. The SMI-q$C_{12}$ SPMNs were dried in a vacuum oven at 60 ˚C.

## 5.5 References


1. Singh, R. Unexpected magnetism in nanomaterials. *J. Magn. Magn. Mater.* **346,** 58–73 (2013).
2. Mahmoudi, M., Sant, S., Wang, B., Laurent, S. & Sen, T. Superparamagnetic iron oxide nanoparticles (SPIONs): Development, surface modification and applications in chemotherapy. *Adv. Drug Deliv. Rev.* **63,** 24–46 (2011).
3. Li, Y., Hu, K., Chen, B., Liang, Y., Fan, F., Sun, J., Zhang, Y. & Gu, N. $Fe_3O_4$@PSC nanoparticle clusters with enhanced magnetic properties prepared by alternating-current magnetic field assisted co-precipitation. *Colloids Surfaces A Physicochem. Eng. Asp.* **520,** 348–354 (2017).
4. Polte, J. Fundamental growth principles of colloidal metal nanoparticles – a new perspective. *CrystEngComm* **17,** 6809–6830 (2015).
5. Borlido, L., Azevedo, A. M., Roque, A. C. A. & Aires-Barros, M. R. Magnetic separations in biotechnology. *Biotechnol. Adv.* **31,** 1374–1385 (2013).
6. Massart, R. Preparation of aqueous magnetic liquids in alkaline and acidic media. *IEEE Trans. Magn.* **17,** 1247–1248 (1981).
7. Ali, A., Zafar, H., Zia, M., ul Haq, I., Phull, A. R., Ali, J. S. & Hussain, A. Synthesis, characterization, applications, and challenges of iron oxide nanoparticles. *Nanotechnol. Sci. Appl.* **9,** 49–67 (2016).
8. Monazam, E. R., Breault, R. W. & Siriwardane, R. Kinetics of magnetite ($Fe_3O_4$) oxidation to hematite ($Fe_2O_3$) in air for chemical looping combustion. *Ind. Eng. Chem. Res.* **53,** 13320–13328 (2014).
9. Alp, E. & Aydogan, N. A comparative study: Synthesis of superparamagnetic iron oxide nanoparticles in air and $N_2$ atmosphere. *Colloids Surfaces A Physicochem. Eng. Asp.* **510,** 205–212 (2016).
10. Maity, D. & Agrawal, D. C. Synthesis of iron oxide nanoparticles under oxidizing environment and their stabilization in aqueous and non-aqueous media. *J. Magn. Magn. Mater.* **308,** 46–55 (2007).
11. Mascolo, M. C., Pei, Y. & Ring, T. A. Room Temperature Co-Precipitation Synthesis of Magnetite Nanoparticles in a Large ph Window with Different Bases. *Materials (Basel).* **6,** 5549–5567 (2013).
12. Zhuang, L., Zhang, W., Zhao, Y., Shen, H., Lin, H. & Liang, J. Preparation and characterization of $Fe_3O_4$ particles with novel nanosheets morphology and magnetochromatic property by a modified solvothermal method. *Sci. Rep.* **5,** 1–6 (2015).
13. Dias, A. M. G. C., Hussain, A., Marcos, A. S. & Roque, A. C. A. A biotechnological perspective on the application of iron oxide magnetic colloids modified with polysaccharides. *Biotechnol. Adv.* **29,** 142–155 (2011).
14. Chandra, A., Turng, L. S., Li, K. & Huang, H. X. Fracture behavior and optical properties of melt compounded semi-transparent polycarbonate (PC)/alumina nanocomposites. *Compos. Part A Appl. Sci. Manuf.* **42,** 1903–1909 (2011).
15. Long, J., Jiao, A., Wei, B., Wu, Z., Zhang, Y., Xu, X. & Jin, Z. A novel method for pullulanase immobilized onto magnetic chitosan/$Fe_3O_4$ composite nanoparticles by in situ preparation and evaluation of the enzyme stability. *J. Mol. Catal. B Enzym.* **109,** 53–61 (2014).
16. Chandra, A., Turng, L., Gopalan, P., Rowell, R. M. & Shaoqin, G. Semitransparent Poly(styrene-*r*-maleic anhydride)/ Alumina Nanocomposites for Optical Applications. *J. Appl. Polym. Sci.* **105,** 2728–2736 (2007).
17. Wang, N., Zhu, L., Wang, D., Wang, M., Lin, Z. & Tang, H. Sono-assisted preparation of highly-efficient peroxidase-like $Fe_3O_4$ magnetic nanoparticles for catalytic removal of organic pollutants with $H_2O_2$. *Ultrason. Sonochem.* **17,** 526–533 (2010).
18. Kumari, S. & Khan, S. Defluoridation technology for drinking water and tea by green synthesized $Fe_3O_4/Al_2O_3$ nanoparticles coated polyurethane foams for rural communities. *Sci.*

*Rep.* **7,** 1–12 (2017).

19. Cheng, W., Tang, K., Qi, Y., Sheng, J. & Liu, Z. One-step synthesis of superparamagnetic monodisperse porous $Fe_3O_4$ hollow and core-shell spheres. *J. Mater. Chem.* **20,** 1799 (2010).

20. Kazeminezhad, I. & Mosivand, S. Phase transition of electrooxidized $Fe_3O_4$ to γ and α-$Fe_2O_3$ nanoparticles using sintering treatment. *Acta Phys. Pol. A* **125,** 1210–1214 (2014).

21. Bui, T. Q., Nu-Cam Ton, S., Duong, A. T. & Tran, H. T. Dependence of magnetic responsiveness on particle size of magnetite nanoparticles synthesised by co-precipitation method and solvothermal method. *J. Sci. Adv. Mater. Devices* (2017). doi:https://doi.org/10.1016/j.jsamd.2017.11.002

22. Unsoy, G., Yalcin, S., Khodadust, R., Gunduz, G. & Gunduz, U. Synthesis optimization and characterization of chitosan coated iron oxide nanoparticles produced for biomedical applications. *J. Nanoparticle Res.* **14,** (2012).

23. Yuwei, C. & Jianlong, W. Preparation and characterization of magnetic chitosan nanoparticles and its application for Cu(II) removal. *Chem. Eng. J.* **168,** 286–292 (2011).

24. Thangaraj, B., Jia, Z., Dai, L., Liu, D. & Du, W. Effect of silica coating on $Fe_3O_4$ magnetic nanoparticles for lipase immobilization and their application for biodiesel production. *Arab. J. Chem.* (2016). doi:10.1016/j.arabjc.2016.09.004

25. Gyergyek, S., Makovec, D., Jagodič, M., Drofenik, M., Schenk, K., Jordan, O., Kovač, J., Dražič, G. & Hofmann, H. Hydrothermal growth of iron oxide NPs with a uniform size distribution for magnetically induced hyperthermia: Structural, colloidal and magnetic properties. *J. Alloys Compd.* **694,** 261–271 (2017).

26. Shaterabadi, Z., Nabiyouni, G. & Soleymani, M. High impact of in situ dextran coating on biocompatibility, stability and magnetic properties of iron oxide nanoparticles. *Mater. Sci. Eng. C* **75,** 947–956 (2017).

# Chapter 6

Affinity studies between modified chitosan and modified SMA nano-substrates and mycobacteria

## 6.1 Introduction

The capturing capabilities (or bacterial affinity) of the nano-substrates are influenced by the characteristics of the *Mycobacterium tuberculosis (Mtb)* cell wall, the functionalized substrates as well as the experimental conditions. A favourable experimental temperature, pH and incubation period will thus be used and the influence of bacterial concentration determined. The cell wall chemistry of *Mtb* and the binding mechanism of *Mtb* to the functionalized nano-substrates will thus be investigated.

### 6.1.1 *Mtb* Cell Wall Chemistry

The *Mtb* cell wall chemistry is complex with a large amount of high molecular weight lipids. This makes the bacteria resistant to disinfectants and laboratory stains such as Gram's stain. The pathogen is gram positive but the wax-rich, hydrophobic cell wall lends the bacilli acid fast properties. The cell wall glycolipids and mycolic acids are responsible for some of the immune responses. *Mtb* can bind to a variety of host cell receptors such as surfactant protein receptors and macrophage receptors.[1]

The *Mtb* has a multilaminate cell wall composed of peptidoglycan, complex polysaccharides, covalently linked lipids and free lipids/lipoglycans (Figure 6.1). The bacterium has characteristic mycolic acids where these long chain α-branched, β-hydroxylated fatty acids are covalently linked to the arabinogalactan polysaccharide layer. A glycolipid layer forms an outer "mycomembrane" around the mycolic acid layer which is characteristic of Gram negative bacteria. The outer layer of the mycobacterium membrane is composed of a variety of lipids such as trehalose dimycolates (TDMs), glycopeptidolipids (GPLs), phthiocerol dimycocerosates (PDIMs), sulfolipids, phenolic glycolipids (PGLs), lipooligosaccharides and mannose containing biomolecules such as mannose-capped lipoarabinomannan (Man-LAM).[2] The outer layer is electron dense and negatively charged which can associate with substrates via surface electrostatic interactions.[3]

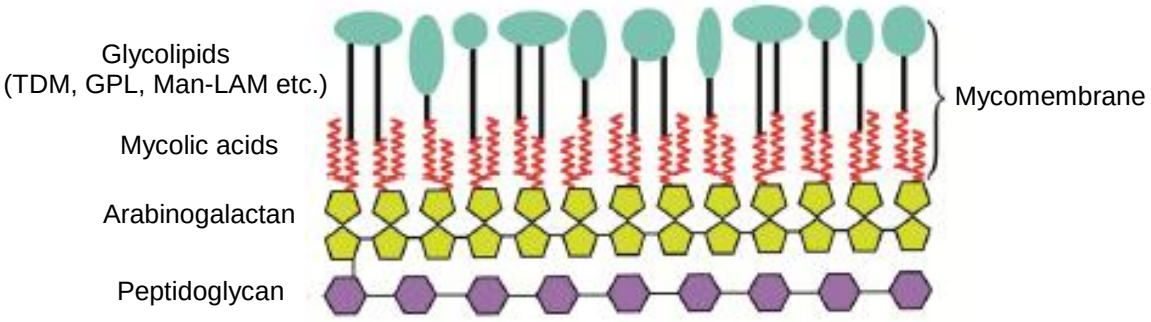


Figure 6.1: Simplified cell wall structure of *Mycobacterium tuberculosis*.[2]

### 6.1.2 Interactions between *Mtb* and substrates

Bacterial adhesion to substrates and host cells can occur via mechanisms such as biospecific (protein-protein or carbohydrate-protein) and non-biospecific (hydrophobic or electrostatic).[4] Substrate surfaces with immobilized Concanavalin A (Con A) protein can be used for biospecific bacterial adhesion. Con A is a carbohydrate binding protein that can bind to the mannose containing groups on the outer *Mtb* cell wall layer.[5] Chemically modified substrates with hydrophobic quaternary ammonium groups such as quaternary chitosan and SMA have shown to possess bacterial adhesion via non-specific hydrophobic and electrostatic interactions. Quaternary ammonium groups are able to damage host cells by disrupting the cellular membrane which leads to cell lysis and death. The molecular weight and the alkyl chain length of quaternary ammonium cations can affect the anti-bacterial activity.[6,7] Substrates containing 12-14 carbon alkyl chain lengths have shown to be effective against Gram positive and Gram negative bacteria.[8] These anti-bacterial studies can be an indication of bacterial adhesion.

## 6.2 Results and Discussion

The modified chitosan bi-component nanofibers and modified SMA nanofibers (as described in Chapter 4) as well as the CS-EDC and SMI-q$C_{12}$ SPMNs (as described in Chapter 5) coated with three different polymer loadings will be tested for their affinity towards *Mtb*. These modified polymers were chosen for their possible capability to capture *Mtb*. Bacillus Calmette–Guérin (BCG) was used as *Mtb* mimic as it is the live attenuated strain of *Mycobacterium bovis* and genetically similar to *Mtb*.[9] The BCG was fluorescent protein encoded (mCherry), as staining BCG captured nanofibers stained the bacteria as well as the fibers.

A preliminary BCG-mCherry affinity study was performed on the nanofibers in order to determine which polymer-and-functional-moiety combination had the highest affinity for the bacteria. The nanofibers were incubated in BCG-mCherry followed by rinsing the nanofibers three times for 10 min with phosphate buffered saline (PBS) solution. The captured bacteria on the nanofibers were evaluated as an indication of chemical interaction and thus BCG-mCherry affinity. The SPMNs nanoparticles were coated with the two polymer-and-functional-moiety combinations with the highest BCG affinity in the nanofiber study (SMI-$qC_{12}$ and CS-EDC-Con A) in three different polymer loadings. A dilution study was performed on the nanoparticles in order to determine the sensitivity and thus limit of detection of bacteria. The nanofibers and nanoparticles were evaluated for BCG-mCherry affinity by fluorescence microscopy (FM), light microscopy (LM) and transmission electron microscopy (TEM).

### 6.2.1 Nanofibers

CS-EDC-Con A, CS-$qC_{10}$ and CS-$qC_{12}$ were electrospun into bi-component nanofibers with polyvinyl alcohol (PVA), poly(L-lactide) (PLA) and polycaprolactam (Nylon 6) and crosslinked. The SMA-Con A, SMI-$qC_{10}$ and SMI-$qC_{12}$ nanofibers were also electrospun and crosslinked as outlined in Chapter 4.

#### a) BCG-mCherry affinity studies

10 mg of the crosslinked nanofiber mats were placed in 5 mL BCG-mCherry culture followed by incubating at 37 °C for 1 h on a laboratory shaker. The nanofibers were removed and washed three times with PBS for 10 min to remove bacteria that were not fully attached to the surfaces. The fibers blended with PVA were in situ crosslinked with 1,2,3,4-butanetetracarboxylic acid (BA) while the fibers blended with PLA were crosslinked with glutaraldehyde for stability. All the nanofibers were stabilized with heat in order to insure stability in PBS. The nanofiber mats were incubated at a concentration of $OD_{600nm}$ = 6/18.78 $\times 10^7$ colony-forming units (CFU)/mL to determine which polymer-and-functional-moiety combination had the highest BCG-mCherry affinity.[10] A confocal microscope in fluorescence and transmission modes was used to detect BCG-mCherry captured on the nanofiber substrates (excitation wavelength of 543 nm to visualize the red bacteria). The nanofibers were evaluated and compared for BCG-mCherry capture as seen in Figure 6.2 where FM is used to visualize bacteria on the nanofiber mats and LM overlaid with FM to visualize the morphology at the given area (Addendum B). Each nanofiber mat was tested for negative controls (without BCG-mCherry) and no fluorescence was observed.

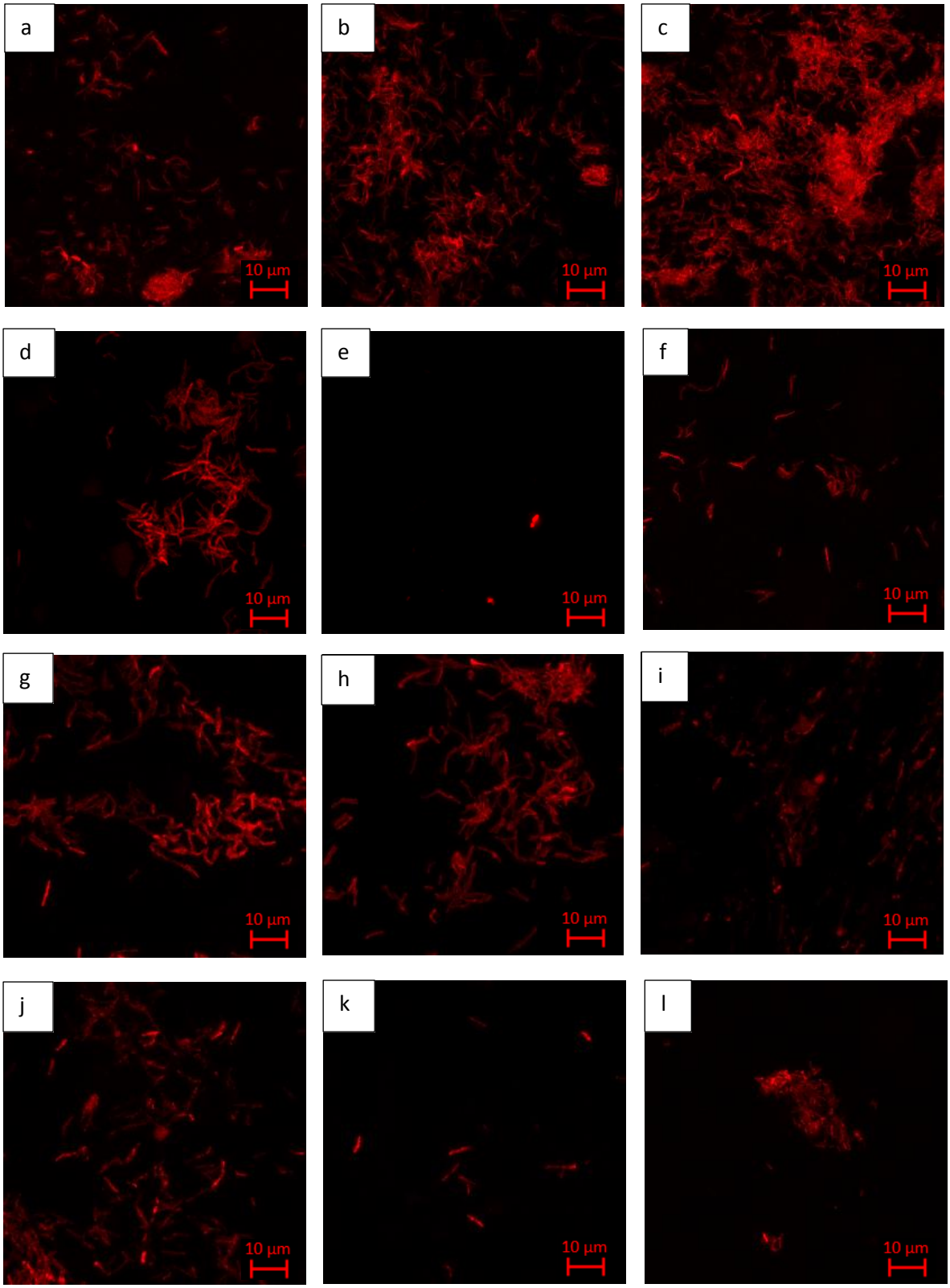


Figure 6.2: Fluorescence microscopy (FM) images of nanofibers incubated in $OD_{600nm}$=6 a) SMI-Con A, b) SMI-$qC_{10}$, c) SMI-$qC_{12}$, d) CS-EDC-Con A/PVA, e)CS-$qC_{10}$/PVA, f) CS-$qC_{12}$/PVA, g) CS-EDC-Con A/PLA, h) Cs-$qC_{10}$/PLA, i) CS-$qC_{12}$/PLA, j) CS-EDC-Con A/Nylon 6, k) CS-$qC_{10}$/Nylon 6, l) CS-$qC_{12}$/Nylon 6.

The SMI-q$C_{12}$ nanofibers showed the greatest affinity towards BCG-mCherry bacteria as seen in Figure 6.2 (c). Various red fluorescent rod shaped bacterial colonies attached to the nanofiber surface for the SMI-q$C_{12}$ nanofibers compared to more disperse single bacteria and single colonies for the various chitosan nanofibers. The densely packed bacteria colonies could be attributed to biofilm formation on the surface of the nanofibers. A biofilm is formed when the bacteria attach to the nanofiber surface followed by the stress induced self-production of an extracellular polymeric matrix that holds the bacteria together. The extracellular polymeric matrix consists of exopolysaccharides, proteins, DNA and lipids (including glycolipids and mycolic acid).[11,12] The positively charged quaternary ammonium moieties of SMI-q$C_{12}$ and CS-q$C_{12}$ can interact with the negatively charged electron dense bacteria cell wall (lipid layer) via electrostatic interaction. The electrostatic interaction leads to attachment of the bacteria to the nanofiber surface. The hydrophobic alkyl chains of $C_{12}$ can also attach to the hydrophobic outer layer (mycolic acids) of the bacteria cell wall which contributes to BCG-mCherry affinity.[13] Hydrophobicity is chain length dependent, the $C_{12}$ chains thus had a higher BCG-mCherry affinity compared to $C_{10}$ due to an increase in hydrophobicity.

For the modified chitosan nanofibers, Figure 6.2 (d-l), CS-EDC-Con A had the highest affinity for BCG-mCherry when blending with the all the non-ionogenic polymers (PVA, PLA and Nylon 6). Con A can bind to the carbohydrate based structures on the surface of BCG-mCherry such as mannose. Mannose is present in the form of mannose-capped lipoarabinomannan (Man-LAM) and is accessible for specific interactions with Con A.[2] The modified chitosan derivatives blended with PLA, Figure 6.2 (g-i), had the highest affinity for BCG-mCherry compared to the other non-ionogenic blending polymers (PVA and Nylon 6). PLA is relatively hydrophobic and biocompatible which could improve adhesion to the hydrophobic outer layer of the bacteria.[14]

The SMI-q$C_{12}$ nanofibers had the highest affinity for BCG-mCherry while the CS-EDC-Con A nanofibers had the highest affinity for BCG-mCherry among the chitosan derivatives. These polymer-and-functional-moiety combinations were thus utilized to coat SPMNs.

### 6.2.2 SPMNs

The SMI-q$C_{12}$ and CS-EDC-Con A superparamagnetic magnetite nanoparticles (SPMN nanocomposites) with 0.1 g, 0.5 g and 0.9 g polymer loading per 1 g magnetite nanoparticles were evaluated for their affinity towards mycobacteria. The synthesis and characterization of SMI-q$C_{12}$ SPMNs and CS-EDC-Con A SPMNs are outlined in Chapter 5. A dilution study was performed to determine the limit of detection of the nanoparticles.

### a) BCG-mCherry affinity studies

50 mg of the pristine SPMNs and polymer coated SPMNs were placed in 5 mL BCG-mCherry culture followed by incubating at 37 °C for 1 h on a laboratory shaker. The nanoparticles were magnetically separated and washed three times with PBS for 10 min to remove bacteria that were not fully attached to the surfaces. A magnet can be placed underneath the nanoparticles, which attracts the nanoparticles out of the BCG-mCherry culture solution. The BCG-mCherry can be decanted followed by washing with PBS. The superparamagnetic magnetite nanoparticles can thus be dispersed in bacteria solution, adhere to the bacteria via the functionalized polymer followed by extracting the nanoparticles with an external magnet. Refer to Figure 6.3 for the chemical structures of the functionalized polymers that were used to coat the SPMNs.

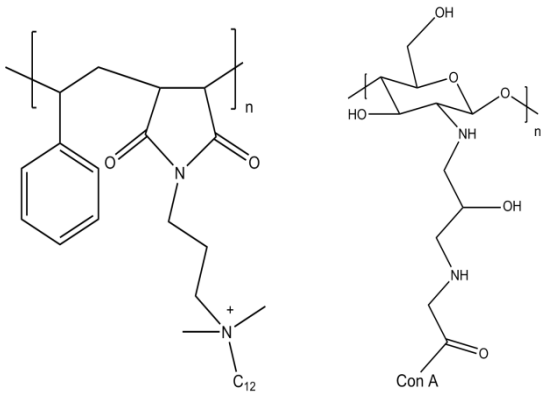


Figure 6.3: Chemical structures of SMI-q$C_{12}$ (left) and CS-EDC-Con A (right).

The nanoparticles with different polymer loadings (0.1 g, 0.5 g and 0.9 g) were evaluated and compared for BCG-mCherry capture as seen in Figure 6.4 and 6.5 where FM is used to visualize the nanoparticles attached to the bacteria. A dilution study with ten-fold serial dilutions was performed to determine the limit of detection. LM overlaid with FM was used to visualize the morphology at the given area (Addendum C). The pristine SPMNs did not have fluorescence at the excitation wavelength of BCG-mCherry.

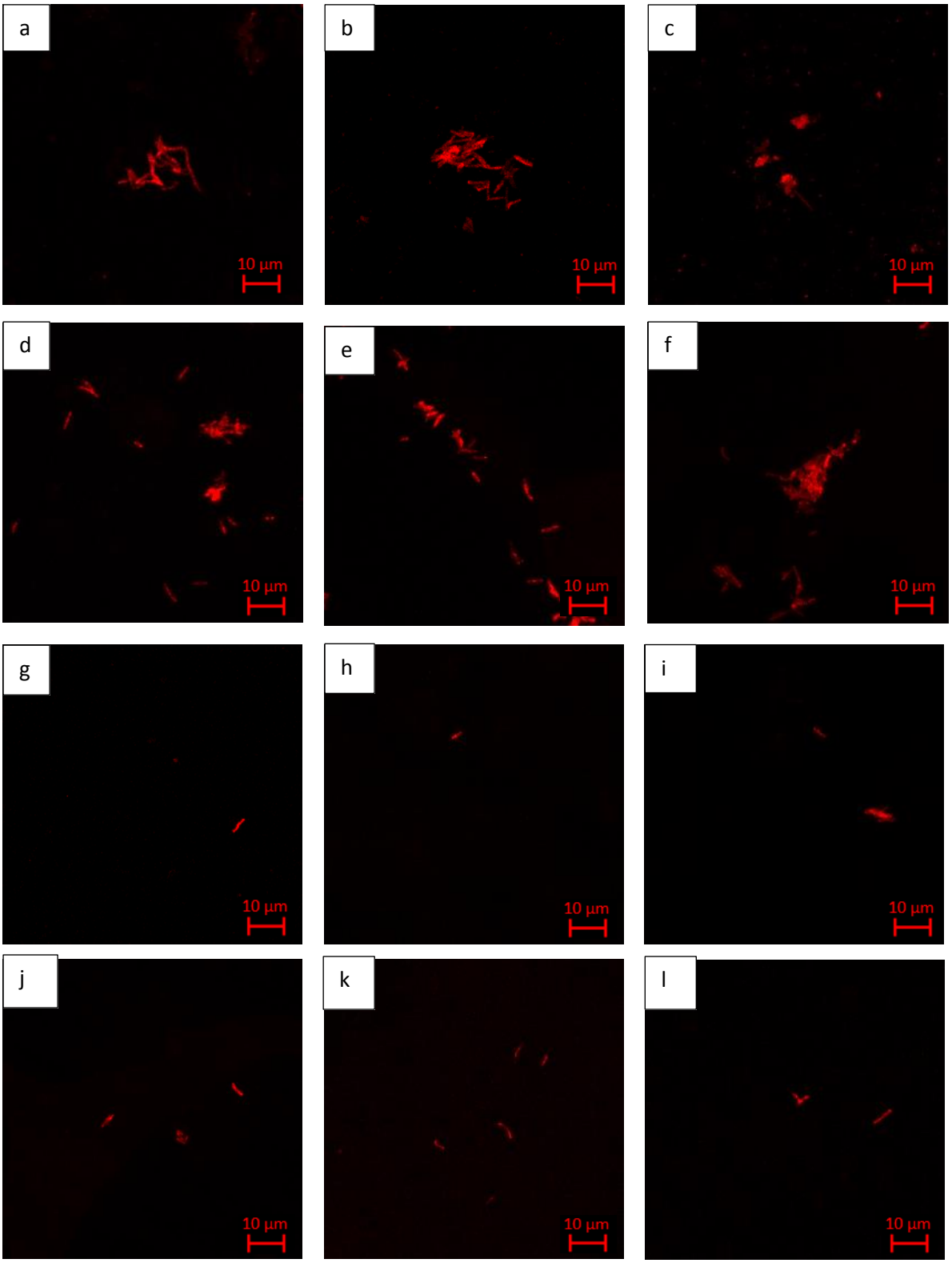


Figure 6.4: FM images at $OD_{600nm}$ = 7 for a) 0.1 g CS-EDC-Con A SPMNs, b) 0.5 g CS-EDC-Con A SPMNs, c) 0.9 g CS-EDC-Con A SPMNs, d) 0.1 g SMI-q$C_{12}$ SPMNs, e) 0.5 g SMI-q$C_{12}$ SPMNs, f) 0.9 g SMI-q$C_{12}$ SPMNs, at $OD_{600nm}$ = 0.7 for g) 0.1 g CS-EDC-Con A SPMNs, h) 0.1 g SMI-q$C_{12}$ SPMNs, i) 0.5 g SMI-q$C_{12}$ SPMNs, j) 0.9 g SMI-q$C_{12}$ SPMNs, at $OD_{600nm}$ = 0.07 for k) 0.1 g SMI-q$C_{12}$ SPMNs and l) 0.5 g SMI-q$C_{12}$ SPMNs.

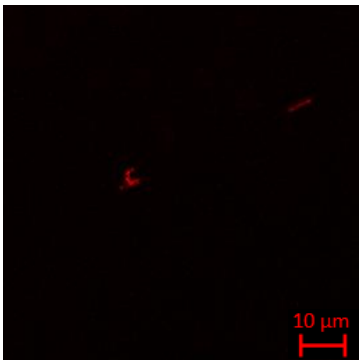


Figure 6.5 Fluorescence microscopy image at $OD_{600nm}$ = 0.07 for 0.9 g SMI-$qC_{12}$ SPMNs.

The coated SPMNs had similar BCG-mCherry affinity for the initial dilution of $OD_{600nm}$ = 7/21.91×$10^7$ CFU/mL as seen in Figure 6.4 (a-f). Only the 0.9 g CS-EDC-Con A SPMNs Figure 6.4 (c) had less rod shaped captured bacteria but fluorescence was still observed. After the second dilution of $OD_{600nm}$ = 0.7/2.19 ×$10^7$ CFU/mL, however, no fluorescence were observed for the 0.5 g CS-EDC-Con A SPMNs and 0.9 g CS-EDC-Con A SPMNs. After the third dilution of $OD_{600nm}$ = 0.07/0.22 ×$10^7$ CFU/mL, only the SMI-$qC_{12}$ SPMNs captured bacteria as seen in Figure 6.4 (k, l) and Figure 6.5. The SMI-$qC_{12}$ SPMNs thus had the highest affinity for BCG-mCherry which was also observed in the nanofiber study. The SPMNs, however, captured less bacteria compared to the nanofibers which can be attributed to the number of functional groups available to bind to the bacteria. Less functional groups are available due to the polymer coating that binds to the hydroxyl groups of iron oxide. The effect of the polymer loading could not be estimated from FM as the 0.1 g, 0.5 g and 0.9 g SMI-$qC_{12}$ SPMNs had similar BCG-mCherry affinity at the lowest $OD_{600nm}$ = 0.07 dilution. The adhesion of the nanoparticles to the bacteria was thus investigated with TEM.

**b) TEM**

Transmission electron microscopy (TEM) was used to observe the physical adhesion of the SPMNs to the bacteria. The nanoparticles used at a BCG-mCherry dilution of $OD_{600nm}$ = 7 were dispersed in PBS, sonicated, placed on TEM grids and dried under ambient conditions. The 0.9 g CS-EDC-Con A SPMNs and 0.1 g SMI-$qC_{12}$ SPMNs did not show BCG-mCherry attachment via TEM. In Figure 6.6 the SPMNs attached to BCG-mCherry can be observed.

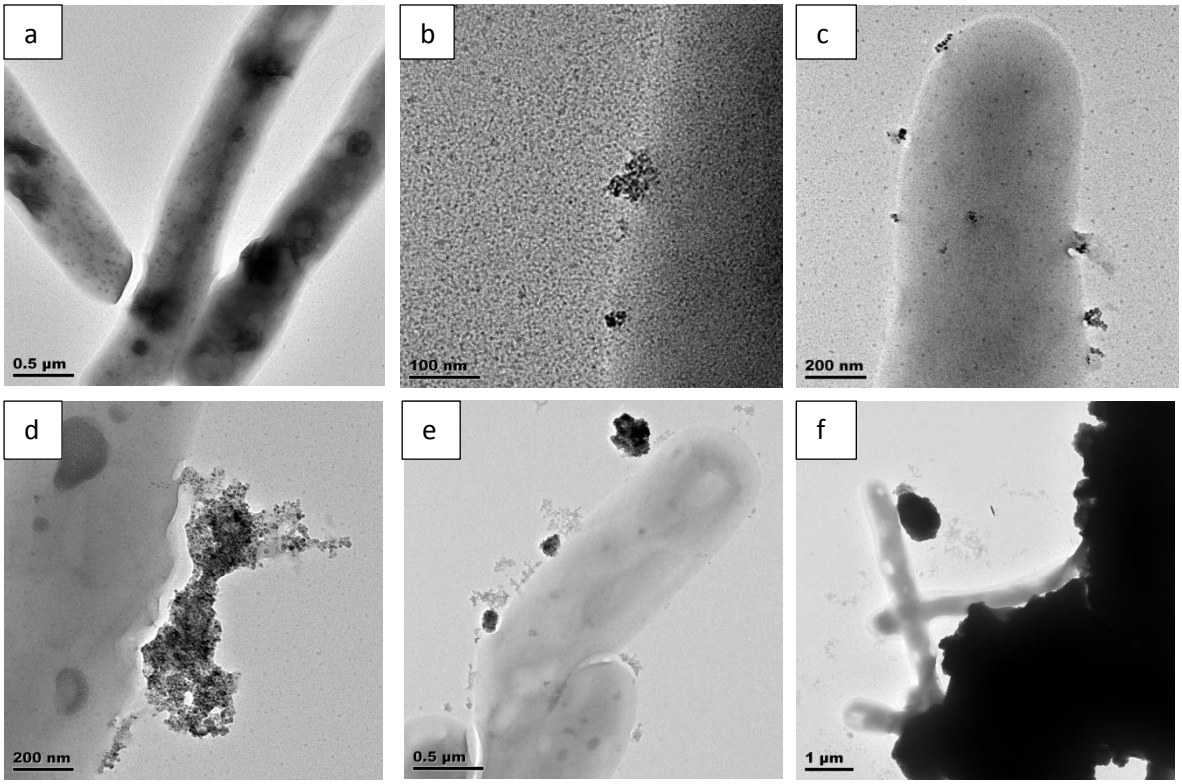


Figure 6.6: TEM images of nanoparticles incubated with BCG-mCherry at $OD_{600nm}$ = 7 a) BCG-mCherry bacteria, b) 0.1 g CS-EDC-Con A SPMNs , c and d) 0.5 g CS-EDC-Con A SPMNs, e) 0.5 SMI-$qC_{12}$ SPMNs, f) 0.9 SMI-$qC_{12}$ SPMNs.

The large rod shaped bacteria with a diameter of 2.5-4 µm was observed in Figure 6.6. The polymer coated SPMNs formed darker areas around the bacteria. The interface between the bacteria and the nanoparticles can be seen in Figure 6.6 (d). A lighter area is observed where the nanoparticles are attached to the bacteria which could be attributed to bacterial shrinkage after drying.[15] The 0.9 g SMI-$qC_{12}$ SPMNs showed the highest affinity for BCG-mCherry, Figure 6.6 (f), where colonies of bacteria were attached to the nanoparticles compared to individual bacteria for the lower polymer loadings.

## 6.3 Conclusion

BCG-mCherry was used as a fluorophore tagged *Mtb* mimic and could be successfully captured onto the modified chitosan/non-ionogenic polymer nanofibers, modified SMA nanofibers, CS-EDC-Con A SPMNs and SMI-$qC_{12}$ SPMNs. The modified polymers were functionalized with quaternary ammonium groups as well as Con A.

The SMI-$qC_{12}$ nanofibers showed the greatest affinity towards BCG-mCherry bacteria. Bacteria were captured due to the positively charged quaternary ammonium moieties of

SMI-q$C_{12}$ that can interact with the negatively charged electron dense bacteria cell wall (lipid layer) via electrostatic interaction. The hydrophobic alkyl chains of $C_{12}$ can also attach to the hydrophobic outer layer (mycolic acids) of the bacteria cell wall which contributes to BCG-mCherry affinity. CS-EDC-Con A had the highest affinity for BCG-mCherry for the modified chitosan nanofibers. Bacteria can thus be captured by Con A that binds to the carbohydrate based structures on the surface of BCG-mCherry such as mannose. The modified chitosan nanofibers blended with PLA as non-ionogenic blending polymer had the highest BCG-mCherry affinity. PLA is relatively hydrophobic and biocompatible which could improve adhesion to the hydrophobic outer layer of the bacteria.

SPMNs were coated with SMI-q$C_{12}$ and CS-EDC-Con A at 0.1 g 0.5 g and 0.9 g polymer loadings. The SMI-q$C_{12}$ SPMNs had the highest BCG-mCherry affinity with a sensitivity of $OD_{600nm}$ = 0.07/0.22 $\times 10^7$ CFU/mL. The 0.9 g SMI-q$C_{12}$ SPMNs captured the most BCG-mCherry bacteria as determined via TEM.

Based on the results non-specific electrostatic and hydrophobic interactions (SMI-q$C_{12}$) lead to a higher BCG-mCherry affinity compared to specific carbohydrate-protein binding (CS-EDC-Con A).

## 6.4 Experimental

### 6.4.1 Characterization Techniques

**a) Fluorescence microscopy (FM)**

The modified chitosan and SMA nanofibers as well as the modified chitosan and SMA coated SPMNs were imaged using a Zeiss LSM 880 confocal microscope (ZEN 2.3 software) coupled with an Argon multiline laser. The nanofibers were placed in a thin layer on a microscope slide in order to visualize the bacteria. The nanoparticles were sonicated in PBS for 10 seconds followed by placing a drop on the microscope slide. An argon laser with an excitation wavelength of 543 nm was used (GaAsP detector 32+2 PMT) for excitation of mCherry fluorescence. Transmission and Light microscopy images were obtained simultaneously with a transmitted light detector T-PMT.

**b) Transmission electron microscopy (TEM)**

The nanoparticles that captured BCG-mCherry was visualised with TEM. A JEM 1200EXII model (JEOL, Japan) microscope with a 120 kV accelerated voltage was used. 1 mg nanoparticles were sonicated in PBS for 10 seconds followed by placing a drop on a carbon-

coated 200 mesh copper grid. The grids were dried at ambient conditions before attaching to the sample holder on the microscope.

### 6.4.2 BCG-mCherry study

#### a) BCG-mCherry culture

mCherry-expressing BCG (BCG-mCherry) was obtained by transforming BCG Pasteur with pMSG432 (episomal plasmid encoding mCherry and enabling hygromycin resistance). The BCG-mCherry strains were grown at 37 °C in Middlebrook 7H9 growth medium supplemented with 10% albumin/dextrose/saline, 0.5 % glycerol and 0.05% Tween-80 in 50 µg/mL hygromycin to an $OD_{600nm}$ of 1. The culture was subsequently inoculated in 20 ml Sauton's medium ($OD_{600nm}$ = 0.05) and further incubated at 37 °C until the culture reached an $OD_{600nm}$ of 6-7.

#### b) Affinity Studies

#### i) Nanofibers

10 mg nanofiber mats were placed in polytops followed by pipetting in a 5 mL aliquot of BCG culture solution and sealing the polytops with parafilm. The polytops were incubated at 37 °C for 1 hour on a laboratory shaker. The nanofiber mats were removed and washed three times in PBS for 10 min followed by placing the mats in clean polytops.

#### ii) Nanoparticles

50 mg nanoparticles were placed in polytops followed by pipetting in a 5 mL aliquot of BCG culture solution and sealing the polytops with parafilm. The polytops were incubated at 37 °C for 1 hour on a laboratory shaker. The nanoparticles were separated with a magnet and washed three times in PBS for 10 min followed by placing the nanoparticles in clean polytops.

## 6.5 References

1. Yepes, J. F., Sullivan, J. & Pinto, A. Tuberculosis: Medical management update. *Oral Surgery, Oral Med. Oral Pathol. Oral Radiol. Endodontology* **98,** 267–273 (2004).
2. Crellin, P. K., Luo, C. & Morita, Y. S. Metabolism of Plasma Membrane Lipids in Mycobacteria and Corynebacteria. in *Lipid Metabolism* 119–148 (INTECH, 2013). doi:10.5772/52781
3. Kaur, D., Guerin, M. E., Škovierová, H., Brennan, P. J. & Jackson, M. Biogenesis of the cell wall and other glycoconjugates of *Mycobacterium tuberculosis*. *Adv. Appl. Microbiol.* **69,** 23–78 (2009).
4. Ostuni, E., Chapman, R. G., Liang, M. N., Meluleni, G., Pier, G., Ingber, D. E. & Whitesides, G. M. Self-Assembled Monolayers That Resist the Adsorption of Proteins and the Adhesion of

Bacterial and Mammalian Cells. *Langmuir* **17,** 6336–6343 (2001).

5. Esparza, M., Palomares, B., García, T., Espinosa, P., Zenteno, E. & Mancilla, R. PstS-1, the 38-kDa *Mycobacterium tuberculosis* glycoprotein, is an adhesin, which binds the macrophage mannose receptor and promotes phagocytosis. *Scand. J. Immunol.* **81,** 46–55 (2015).

6. Kim, C. H., Choi, J. W., Chun, H. J. & Choi, K. S. Synthesis of chitosan derivatives with quaternary ammonium salt and their antibacterial activity. *Polym. Bull.* **38,** 387–393 (1997).

7. Sahariah, P., Benediktssdóttir, B. E., Hjálmarsdóttir, M. Á., Sigurjonsson, O. E., Sørensen, K. K., Thygesen, M. B., Jensen, K. J. & Másson, M. Impact of chain length on antibacterial activity and hemocompatibility of quaternary *N*-alkyl and *N*, *N*-dialkyl chitosan derivatives. *Biomacromolecules* **16,** 1449–1460 (2015).

8. Birnie, C. R., Malamud, D. & Schnaare, R. L. Antimicrobial evaluation of *N*-Alkyl betaines and *N*-Alkyl-*N*,*N*-dimethylamine oxides with variations in chain length. *Antimicrob. Agents Chemother.* **44,** 2514–2517 (2000).

9. Lewis, K. N., Liao, R., Guinn, K. M., Hickey, M. J., Smith, S., Behr, M. A. & Sherman, D. R. Deletion of RD1 from *Mycobacterium tuberculosis* Mimics Bacille Calmette-Guérin Attenuation. **187,** 117–123 (2003).

10. Peñuelas-Urquides, K., Villarreal-Treviño, L., Silva-Ramírez, B., Rivadeneyra-Espinoza, L., Said-Fernández, S. & de León, M. B. Measuring of *Mycobacterium tuberculosis* growth. A correlation of the optical measurements with colony forming units. *Brazilian J. Microbiol.* **44,** 287–290 (2013).

11. Trivedi, A., Mavi, P. S., Bhatt, D. & Kumar, A. Thiol reductive stress induces cellulose-anchored biofilm formation in *Mycobacterium tuberculosis*. *Nat. Commun.* **7,** 11392 (2016).

12. Mothiba, M. T., Anderson, R., Fourie, B., Germishuizen, W. A. & Cholo, M. C. Effects of clofazimine on planktonic and biofilm growth of *Mycobacterium tuberculosis* and *Mycobacterium smegmatis*. *J. Glob. Antimicrob. Resist.* **3,** 13–18 (2015).

13. Tischer, M., Pradel, G., Ohlsen, K. & Holzgrabe, U. Quaternary ammonium salts and their antimicrobial potential: Targets or nonspecific interactions? *ChemMedChem* **7,** 22–31 (2012).

14. Ignatova, M., Manolova, N., Markova, N. & Rashkov, I. Electrospun non-woven nanofibrous hybrid mats based on chitosan and PLA for wound-dressing applications. *Macromol. Biosci.* **9,** 102–111 (2009).

15. Sai, H., Fu, R., Xiang, J., Guan, Y. & Zhang, F. Fabrication of elastic silica-bacterial cellulose composite aerogels with nanoscale interpenetrating network by ultrafast evaporative drying. *Compos. Sci. Technol.* **155,** 72–80 (2018).

# Chapter 7

## Conclusions and recommendations

## 7.1 Conclusions

The synthesis and characterization of modified chitosan and SMA polymers, which were electrospun into nanofibers and which were used to synthesize coated superparamagnetic magnetite nanoparticles, were presented in this thesis as *Mycobacterium tuberculosis* (*Mtb)* capturing platforms. The nano-substrates were evaluated for their affinity and thus capturing capabilities utilizing the mCherry fluorophore tagged bacillus Calmette-Guérin (BCG) strain of *Mycobacterium bovis*. BCG-mCherry was used as the live attenuated *Mtb*-mimic bacteria due to the pathogenic nature of *Mtb*.

### 7.1.1 Polymer modification

Chitosan was modified to yield quaternized derivatives with a permanent cationic charge by functionalizing with quaternary ammonium moieties. Poly(styrene-*alt*-maleic anhydride) (SMA) was synthesized via conventional free radical copolymerization and could be modified to form quaternary ammonium maleimide derivatives (SMI). Chitosan required functionalization with linker molecules in order to immobilize Concanavalin A (Con A) carbohydrate binding protein. These quaternary derivatives and Con A functionalized polymers were selected and synthesized due to possible chemical interaction and thus affinity for the BCG-mCherry cell wall.

Quaternary chitosan was synthesized by modifying chitosan with 3-dimethylamino-2,2-dimethylpropanal to yield the *N*-substituted chitosan precursor polymer. 3-dimethylamino-2,2-dimethylpropanal formed a Schiff base with the amino groups of chitosan, followed by adding a reducing agent ($NaBH_4$) to yield *N*-substituted chitosan. After which 1-bromodecane and 1-bromododecane were used to synthesize *N*,*N*-(2-dimethyl)propyl-3-*N',N'*-dimethyl-*N'*-decylammonium chitosan chloride (CS-q$C_{10}$) and *N*,*N*-(2-dimethyl)propyl -3-*N',N'*-dimethyl-*N'*-dodecylammonium chitosan chloride (CS-q$C_{12}$) respectively.

Pristine chitosan required modification via linker molecules for Con A immobilization. Chitosan was crosslinked with glutaraldehyde followed by activation with glycine and 1-ethyl-3-(3-dimethylaminopropyl) carbodiimide (EDC) thus forming CS-EDC.

SMA was modified with 3-(*N,N*-dimethylamino)-1-propylamine, where ring-opening of the maleic anhydride functional group enabled nucleophilic addition of the primary amine. Heating at 170 ˚C enabled ring closure and thus resulting in the formation of poly(styrene-[*N*-3-(*N',N'*-dimethylamino)propyl maleimide]) (SMI-tC). Addition of 1-bromodecane and 1-bromododecane resulted in poly(styrene-[*N*-3-(*N'*-decyl-*N',N'*-dimethylammonium)propyl maleimide]) (SMI-q$C_{10}$) and poly(styrene-[*N*-3-(*N'*-dodecyl-*N',N'*-dimethylammonium)propyl maleimide]) (SMI-q$C_{12}$) respectively. $^{1}$H NMR, $^{13}$C NMR, ATR-FTIR and $^{13}$C solid-state cross polarization magic-angle-spinning (CP-MAS) NMR for CS-EDC were used as characterization techniques to verify the formation of these compounds.

### 7.1.2 Nanofibers

CS-EDC, CS-q$C_{10}$ and CS-q$C_{12}$ were blended with poly(vinylalcohol) (PVA), polylactide (PLA) and polycaprolactam (Nylon 6) and electrospun via single needle electrospinning into polymer nanofibers with an average diameter of 264-437 nm, 202-349 nm and 111-204 nm, respectively. 1,2,3,4-butanetetracarboxylic acid was used as insitu crosslinking agent for the PVA blended fibers, while glutaraldehyde was used to crosslink the PLA fibers. PEO and PVP were electrospun and crosslinking agents namely glutaraldehyde, genipin and photocrosslinking agents were investigated. The PEO and PVP nanofibers were however soluble in phosphate buffered saline (PBS) solution and thus removed from the study. SMA, SMI-q$C_{10}$ and SMI-q$C_{12}$ were electrospun into nanofibers with average diameters of 380 nm, 494 nm and 482 nm respectively. Con A was immobilized to the SMA nanofibers and the CS-EDC/PVA, CS-EDC/PLA and CS-EDC/Nylon 6 nanofibers and the amount of biologically active Con A was determined to be 11.3 %, 15.1 %, 7.5 % and 11.3 % respectively. The modified chitosan derivatives required heat treatment at 100˚C while the SMA derivatives required heat treatment at 120˚C to crosslink and impart stability in PBS. Water contact angle measurements (WCA) were performed on the chitosan derivative films and SMA derivative nanofibers to determine the hydrophilicity/hydrophobicity in solution.

### 7.1.3 Nanoparticles

Pristine superparamagnetic magnetite nanoparticles (SPMNs) were produced via chemical co-precipitation of $Fe^{2+}$ and $Fe^{3+}$ ions (2:1) by addition of excess base (ammonium hydroxide) in aqueous solution under $N_2$ atmosphere. $N_2$ gas prevented oxidation and reduced the particle diameter. XRD determined that the nanoparticles were relatively pure in phase. The nanoparticles were magnetically characterized via SQUID magnetometry which indicated that the nanoparticles were superparamagnetic. The SPMNs had zero coercivity and zero remanence and a saturation magnetization of 29.0 emu/g.

SMI-qC$_{12}$ followed by CS-EDC-Con A was determined to be the polymer-and-functional-moiety combinations which captured the most BCG-mCherry bacteria. The SPMNs were thus polymer coated with SMI-qC$_{12}$ and CS-EDC-Con A which also prevented aggregation. The nanoparticles were coated with 0.1 g, 0.5 g and 0.9 g polymer per 1 g pristine SPMNs to determine the most effective polymer loading. CS-EDC-Con A SPMNs were synthesized via insitu co-precipitation of $Fe^{2+}$, $Fe^{3+}$ and chitosan followed by modification of the polymer coating. SMI-qC$_{12}$ SPMNs were synthesized by activating the iron oxide core with 3-aminopropyl(triethoxysilane) (3-APTES) followed by SMA coating and further modification of the polymer. The coated SPMNs were characterized via transmission electron microscopy (TEM), thermogravimetric analysis (TGA), attenuated total reflectance Fourier transform infrared (ATR-FTIR) spectroscopy and energy-dispersive X-ray (EDX) spectroscopy which confirmed that the nanoparticles were coated with polymer. TGA indicated that a higher coating % was achieved for 0.9 g polymer loading compared to 0.1 g polymer loading and a slight increase in average nanoparticle diameter was seen for the coated SPMNs via TEM. An HRP assay was performed on the CS-EDC-Con A SPMNs which confirmed the biological activity of Con A immobilized to the nanoparticles. SQUID magnetometry was performed on chitosan coated SPMNs and a decrease in saturation magnetization was observed, 22.6 emu/g compared to pristine SPMNs. The SPMNs however retained superparamagnetism after polymer coating.

### 7.1.4 BCG-mCherry affinity

A preliminary BCG-mCherry affinity study was performed on the nanofibers to determine which polymer-and-functional-moiety combination captured the most BCG-mCherry bacteria. Fluorescence microscopy (FM) and light microscopy (LM) were used to count the bacteria. The SMI-qC$_{12}$ nanofibers followed by the CS-EDC-Con A nanofibers had the highest affinity for BCG-mCherry. The SMI-qC$_{12}$ nanofibers could adhere to the BCG-mCherry cell wall via a combination of electrostatic and hydrophobic interactions whereas the Con A immobilized to the CS-EDC-Con A nanofibers could adhere to BCG-mCherry via the carbohydrate binding properties of the protein. The chitosan derivative nanofibers blended with PLA had the highest affinity for BCG-mCherry which was attributed to the hydrophobicity and biocompatibility of PLA. Hydrophobicity can improve adhesion to the hydrophobic outer layer of the bacteria.

A BCG-mCherry affinity and dilution study was performed on the SMI-qC$_{12}$ SPMNs and CS-EDC-Con A SPMNs at 0.1 g 0.5 g and 0.9 g polymer loadings. The nanofibers were more sensitive to BCG-mCherry bacteria compared to the SPMNs which could be attributed to chelation of the polymer coating to the iron oxide core and thus less available functional

groups. A larger amount of polymer could also be visualized via FM for the nanofibers compared to the SPMNs with a thin polymer coating. The SMI-q$C_{12}$ SPMNs had the highest BCG-mCherry affinity with a sensitivity of $OD_{600nm}$ = 0.07/0.22 ×$10^7$ CFU/mL. The 0.9 g SMI-q$C_{12}$ SPMNs captured the most BCG-mCherry bacteria as determined via TEM. The results can conclude that non-specific electrostatic and hydrophobic interactions (SMI-q$C_{12}$) lead to a higher BCG-mCherry affinity compared to specific carbohydrate-protein binding (CS-EDC-Con A).

The objectives of this thesis, to synthesize polymer coated SPMNs that can be used to capture and extract mycobacteria, was essentially met as outlined in Chapter 1. The optimal polymer-and-functional-moiety combination and polymer loading for BCG-mCherry affinity was also estimated. These polymer coated SPMNs can thus potentially be used to concentrate bacteria in a specimen, followed by extraction with an external magnet and analysis via FM, SEM and TEM.

## 7.2 Recommendations

The SPMNs with higher polymer loadings (0.9 g) had a higher affinity for BCG-mCherry. Polymer loadings higher than 0.9 g were, however, not investigated in this study. The synthesis of SPMNs with higher polymer loadings can thus be explored as well as the effect of higher polymer loading on particle diameter and superparamagnetism. In this thesis, the iron oxide core was activated with 3-APTES followed by SMA coating. Previous research also coated the iron oxide core with a silica layer followed by activation with 3-APTES.[1] An additional silica layer may affect the SMA coating and can thus be investigated. Con A could possibly be crosslinked to the polymer coated SPMNs to improve binding. The use of polymerase chain reaction (PCR) could be investigated as a molecular testing technique to verify if mycobacteria were captured on the SPMNs. Optimization of the parameters are, however, required to attain accurate PCR results. The nanofibers and polymer coated SPMNs were not evaluated for affinity to *Mtb*. A *Mtb* affinity study could thus be performed on the nanofibers and nanoparticles to determine if the results correlate with the BCG-mCherry affinity study.

## 7.3 References

1. Song, C., Sheng, L. & Zhang, X. Preparation and characterization of a thermostable enzyme (Mn-SOD) immobilized on supermagnetic nanoparticles. *Appl. Microbiol. Biotechnol.* **96,** 123–132 (2012).

# Addendum A

## Chitosan

Chitosan is the *N*-deacetylated derivative of chitin obtained by alkaline treatment, although the *N*-deacetylation is rarely complete. The structure of chitosan is composed of 2-amino-2-deoxy-β-d-glucopyranose (GlcN) and β(1→4)-linked 2-acetamido-2-deoxy-β-d-glucopyranose (GlcNAc) residues. The monomers thus differ with either an amino or an acetamide group as C2-substituent in the saccharide ring as seen in Figure A.1.[1]

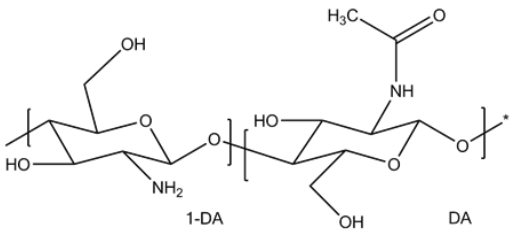


Figure A.1: Chemical structure of chitosan (1-DA (degree of acetylation)) (left) and chitin (DA=1) (right).

The degree of *N*-acetylation (DA) of chitosan can be measured as the average number of GlcNAc per 100 chitosan monomers in percentile units and thus the fraction of *N*-acetyl-d-glucosamine units. A DA distribution can be seen in the various chitosan chains due to its natural origin and variations in processing conditions. The conversion of chitin to chitosan can be verified by the ratio of GlcNAc to GlcN structural units. Chitosan is fully or partially *N*-deacetylated when the DA is less than 30% and where the degree of *N*-deacetylation (DDA) is thus ≥ 70%. The DA and DA distribution influences the solubility due to the distribution of free amino and *N*-acetyl groups. The deacetylated amino groups of GlcN can be protonated in an acidic solution which enables chitosan to dissolve under acidic conditions.[2]

### a) ATR-FTIR

The ATR-FTIR spectrum of pristine chitosan is shown in Figure A.2.

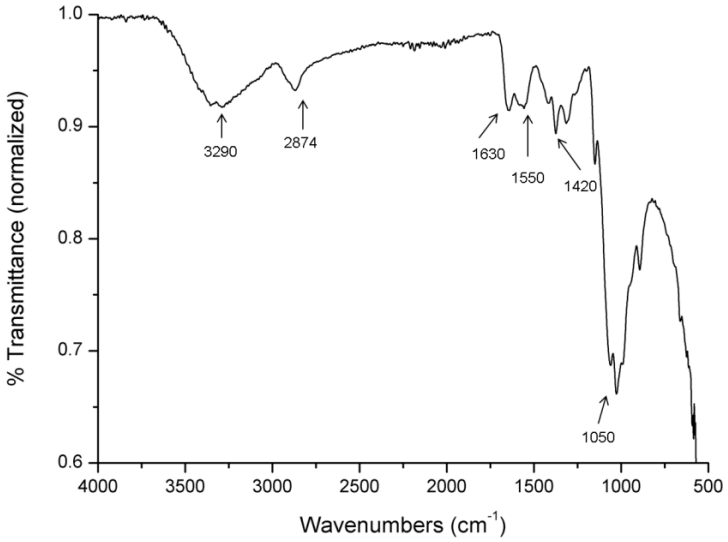


Figure A.2: FTIR spectrum of pristine chitosan.

Chitosan is of natural origin and extracted from the exoskeleton of crabs. A varying distribution of deacetylation and molecular weight can thus occur. The polymer was thus characterized followed by modification and characterization. The characteristic peaks can be assigned via literature as seen in Figure A.2. In the spectrum of chitosan a broad peak at 3050-3600 $cm^{-1}$ is attributed to the N-H and O-H stretching vibrations, the peak at 2874 $cm^{-1}$ can be assigned to the C-H stretching vibration of the methylene groups, the peaks at 1630 $cm^{-1}$ and 1550 cm−1 are assigned to the carbonyl stretching and the N-H deformation (amide I, amide II band), respectively, the peak at 1420 $cm^{-1}$ represents the C-N vibration, while the peak at 1050 $cm^{-1}$ is attributed to the C-O-C stretching vibration.[3,4]

**b) NMR**

The medium molecular weight ($M_w$ = 129 kD) unmodified chitosan polymer was purchased with a reported degree of *N*-deacetylation (DDA) of 75 – 85% and used as parent polymer.

The $^1$H NMR spectrum of pristine chitosan (Figure A.3) can be characterized by the peak at 5.28 ppm due the methine protons of chitosan carbon 1 (C-1). The peak at 4.28 ppm is due to the methine protons (C-3 and C-4) and the methylene C-6 protons of the glycopyranose unit. The overlapping absorption peak at 4.11 ppm can be attributed to the methine protons C-5 of the glycopyranose unit and those of methylene C-6' protons of the glucopyranose (chitin) unit. The methine proton, C-2 of the glycopyranose ring can be assigned to the peak at 3.58 ppm. The peak at 2.41 ppm can be assigned to the methyl protons of the acetamido groups (chitin residue) and the overlapping weak acetic acid (AcOH) peak.[3]

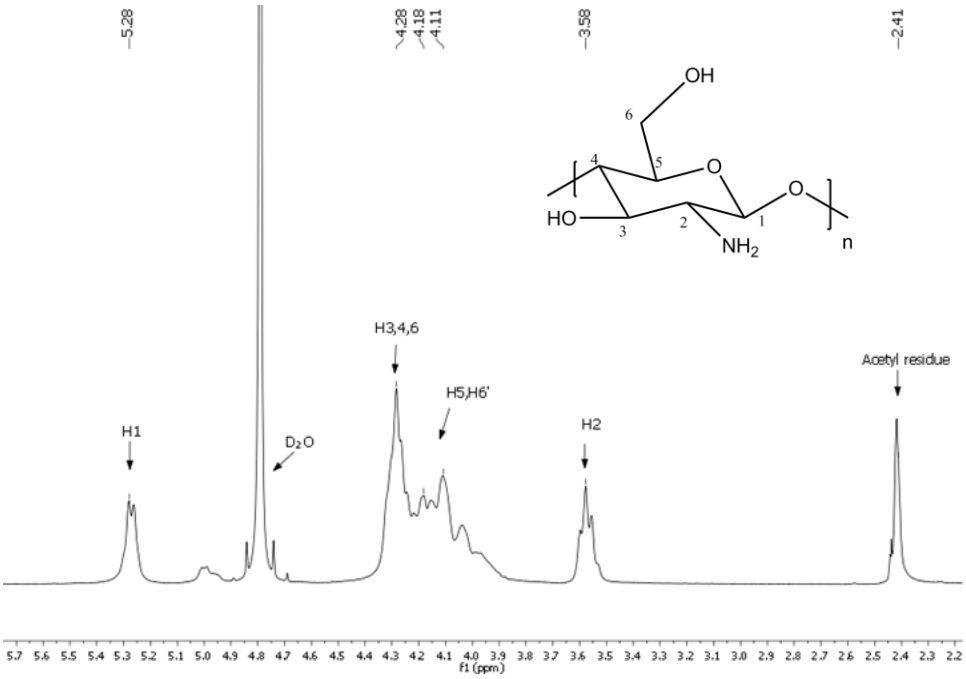


Figure A.3: $^{1}$H-NMR spectrum of chitosan at 80 ˚C in $D_20$/Acetic acid-d4 (70:30, v/v).

The DDA was determined using the integrals of the peaks H-1 corresponding to the deacetylated monomer and the three protons of the acetyl group (2.41 ppm). The Equation A.1 was used.[5]

$$\mathrm{DDA\%} = \frac{\mathrm{H_1D}}{\mathrm{H_1D} + \frac{\mathrm{H_{Ac}}}{3}} \times 100 \qquad \mathrm{A.1}$$

The DDA of chitosan was determined to be 75%, in percentile units per 100 chitosan monomer units.

From the $^{13}$C NMR spectrum of chitosan Figure A.4 the peaks at 177.2 and 25.1 ppm, adjacent to the solvent signals, can be attributed to the carbonyl and methyl groups of the monomeric chitin due to incomplete deacetylation. The chitin residue signal can be enhanced by the temperature of NMR analysis (80 ˚C) where partial conversion to chitin can occur.[6] The chemical shift of 100.8 ppm can be assigned to C-1, 80.4 ppm to C-4, 77.7ppm to C-5, 73.1 ppm to C-3, 63.3 ppm to C-6 and 59.0 ppm to C-2. [7]

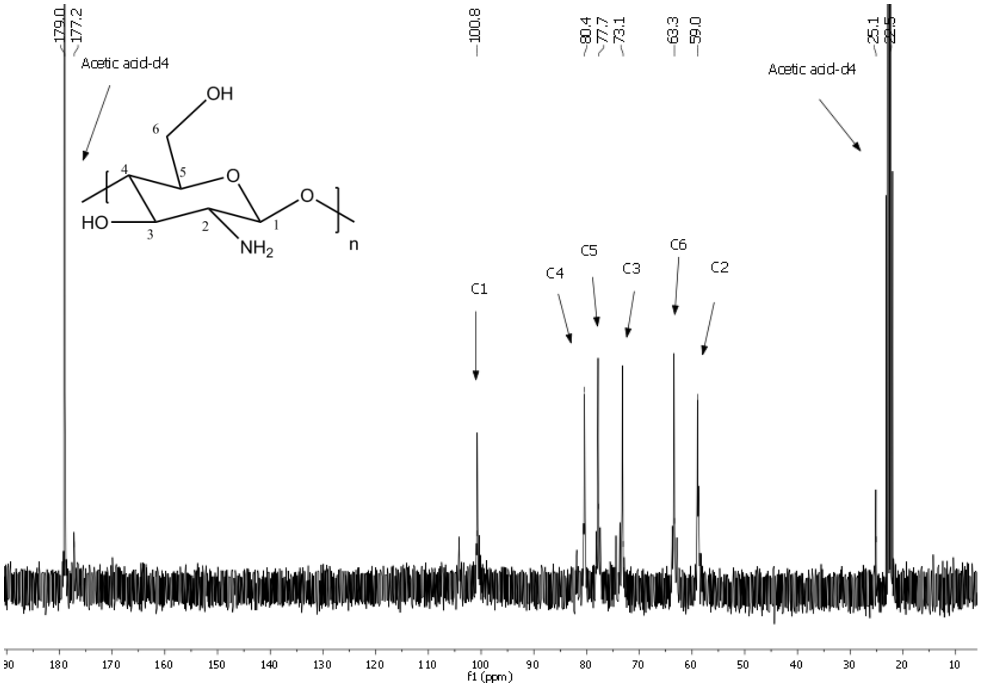


Figure A.4: $^{13}$C-NMR spectrum of chitosan at 80 ˚C in $D_20$/Acetic acid-d4 (70:30, v/v).

# Addendum B

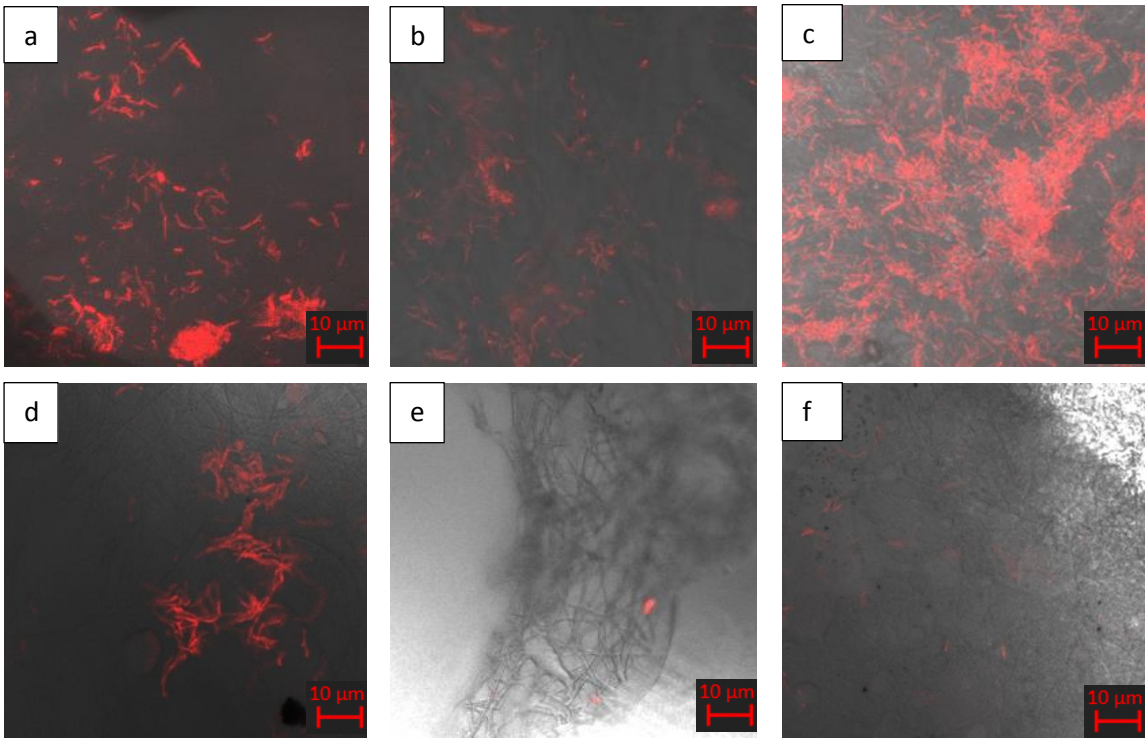

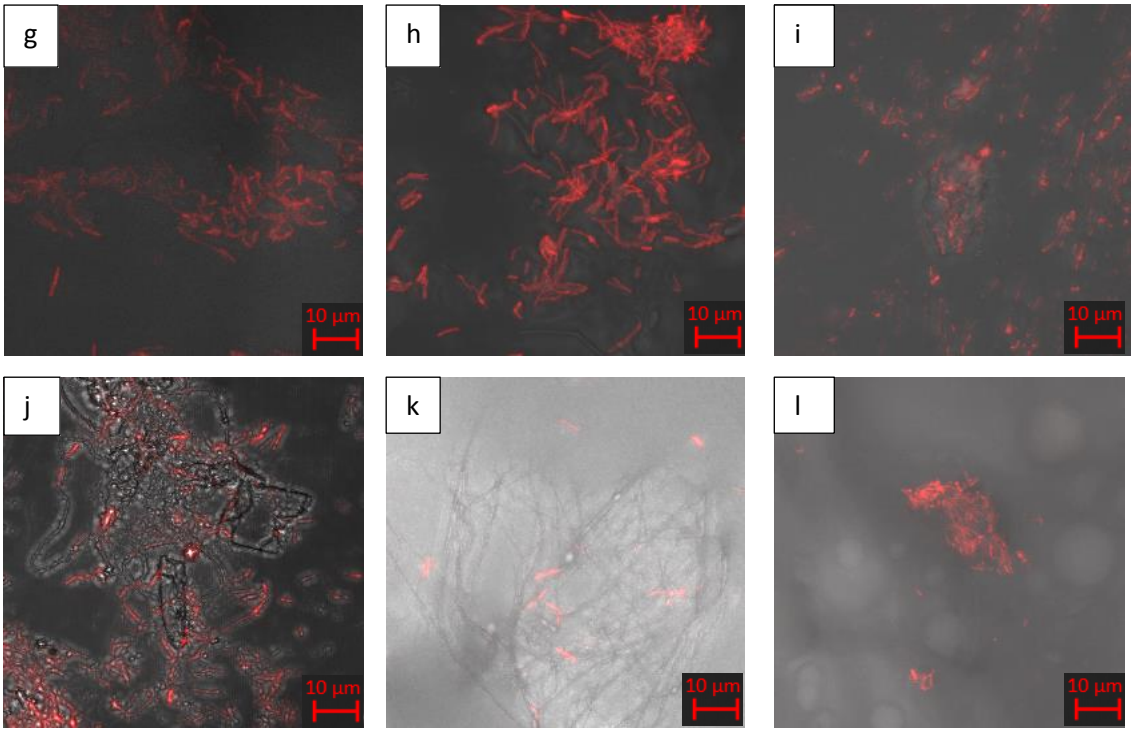


Figure B: Fluorescence microscopy (FM) and Light microscopy (LM) images of nanofibers incubated in $OD_{600nm}$=6 a) SMI-Con A, b) SMI-$qC_{10}$, c) SMI-$qC_{12}$, d) CS-EDC-Con A/PVA, e)CS-$qC_{10}$/PVA, f) CS-$qC_{12}$/PVA, g) CS-EDC-Con A/PLA, h) Cs-$qC_{10}$/PLA, i) CS-$qC_{12}$/PLA, j) CS-EDC-Con A/Nylon 6, k) CS-$qC_{10}$/Nylon 6, l) CS-$qC_{12}$/Nylon 6.

# Addendum C

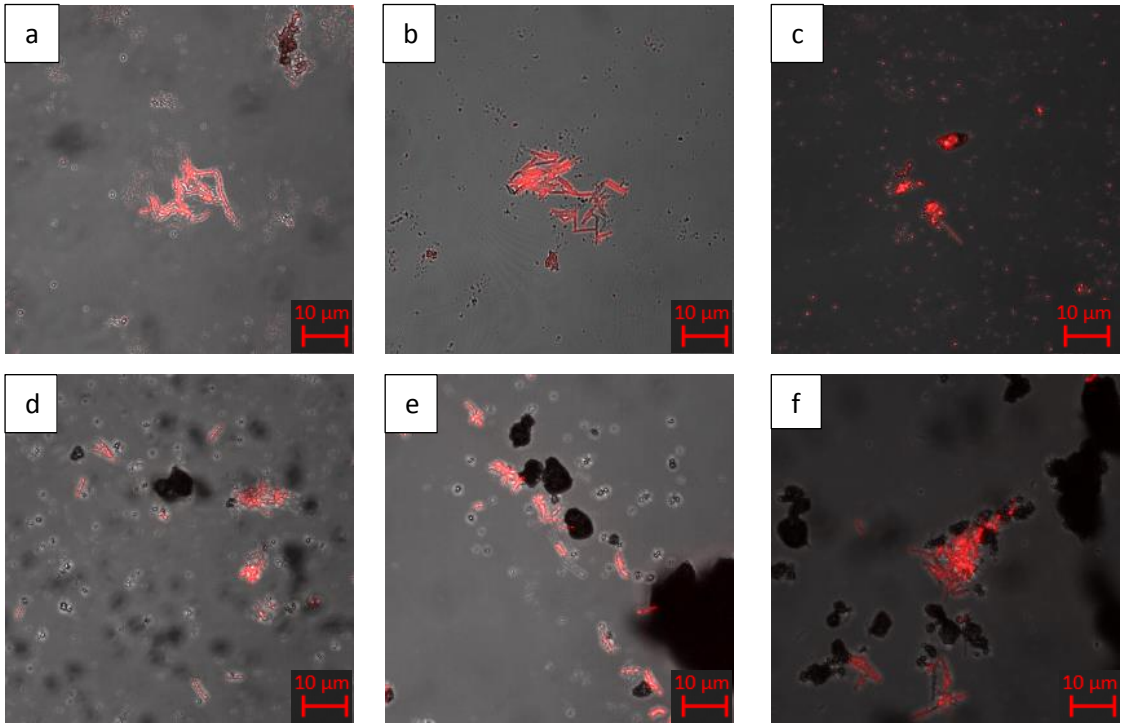

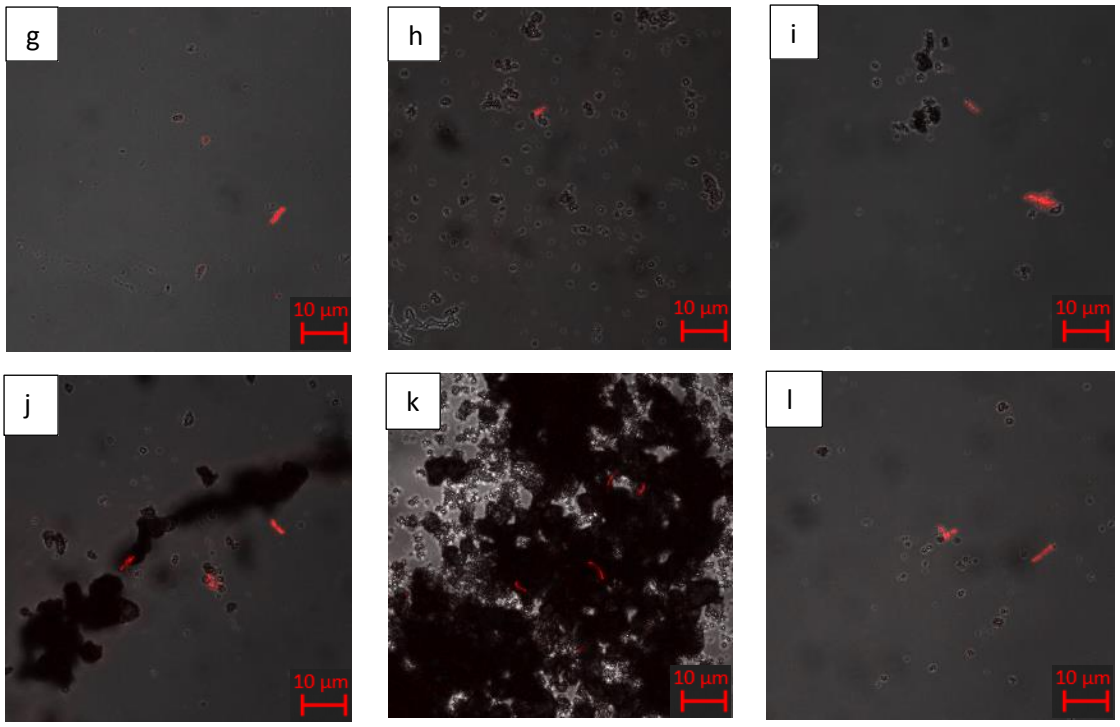


Figure C.1: Fluorescence microscopy overlaid with Light microscopy images at $OD_{600nm}$ = 7 for a) 0.1 g CS-EDC-Con A SPMNs, b) 0.5 g CS-EDC-Con A SPMNs, c) 0.9 g CS-EDC-Con A SPMNs, d) 0.1 g SMI-$qC_{12}$ SPMNs, e) 0.5 g SMI-$qC_{12}$ SPMNs, f) 0.9 g SMI-$qC_{12}$ SPMNs, at $OD_{600nm}$ = 0.7 for g) 0.1 g CS-EDC-Con A SPMNs, h) 0.1 g SMI-$qC_{12}$ SPMNs, i) 0.5 g SMI-$qC_{12}$ SPMNs, j) 0.9 g SMI-$qC_{12}$ SPMNs, at $OD_{600nm}$ = 0.07 for k) 0.1 g SMI-$qC_{12}$ SPMNs and l) 0.5 g SMI-$qC_{12}$ SPMNs.

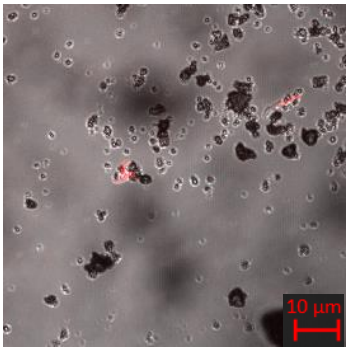


Figure C.2: Fluorescence microscopy overlaid with Light microscopy image at $OD_{600nm}$ = 0.07 for 0.9 g SMI-$qC_{12}$ SPMNs.

## References

1. Kumar, M. A review of chitin and chitosan applications. *React. Funct. Polym.* **46,** 1–27 (2000).

2. Jerushan, J., Paul, M., Leeuwen, V., Cottet, H., Castignolles, P. & Gaborieau, M. International Journal of Biological Macromolecules Determination of the distributions of degrees of acetylation of chitosan. *Int. J. Biol. Macromol.* **95,** 40–48 (2017).

3. Liu, J., Pu, H., Liu, S., Kan, J. & Jin, C. Synthesis , characterization , bioactivity and potential application of phenolic acid grafted chitosan : A review. *Carbohydr. Polym.* **174,** 999–1017

(2017).

4. Branca, C., D'Angelo, G., Crupi, C., Khouzami, K., Ri, S., Ruello, G. & Wanderlingh, U. Role of the OH and NH vibrational groups in polysaccharide- nanocomposite interactions : A FTIR-ATR study on chitosan and chitosan / clay films. **99,** 614–622 (2016).

5. Abdel-Rahman, R. M., Hrdina, R., Abdel-Mohsen, A. M., Fouda, M. M. G., Soliman, A. Y., Mohamed, F. K., Mohsin, K. & Pinto, T. D. Chitin and chitosan from Brazilian Atlantic Coast: Isolation, characterization and antibacterial activity. *Int. J. Biol. Macromol.* **80,** 107–120 (2015).

6. Quijada-Garrido, I., Iglesias-González, V., Mazón-Arechederra, J. M. & Barrales-Rienda, J. M. The role played by the interactions of small molecules with chitosan and their transition temperatures. Glass-forming liquids: 1,2,3-Propantriol (glycerol). *Carbohydr. Polym.* **68,** 173–186 (2007).

7. Toeri, J., Osorio-Madrazo, A. & Laborie, M.-P. Preparation and Chemical/Microstructural Characterization of Azacrown Ether-Crosslinked Chitosan Films. *Materials (Basel).* **10,** 400 (2017).